VTRC
Virginia Transportation Research Council

We Bring Innovation to Transportation

Methods for Evaluation of the Remaining Shear Capacity in Steel Bridge Beams With Section Losses Attributable to Corrosion Damage

http://www.virginiadot.org/vtrc/main/online_reports/pdf/22-r4.pdf

EULOGIO M. JAVIER III
Graduate Research Assistant
Charles E. Via, Jr. Department of Civil & Environmental Engineering
Virginia Tech

MATTHEW H. HEBDON, Ph.D., P.E.
Associate Professor
Department of Civil, Architectural and Environmental Engineering
The University of Texas at Austin

JASON T. PROVINES, P.E.
Research Scientist
Virginia Transportation Research Council

Final Report VTRC 22-R4

VIRGINIA TRANSPORTATION RESEARCH COUNCIL
530 Edgemont Road, Charlottesville, VA 22903-2454
vtrc.virginiadot.org

Standard Title Page - Report on Federally Funded Project

1. Report No.: FHWA/VTRC 22-R4	2. Government Accession No.:	3. Recipient's Catalog No.:
4. Title and Subtitle: Methods for Evaluation of the Remaining Shear Capacity in Steel Bridge Beams With Section Losses Attributable to Corrosion Damage		5. Report Date: October 2021 6. Performing Organization Code:
7. Author(s): Eulogio M. Javier III, Matthew H. Hebdon, Ph.D., P.E., and Jason T. Provines, P.E.		8. Performing Organization Report No.: VTRC 22-R4
9. Performing Organization and Address: Virginia Transportation Research Council 530 Edgemont Road Charlottesville, VA 22903		10. Work Unit No. (TRAIS): 11. Contract or Grant No.: 114324
12. Sponsoring Agencies' Name and Address: Virginia Department of Transportation 1401 E. Broad Street Richmond, VA 23219 Federal Highway Administration 400 North 8th Street, Room 750 Richmond, VA 23219-4825		13. Type of Report and Period Covered: Final Contract 14. Sponsoring Agency Code:
15. Supplementary Notes: This is an SPR-B report.		

16. Abstract:

Steel bridges commonly have corrosion at beam ends because of leaking joints, which provide a pathway for de-icing salts to fall onto the beams from the roadway above. Once beam ends have corrosion damage, it becomes more difficult to determine their remaining shear capacity to be used for load rating. This is because classical design equations are based on intact sections and do not account for corrosion damage. This study was conducted to understand better the structural behavior of unstiffened steel bridge beams that have section loss near the bearings and to determine a simple, effective method for determining the remaining shear capacity of corroded beams during load rating.

Seventeen beams from four decommissioned structures throughout Virginia were experimentally tested in a laboratory to induce web shear failure near the bearing locations and were measured for load, vertical displacement, and web strain behavior. Strain was measured using a digital image correlation system to create a digital strain field at discrete load and beam displacement intervals during testing. The large-scale test results were compared to shear capacity calculations conducted in accordance with the *AASHTO LRFD Bridge Design Specifications;* AISC (American Institute of Steel Construction) 360-16; the Massachusetts Department of Transportation *LRFD Bridge Manual;* and other methods found in the literature for calculating the shear capacity of the damaged steel beam ends. The study found that using the shear capacity calculations presented by Tzortzinis et al. (2019a) in *Development of Load Rating Procedures for Deteriorated Steel Beam Ends* resulted in reliable shear capacity predictions.

The study also concluded that AASHTOWare Bridge Rating (BrR) can be used for determining the capacity of steel beams with corrosion using the percent web thickness loss input in the program. When doing so for a corroded steel beam without holes, the accuracy of BrR can be improved by calculating the percent thickness loss input in the BrR deterioration profile using a portion of the web with a height equal to the bottom or top 3 in of the web, depending on the location of severe corrosion, and a length equal to the lesser of the bearing length plus the beam height or the extent of the corrosion damage near the bearing. When doing so for a corroded steel beam end with holes, the accuracy of BrR can be improved by using the same portion of the web and by modifying the remaining average web thickness using the guidelines provided in the Massachusetts Department of Transportation *LRFD Bridge Manual* before inputting the percent thickness loss into the BrR deterioration profile.

Based on these conclusions, the study recommends that the Virginia Department of Transportation provide guidance (1) in a job aid to bridge inspectors for enhanced web thickness measurements and measurements of holes to be used when inspecting unstiffened corroded steel beam ends in Condition State 4 on bridges without diaphragms or a concrete deck, and (2) in its upcoming new load rating user manual to define the portion of the web and web thickness modification to account for holes when the same corroded steel beam ends are load rated.

17 Key Words: Corrosion, steel beam end, shear capacity, load rating, AASHTOWare BrR, inspection	18. Distribution Statement: No restrictions. This document is available to the public through NTIS, Springfield, VA 22161.		
19. Security Classif. (of this report): Unclassified	20. Security Classif. (of this page): Unclassified	21. No. of Pages: 77	22. Price:

FINAL REPORT

METHODS FOR EVALUATION OF THE REMAINING SHEAR CAPACITY IN STEEL BRIDGE BEAMS WITH SECTION LOSSES ATTRIBUTABLE TO CORROSION DAMAGE

Eulogio M. Javier III
Graduate Research Assistant
Charles E. Via, Jr. Department of Civil & Environmental Engineering
Virginia Tech

Matthew H. Hebdon, Ph.D., P.E.
Associate Professor
Department of Civil, Architectural and Environmental Engineering
The University of Texas at Austin

Jason T. Provines, P.E.
Senior Research Scientist
Virginia Transportation Research Council

In cooperation with the U.S. Department of Transportation
Federal Highway Administration

Virginia Transportation Research Council
(A partnership of the Virginia Department of Transportation
and the University of Virginia since 1948)

Charlottesville, Virginia

October 2021
VTRC 22-R4

DISCLAIMER

The contents of this report reflect the views of the authors, who are responsible for the facts and the accuracy of the data presented herein. The contents do not necessarily reflect the official views or policies of the Virginia Department of Transportation, the Commonwealth Transportation Board, or the Federal Highway Administration. This report does not constitute a standard, specification, or regulation. Any inclusion of manufacturer names, trade names, or trademarks is for identification purposes only and is not to be considered an endorsement.

ABSTRACT

Steel bridges commonly have corrosion at beam ends because of leaking joints, which provide a pathway for de-icing salts to fall onto the beams from the roadway above. Once beam ends have corrosion damage, it becomes more difficult to determine their remaining shear capacity to be used for load rating. This is because classical design equations are based on intact sections and do not account for corrosion damage. This study was conducted to understand better the structural behavior of unstiffened steel bridge beams that have section loss near the bearings and to determine a simple, effective method for determining the remaining shear capacity of corroded beams during load rating.

Seventeen beams from four decommissioned structures throughout Virginia were experimentally tested in a laboratory to induce web shear failure near the bearing locations and were measured for load, vertical displacement, and web strain behavior. Strain was measured using a digital image correlation system to create a digital strain field at discrete load and beam displacement intervals during testing. The large-scale test results were compared to shear capacity calculations conducted in accordance with the *AASHTO LRFD Bridge Design Specifications;* AISC (American Institute of Steel Construction) 360-16; the Massachusetts Department of Transportation *LRFD Bridge Manual;* and other methods found in the literature for calculating the shear capacity of the damaged steel beam ends. The study found that using the shear capacity calculations presented by Tzortzinis et al. (2019a) in *Development of Load Rating Procedures for Deteriorated Steel Beam Ends* resulted in reliable shear capacity predictions.

The study also concluded that AASHTOWare Bridge Rating (BrR) can be used for determining the capacity of steel beams with corrosion using the percent web thickness loss input in the program. When doing so for a corroded steel beam without holes, the accuracy of BrR can be improved by calculating the percent thickness loss input in the BrR deterioration profile using a portion of the web with a height equal to the bottom or top 3 in of the web, depending on the location of severe corrosion, and a length equal to the lesser of the bearing length plus the beam height or the extent of the corrosion damage near the bearing. When doing so for a corroded steel beam end with holes, the accuracy of BrR can be improved by using the same portion of the web and by modifying the remaining average web thickness using the guidelines provided in the Massachusetts Department of Transportation *LRFD Bridge Manual* before inputting the percent thickness loss into the BrR deterioration profile.

Based on these conclusions, the study recommends that the Virginia Department of Transportation provide guidance (1) in a job aid to bridge inspectors for enhanced web thickness measurements and measurements of holes to be used when inspecting unstiffened corroded steel beam ends in Condition State 4 on bridges without diaphragms or a concrete deck, and (2) in its upcoming new load rating user manual to define the portion of the web and web thickness modification to account for holes when the same corroded steel beam ends are load rated.

FINAL REPORT

METHODS FOR EVALUATION OF THE REMAINING SHEAR CAPACITY IN STEEL BRIDGE BEAMS WITH SECTION LOSSES ATTRIBUTABLE TO CORROSION DAMAGE

Eulogio M. Javier III
Graduate Research Assistant
Charles E. Via, Jr. Department of Civil & Environmental Engineering
Virginia Tech

Matthew H. Hebdon, Ph.D., P.E.
Associate Professor
Department of Civil, Architectural and Environmental Engineering
The University of Texas at Austin

Jason T. Provines, P.E.
Senior Research Scientist
Virginia Transportation Research Council

INTRODUCTION

Because of the aging infrastructure in the United States, significant effort is required to maintain and repair existing structures. Although many factors contribute to the degradation of bridge conditions, losses in steel bridge capacity over time can often be attributed to the corrosion of steel beams. Although corrosion is a natural occurrence, the process may be accelerated because of applied chemicals, most notably chlorides, that have a pronounced effect on metals' speed of corrosivity. In the United States, the most common chloride sources for bridges are seawater and de-icing salts. The exposure of steel superstructure beams to de-icing salts often occurs because of the leaking of expansion joints above bearing locations. Roadway runoff from these damaged joints can cause accelerated corrosion of the beam ends, which can result in significant web thickness losses over time (see Figure 1). These losses can reduce the available web area to resist the high shear loads typically present at the supports. As a result, many bridges have to be posted for reduced capacity or closed to traffic because of operating safety concerns.

The Virginia Department of Transportation (VDOT) employs the American Association of State Highway and Transportation Officials (AASHTO) load and resistance factor design/rating (LRFD/LRFR) shear capacity calculations as defined in the AASHTO *Manual for Bridge Evaluation* (AASHTO, 2018) to assess bridges with this type of steel beam corrosion for load rating. These calculations were derived initially from Timoshenko plate buckling theory, where the beam web is assumed to be a simply supported, prismatic plate member (Timoshenko and Gere, 1961). Although this assumption may be correctly used for a newly constructed bridge beam, the deteriorated beam sections inherent in corroded steel bridge beams do not closely resemble this idealized geometry.

Figure 1. Example of Extensive Beam End Corrosion Damage

This issue is further illustrated when the shear capacity formulas are considered; they rely on a uniform web thickness. Corroded steel beam webs often display highly localized and irregular section profiles, with varying thicknesses along their length and height. This variation in web thickness creates some confusion in determining what thickness is appropriate to use in residual capacity analyses.

VDOT regularly uses AASHTOWare Bridge Rating, hereinafter "BrR," to perform load rating of bridges. BrR uses an assumed uniform web thickness to provide an approximate value for these shear calculations. However, assuming a uniform web thickness is questionable because of ambiguity regarding the proper measurement of beam corrosion and consistency in applying these measurements to shear calculations. The shear calculations are based on the thickness of an assumed prismatic plate member. Thus, the safest approach to using this method is to apply a reduced web thickness to receive a conservative estimate of the capacity. For example, this method is achieved by multiplying the web thickness by a reduction factor or using the minimum measured local web thickness as the assumed constant web thickness. Even with these simplifications considered, bridges can also have highly localized damage such as pitting or even holes in the web, which may further complicate the implementation and accuracy of this method.

Figure 2 shows the four condition states for the beam end element in the *VDOT Supplement to the AASHTO Manual for Bridge Element Inspection* (VDOT, 2016). As shown in the figure, beam ends in Condition State 4 have sufficient corrosion damage to warrant additional structural analysis during load rating. Information regarding the actual quantity of section loss is dependent on the description given in the VDOT inspection report, which is at the discretion of the inspector. Typically, an approximated uniform section loss on the web and flanges is given, but diagrams, dimensions, and pictures provided in the report may vary among VDOT districts and even among inspectors within districts. For example, the consensus of bridge inspectors in VDOT's Staunton District is that a rating of 1 indicates zero section loss; 2 indicates less than 1/16-in section loss; 3 indicates approximately 1/16-in section loss, and 4 indicates greater than 1/16-in section loss.

VDOT ELEMENT NUMBER	811	VDOT ELEMENT NAME	BEAM/GIRDER END
DESCRIPTION	This element defines the last 5 feet of a beam/girder end. Measurement shall begin at the end of the beam/girder and continue toward the center of the structure.		
UNIT OF MEASURE	EA		

STEEL		CONDITION STATES			
DEFECT		1	2	3	4
		GOOD	FAIR	POOR	SEVERE
1000	Corrosion	None	Freckled Rust. Corrosion of the steel has initiated.	Section loss is evident, or pack rust is present but does not warrant structural review.	The condition warrants a structural review to determine the effect on strength or serviceability of the element or bridge; OR a structural review has been completed and the defects impact strength or serviceability of the element or bridge.

Figure 2. VDOT Steel Beam End Element Condition States. Virginia Department of Transportation (2016).

The failure modes associated with shear loads on steel beams, with or without corrosion damage, include web buckling, web yielding, web crippling, and web compression cracking. Web buckling occurs in beams with slender webs, where high stresses within the height of the member cause sudden lateral deformation of the beam perpendicular to the line between the applied load and the support. Although the loads required to initiate this type of failure are typically much higher than for other types, web buckling may occur because of web thinning in the beam's height between the applied load and the support. Web yielding and web crippling occur because of the high concentrations of forces located directly beneath the applied load and directly above the support. Although the failure types may appear similar, AISC 360-16 defines web local crippling as "crumpling of the web into buckled waves directly beneath the load, occurring in more slender webs, whereas local web yielding is yielding of that same area, occurring in stockier webs" (American Institute of Steel Construction [AISC], 2016). There were no examples of web yielding during this study.

Typical images of the three shear failure types related to this study are shown in Figure 3. Figure 3a shows a web buckling failure occurring within the diagonal red oval perpendicular to the dashed red line between the applied load and the support. This example occurred because of web section losses thinning the web at mid-height between the applied load and the support. Figure 3b shows an example of a web crippling failure that occurred at 3 in above the bottom flange at the bearing for a slender W-shape beam. Some failures more closely resemble continuous plastic web deformation along the length of the web and starting at the beam end, as opposed to true web crippling failures, which would develop above the bearing because of high concentrations of compressive force. Although it is worth noting that these failures did not meet the traditional definition of web crippling, they are referred to as web crippling failures because

of their similarity in location and for the simplicity of categorization. Figure 3c shows an example of web cracking, where cracks formed between adjacent web holes along the height of the beam. This crack formed because of the formation of diagonal shear stress bands perpendicular to the loads creating tension forces, shown as red arrows, which pulled the web apart in the red oval.

Figure 3. Photographs of Shear Failure Types: (a) web buckling; (b) web crippling; (c) web cracking.

PURPOSE AND SCOPE

The purpose of this study was to determine an appropriate method of assessing the remaining capacity of beams that exhibit web section losses because of corrosion. Several available capacity calculation methods were compared with the results of 17 steel beam tests to determine their accuracy and applicability for VDOT uses. Results from this analysis should increase the reliability of capacity assessment for corrosion-damaged steel bridges, which will yield safer load ratings with higher confidence.

This scope of the study included laboratory testing and determination of a method to predict corroded beam end shear capacity. Full-scale flexural testing of 17 steel beams was conducted at the Thomas M. Murray Structures Laboratory (hereinafter "structures laboratory") at Virginia Tech. These steel beams were acquired from bridges located in several VDOT districts throughout Virginia and selected to encompass a full range of damage. This range included beams from near zero section loss to severe localized end damage, including full height web thickness reduction and through-thickness holes. Several existing capacity calculation methods were then compared to determine their correlation to the full-scale testing results. Finally, an investigation was made to determine how these test results could be applied to determine shear capacity using BrR.

It is currently up to the load rating engineer to negotiate these uncertain variables using his or her engineering judgment to determine an appropriate capacity. This study intended to reduce the uncertainty inherent in this approach by comparing full-scale load testing results to existing shear capacity calculations to determine an accurate method of calculating shear capacity on steel bridges with corrosion-related section losses.

METHODS

Four tasks were conducted to achieve the study objectives:

1. Conduct a literature review.

2. Conduct large-scale flexural tests on out-of-service steel bridge beams to determine the remaining capacity and shear behavior under near–end point loading.

3. Determine a simplified capacity calculation method by comparing existing load rating methods to the large-scale test results to allow VDOT to approximate the remaining shear capacity of corroded steel bridges without needing rigorous analyses.

4. Compare results from the large-scale tests to capacity results using BrR to determine if the latter were accurate or needed modification for increased accuracy.

Task 1: Literature Review

A literature review was conducted to synthesize information from previous studies and guidelines regarding the effects of section loss on the behavior of steel beams. This review included the impact of governing factors such as corrosion patterns, the fidelity of corrosion measurement, and the geometries and location of section losses and holes. Most important, the review summarized several methods that could predict the shear capacity of steel beams with corroded ends.

Task 2: Large-Scale Flexural Tests

Specimen Acquisition and Selection

All bridge beams used in this study were received through contact with several VDOT districts and residencies, whose ongoing maintenance work includes the replacement and disposal of retired bridge superstructures. For many of these beams, their availability was limited because of logistics concerning construction schedules and access to vehicles for hauling beams. Because of this limitation, deteriorated bridge beam candidates were briefly reviewed to determine if they were appropriate for the experimental testing. This assessment included in-person inspection when available, discussion with VDOT engineers, and a review of available bridge inspection documents with VDOT's permission. After a bridge was determined to show adequate corrosion damage for the study, beams were transported to the structures laboratory at Virginia Tech. To maximize the pool of available beams from which to select, nine total sets of bridge beams were delivered to the laboratory. Of these nine sets, 17 beam ends from four bridges were selected for testing.

Beams with bearing stiffeners were excluded because of their effect on beam capacity to simplify determining a simplified analysis method. In addition, many of VDOT's steel beam bridges with timber decks have corrosion damage and do not have bearing stiffeners. The initial

selection and damage ranking of these specimen conditions were made visually according to apparent section loss but were further quantified using more precise measurements after the beams were cleaned. Each beam set included four beams of identical beam shape except for the W16x45 beams. Five of these beams were tested because the original four selected beams did not fully encompass the previously mentioned range of damage types.

Specimen Matrix

The four test beam groups totaled 17 specimens, listed in Table 1 along with their nominal web thickness and minimum average web thickness. Individual beams were selected to represent a qualitative spectrum of section loss and web damage defined as low, medium low, medium high, and high. However, because of specimen availability, not every beam set included an ideal range of corrosion damage. In cases such as this, a beam with a greater or lesser amount of damage was selected to fill the gap. For example, the medium-high-damage and high-damage S8x18.4 beams showed more than 50% section loss whereas the high-damage beam for the W10x26 specimens showed slightly more than 25% section loss.

Table 1. Specimen Matrix for Steel Beam End Corrosion Flexural Tests

Specimen No.	Beam Shape	Specimen Name	Web Damage Condition	Beam Depth (in)	Nominal Web Thickness (in)	Minimum Average Web Thickness (in)	% Thickness Remaining
1	S8x18.4	1-S8-L	Low	8.0	0.271	0.271	99.8%
2		2-S8-ML	Medium-Low			0.225	83.1%
3		3-S8-MH	Medium-High			0.126	46.4%
4		4-S8-H	High			0.125	46.0%
5	W10x26	5-W10-L	Low	10.3	0.260	0.256	98.3%
6		6-W10-ML	Medium-Low			0.247	95.0%
7		7-W10-MH	Medium-High			0.191	73.6%
8		8-W10-H	High			0.193	74.3%
9	W16x45	9-W16-L	Low	16.1	0.345	0.261	75.7%
10		10-W16-ML	Medium-Low			0.324	93.9%
11		11-W16-MH	Medium-High			0.308	89.3%
12		12-W16-H	High			0.330	95.6%
13		13-W16-L(A)	Low Alternate			0.337	97.6%
14	W21x62	14-W21-L	Low	21.0	0.400	0.387	96.7%
15		15-W21-ML	Medium-Low			0.364	91.0%
16		16-W21-MH	Medium-High			0.344	86.1%
17		17-W21-H	High			0.294	73.5%

Discrepancies with the beam damage ranking are further discussed throughout the report, but the order of the web damage conditions was not changed from their original physical assessment. In addition, the use of the minimum average web thickness also resulted in some discrepancies, such as Specimen 9-W16-L appearing to have much more section loss than the beams with more damaged beam rankings. This was due to the presence of severe localized beam end damage that skewed the average web thickness far below what would be representative of the rest of the beam.

The minimum average web thicknesses shown in the table, which were used to calculate the remaining capacity, were determined by averaging the web thickness measurements over the beam height at the cross section with the most section loss, as described previously. In addition, each beam was given a designation, which is how the beams are referred to throughout the remainder of this report. The specimen naming convention represents information about the specimen separated by dashes. The first number describes the test order as the tests were performed from 1 to 17, followed by the structural shape and height, and concludes with abbreviations of the specimen's condition state. For example, "1-S8-L" indicates that the test was the first test completed, the beam has an S8 shape, and the web represents a specimen with low corrosion losses.

Specimen Preparation

Each beam was prepared before testing to remove existing corrosion and paint on the surfaces that were to be analyzed during testing. Oxidized steel layers adhering to the beam surface were initially removed using a chisel or a Mason hammer. Initial paint removal was then performed using an alkaline paint removal system that chemically stripped layers of paint from the beam surfaces. One of the significant issues with this method was the necessity to avoid lead particulate poisoning and spread because of the unknown makeup of the existing paint on the beams. This process required much certification and monitoring to achieve, which significantly delayed progress on specimen preparation. The process also required the full breadth of personal protective equipment, including a respirator, chemical goggles, nitrile gloves, and a full Tyvek suit to prevent injury or harm to the operator. In addition, the use of an abrasive blasting system was attempted for paint removal. The required amount of air pressure exceeded that provided by the laboratory's portable air compressor, which could not be used outside the laboratory where the beams were stored. Finally, a more successful alternative method of paint and corrosion removal was proposed, i.e., using a pneumatic needle scaler.

The needle scaling tool uses multiple fine metal needles to abrade the beam's surface to remove layers of paint and oxidized metal from the base metal and capture the particulate using suction from a vacuum. This method was the most effective surface preparation available because of the speed of removal, the enclosed nature of the removal process, and its ability to clean uneven surfaces, which was necessary for the corroded metal of the specimen webs. Further, the process could be used with a gasoline generator and transported to the lot where the beams were stored. This portability was necessary because of limitations on available space at the structures laboratory, as paint removal could be conducted at various locations without the need to allocate a specific area around the laboratory building. An example of this configuration is shown in Figure 4. The needle gun is shown connected to the laboratory's compressor by the

green pneumatic hose and an ultra-low-particulate air-filtered vacuum to collect the debris created by the gun.

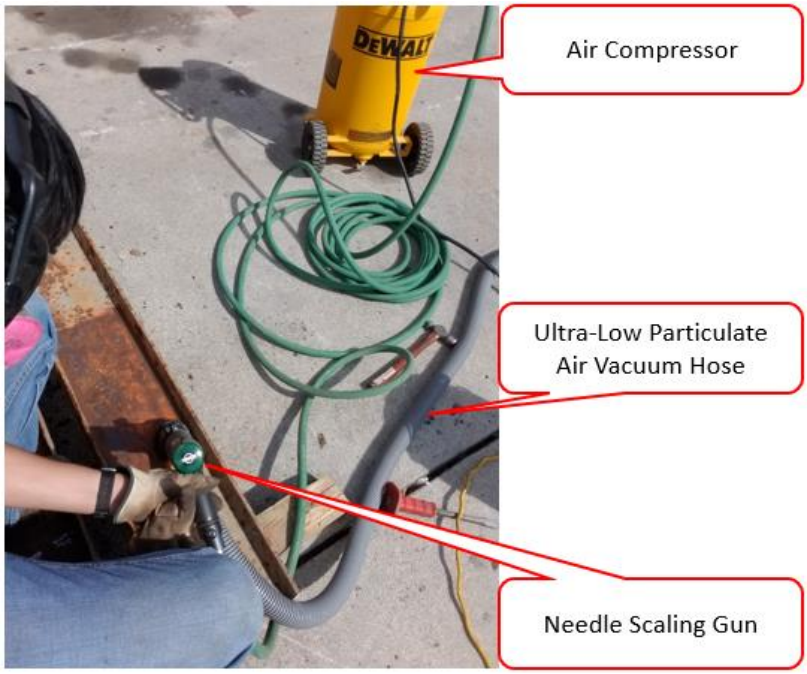

Figure 4. Pneumatic Needle Scaler Configuration

Test Setup and Instrumentation

The test setup consisted of a three-point beam loading test with a single applied load near the support to determine the shear capacity. The tests were carried out on a self-reacting steel load frame, resting on two W36x160 reaction beams. Test specimens were supported by a 6-in neoprene rubber bearing pad on top of a W21x68 beam at each end. The neoprene pads were used to replicate the in-field conditions of the specimens better and were chosen in favor of roller bearings because of the minimal translational displacement resulting from the near bearing loading point. The load frame was made up of two W12x53 columns connected by two coped W18x86 crosshead beams, which supported a 200-ton hydraulic cylinder used for loading. This cylinder was connected to a 10,000-psi pump with hoses equipped with ball-type quick couplings and a hydraulic tee adapter connected in series to allow for pressure readings taken using a pressure transducer. Figures 5 and 6 show diagrams of the load frame configuration from the front and side view.

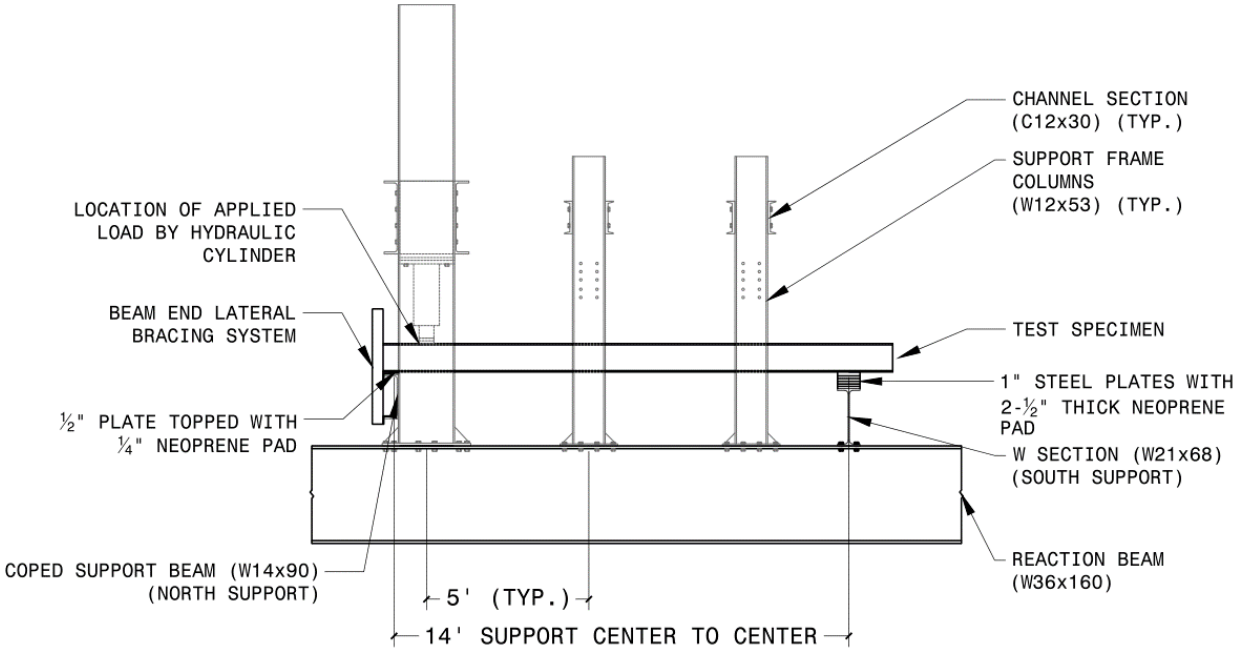

Figure 5. Elevation View of Full-Scale Beam Testing Configuration

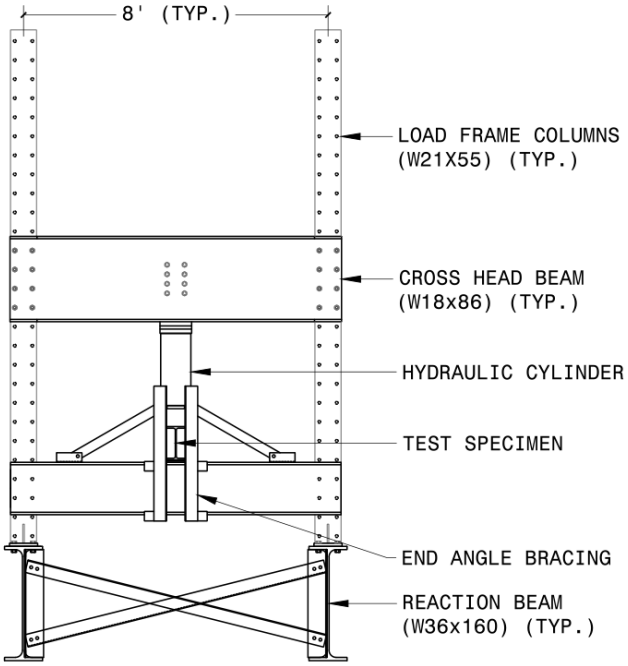

Figure 6. Transverse Elevation View of Full-Scale Beam Testing Configuration

The coped support beam shown in Figure 5 was moved to sit on the top flange of the reaction beams during the W16x45 and W21x62 load tests so that the load could be positioned farther from the bearing. As a result, the 1-in steel plates on the south support were moved to the north support to level the test specimen. In addition, lateral supports were added to brace the beams at 5-ft intervals from the loading point and at the beam end to prevent lateral torsional buckling and ensure that the beam would fail in shear. The beam end lateral bracing system first shown in Figure 6 was composed of a system of welded angles clamped to the loading frame

using heavy-duty bridge clamps. The beam end bracing is shown in Figure 7. This configuration was easily reassembled between beam tests and adjusted to various beam widths while providing enough stability to prevent beam torsion at the bearing during testing.

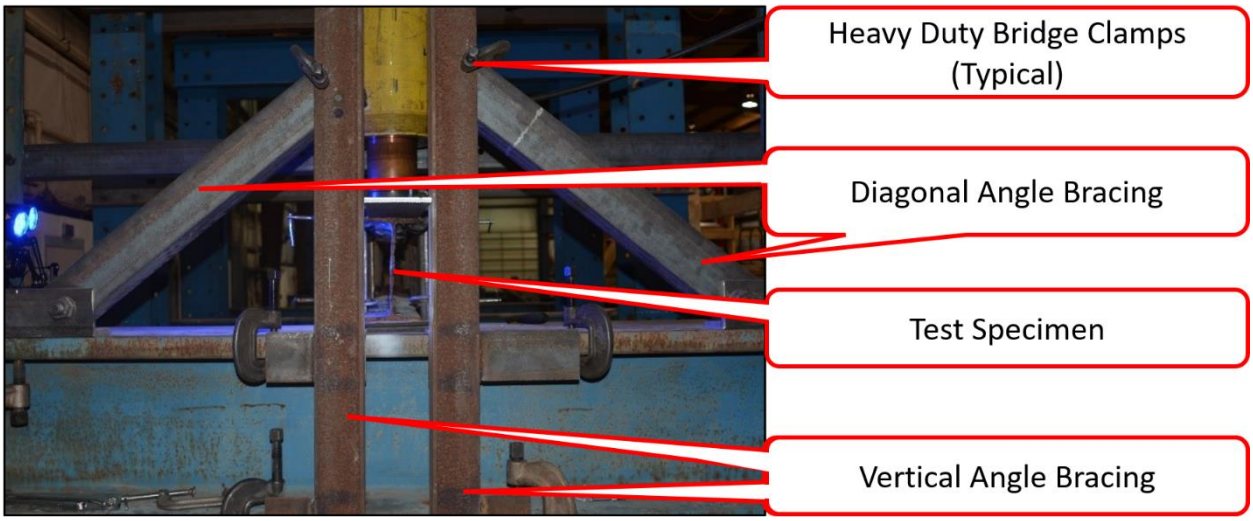

Figure 7. Beam End Bracing Configuration

Beams were loaded at varying distances from the support because of variation in beam size and the decision to move the load farther for deeper beams to maintain a similar shear state between beam sizes. This difference in load location is further discussed later in the report. Table 2 provides the distances between the loads and the edge of the north support. The distance between the load and the edge of the support was chosen instead of the distance to the midpoint of the support because loads applied to the beams during testing caused many of the specimens to lift at the beam end, contacting only the support at the edge. An advanced state of this behavior is shown in Figure 8 where significant amounts of deformation caused a clearly visible lift of the beam end. Figure 9 shows a drawing of the north support, including the bearing pads used, the positions of the lateral support structures, the beam height shown as "h," and the distance from the load to the support shown as "d."

The data were collected using a data acquisition system paired with a power supply. In addition, an analog output module was used to communicate the applied loads from the data logger to a digital image correlation (DIC) system described further in this section. A calibrated pressure transducer was connected to the hydraulic cylinder and used to determine the applied loads. In addition, a single string potentiometer was installed directly below the loading point to record the beams' vertical displacement during testing.

Table 2. Test Specimen Distances Between Applied Loads and Edge of Support

Test Set	Distance Between Load and Support, Distance *d* in Figure 9 (in)
S8x18.4	4
W10x26	4
W16x45	16
W21x62	21

Figure 8. Example of Beam Lifting at End Because of Applied Loads

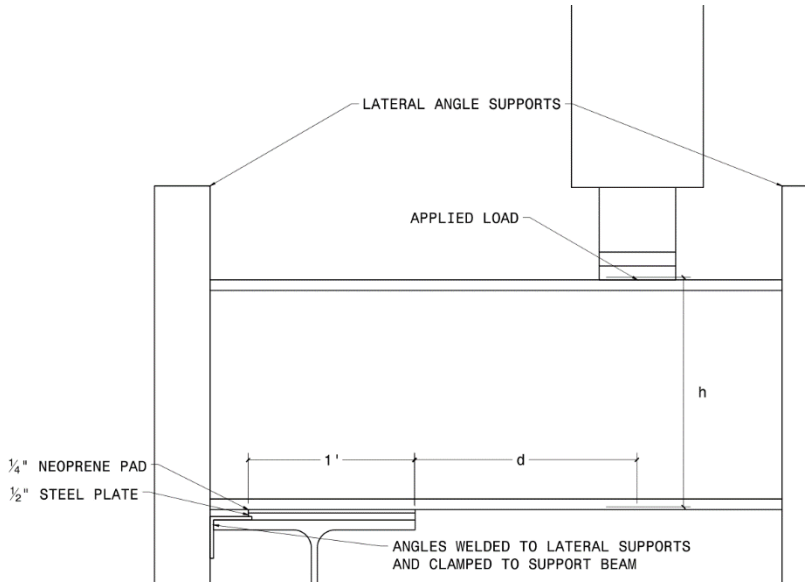

Figure 9. North Support View of Full-Scale Beam Testing Configuration

DIC Measurement System

Comprehensive strain fields of the beam webs were captured using the DIC system. This system replaced the need to use strain gauges by instead making use of an applied stochastic pattern. This pattern's application was a simple process. A primary coat of white spray paint was applied to the beam web to create a uniform base layer. The white paint was allowed to dry before a randomized series of black dots were painted overtop by applying a small amount of pressure to the nozzle of a black spray paint can. Figure 10 is an example of the system in use. The camera system projects a bright blue polarized LED light on the stochastic pattern, which was photographed throughout the loading process using a stereoscopic camera arrangement to identify displacements of individual points on the face of the webs.

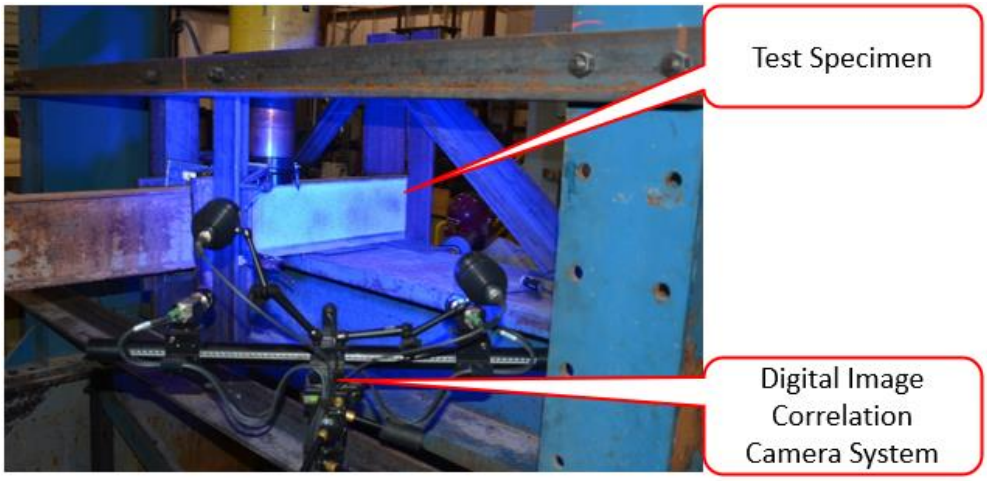

Figure 10. Digital Image Correlation Camera Scanning a Beam

It was essential to use contrasting paint colors (black and white in this case), high-resolution cameras, and constant bright lighting to ensure that the images taken were clear and consistent. The quality of these images ensured that the randomized points could be tracked between separate photographs taken throughout the loading process.

By use of the DIC software, the images taken were then converted into a surface model with a strain field based on the location of each point on the web before and during loading. This method removed the need to use an extensive series of strain gauges or multiple strain gauge rosettes that are time-consuming to apply. In addition, the DIC system was advantageous because strain gauges do not work well on uneven surfaces such as corroded metal.

Before each load test, the DIC software was used to convert images taken on each side of the undeformed beams into a 3D mesh, which was then referenced for the original beam's section loss measurements. These preliminary scans were achieved initially by taking images on both sides of the beams and marking five points where no corrosion had occurred on either side of the web, typically toward the upper flange where moisture did not accumulate during the bridge's service life. This process formed two separate meshes representing each side of the web. The marked points were then matched in the 3D point cloud, and mesh processing software was used to create a plane around which the mesh objects could be oriented. One of the meshes was then translated perpendicularly to the plane by a distance equal to the thickness of their uncorroded web to create a model of the corroded web, which included section loss from both sides of the web. This method was used for the first four beams; however, after a better understanding of the DIC system was gained, a more efficient process was determined and used for all of the following specimens.

The second method used a wooden board marked with five target dots and clamped to the top flange such that the DIC cameras could see the targets from either side of the beam. Thus, by matching the five marker points using the DIC software, a single web mesh could be generated with relative ease and more certainty of the accuracy of measurements made. Figure 11 illustrates the process by which DIC images were taken of the east and west faces of the beam end. The target dot boards marked with red dashed lines were matched in 3D space to align the surface models in the center of the figure shown as bright green rectangles.

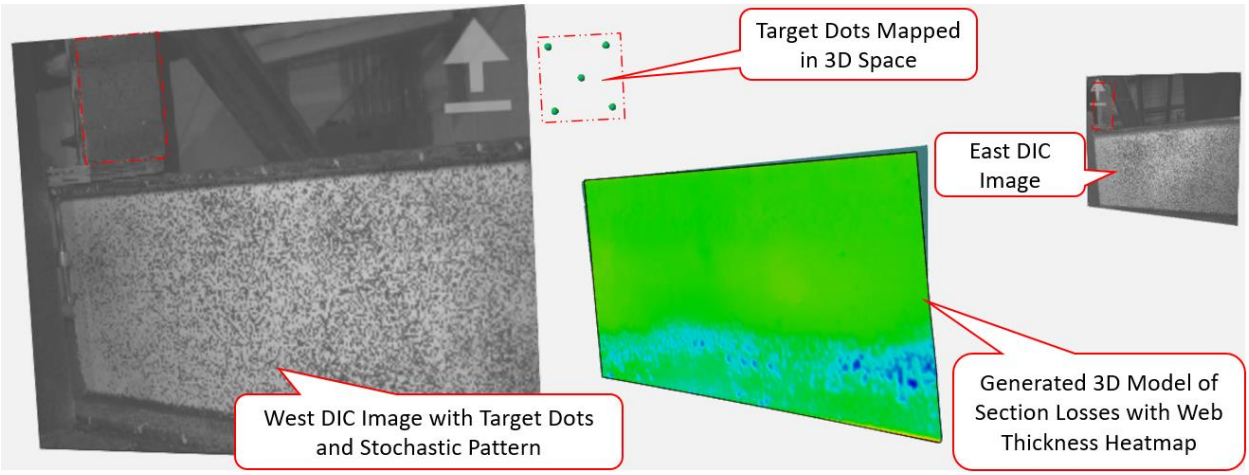

Figure 11. DIC Profile Scanning Using Target Dots. DIC = digital image correlation.

After the scanning process was completed, the deviation between the 3D surface models could be referenced to determine the remaining thickness of each beam digitally. Points were sampled from the 3D meshes at 0.5-in intervals for the S8x18.4 and W10x26 beams and 1-in intervals for the W16x45 and W21x62 beams. This difference in measurement interval was due to the DIC software's limitations on the number of sample points placed on a single scan. These sample points were then exported into a spreadsheet to create a matrix of thickness measurements referenced for web thickness data.

Specimen Set 1: S8x18.4 Beams

The first set of beams tested were S8x18.4 beams and featured heavy section losses because of corrosion spread across the beam end webs. A total of nine beams from a single bridge were brought to Virginia Tech in August 2018. Four beams with varying corrosion damage were selected for testing and assigned damage levels ranging from low to high. Images of these four beams with applied stochastic patterns are shown in Figure 12.

The first set of the deteriorated beams tested were the S8x18.4 shapes. These specimens came from a steel beam timber deck bridge that had severe localized corrosion on several beam webs and flanges. This deterioration was likely due to exposure to atmospheric moisture, roadway leakage, and moisture absorbed by the timber deck planks. Figure 13 shows an image of the first specimen tested after arrival at the structures laboratory at Virginia Tech. The first specimen was nearly undamaged except for some paint coating failure and minor corrosion near the beam end and small portions of the lower flange. An example of the first beam after cleaning is shown in Figure 14.

Specimen 2-S8-ML featured significantly more section loss than Specimen 1-S8-L. The decision to use this beam as the medium-low-damage specimen was driven by the presence of significant section losses without any through-web holes. As the study progressed, it became clear that the corrosion on Specimens 2-S8-ML, 3-S8-MH, and 4-S8-H was unlike most patterns characteristic of deck joint failure. The deterioration of a joint failure would follow the path of water runoff along the height of the beam end and near the bottom flange where water typically pools.

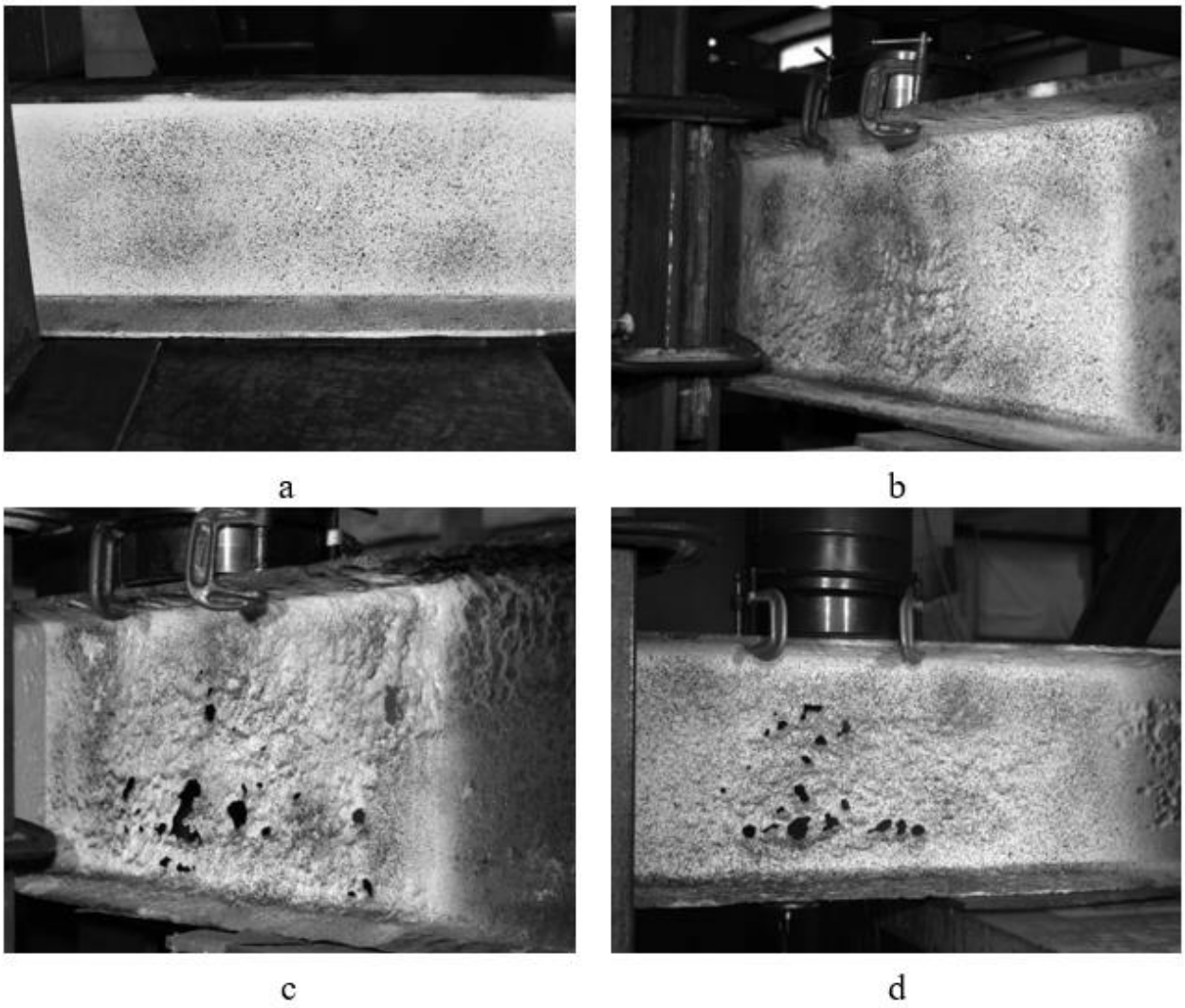

Figure 12. Photographs of S8x18.4 Beam End Specimens With Stochastic Patterns Showing Corrosion Damage: (a) 1-S8-L; (b) 2-S8-ML; (c) 3-S8-MH; (d) 4-S8-H.

The bridge this specimen came from was a steel beam bridge with a timber deck, making it likely that the timber deck absorbed water that was gradually released onto the beam along its entire length. This meant that the corrosion was not only the beam end but also throughout the entire length of the beam. Figure 15 shows an image taken of one of the bridge beams during service and illustrates this full-height web corrosion.

The medium-high-damage Specimen 3-S8-MH showed more significant section loss spread across the entirety of the studied area, including through-web holes. Further, the damage extended past the applied stochastic pattern toward the end of the beam. However, the specimen was positioned so that the applied load would be placed directly over most web holes to analyze the shear behavior around these defects.

Figure 13. Image of Specimen 1-S8-L After Arrival at Laboratory

Figure 14. Specimen 1-S8-L Stripped of Paint

Figure 15. Example of Steel Beam Timber Deck Web Corrosion

Specimen 4-S8-H was selected as the high-damage beam based on its holes' relative positioning since they were in the same vertical plane. If an analysis were to use the worst cross section as the defining corrosion measure for Specimen 3-S8-MH, it would be taken at the center of the large L-shaped hole in the lower half of the web in Figure 12c. For Specimen 4-S8-H, it would be taken along the column of holes directly below the load shown in Figure 12d.

In Figure 16, a comparative drawing of the cross sections illustrates the dimensions of these holes without the surrounding section losses. The ratio of hole to total web cross-sectional area between the flanges results in a 27% section loss for Specimen 3-S8-MH and a 33% section loss for Section 4-S8-H. When the specimen matrix was created, this simplified cross section was used as the rationale for assigning the condition rankings.

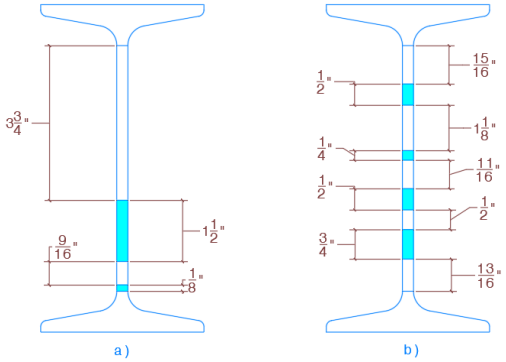

Figure 16. Comparison of Worst Cross Sections: (a) 3-S8-MH; (b) 4-S8-H.

Specimen Set 2: W10x26 Beams

The second set of beams tested were selected because of the limited availability of suitable beams between 10 and 12 in in height. Specimen 5-W10-L represented the low-damage configuration of the W10x45 beams and was selected from the available bridge beams because of its uniform profile. Despite this low-damage designation, all of the beams in this set showed less web corrosion and paint loss 3 in above the bottom flange. Figure 17 shows photographs of each of the corroded beam ends with applied stochastic patterns.

Specimen 6-W10-ML also exhibited low corrosion but was selected because of noticeable localized pitting damage in the lower 3-in band of corrosion mentioned before. This deep pitting continued intermittently throughout the length of the beam. The pitting caused various pinholes through the web; however, none was large enough for the DIC system to recognize. This is further discussed later.

The W10x26 beams selected did show significant corrosion; however, severe damage was found on only one beam in the set. Portions of this beam served as both the medium-high and high-damage specimen to provide the necessary range of damage for the test matrix. First, Specimen 7-W10-MH was loaded 1 ft from the beam's end. However, adjustments had to be made since the last 4 in of the span did not fully extend to the bracing to the north of the support to prevent lateral torsional buckling. A 2-ft steel plate was welded to the last 6 in along the top flange, shown at the top of Figure 17c. This plate extended across the north support to the two angle braces in place of additional beam length.

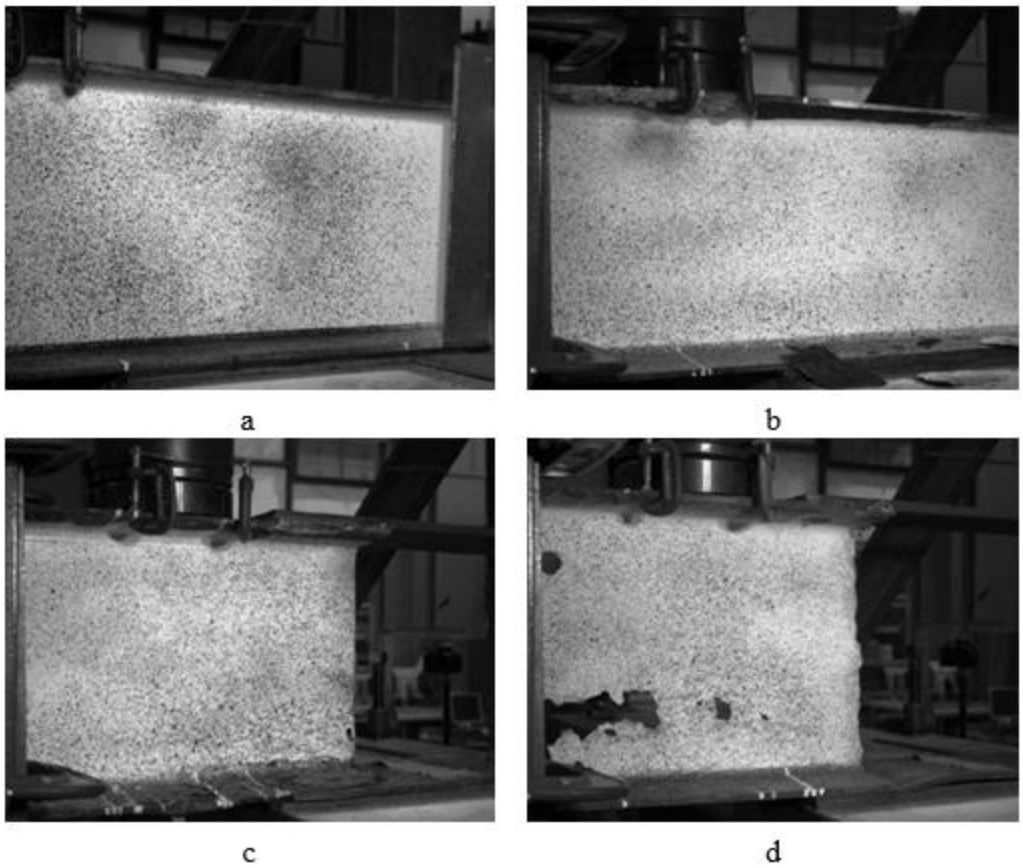

Figure 17. Photographs of W10x26 Beam End Specimens With Stochastic Patterns Showing Corrosion Damage: (a) 5-W10-L; (b) 6-W10-ML; (c) 7-W10-MH; (d) 8-W10-H.

After Specimen 7-W10-MH was tested, the band saw in the laboratory was used to cut off the deformed portion of the beam end. An additional steel plate was then welded to the top flange to allow for a similar test of the portion of the beam deemed the high-damage web section, Specimen 8-W10-H. Since the section was from the same beam as in the previous test, the 3.5-in longitudinal corrosion straddled the cut line between the two specimens. However, this beam also featured a substantial through-web opening, shown in Figure 17d.

Specimen Set 3: W16x45 Beams

The third set of beams comprised W16x45 beams that came from a completed bridge replacement. Concerns with the bridge's remaining capacity because of corrosion made this decommissioned bridge an appropriate candidate for testing. Six beams with varying levels of damage were transported by a contractor to the structures laboratory at Virginia Tech in February 2020. The low-damage specimen was selected from among the beams with minimal visible corrosion and intact coatings. Figure 18 shows images of all of the W16x45 corroded beam ends with applied stochastic patterns.

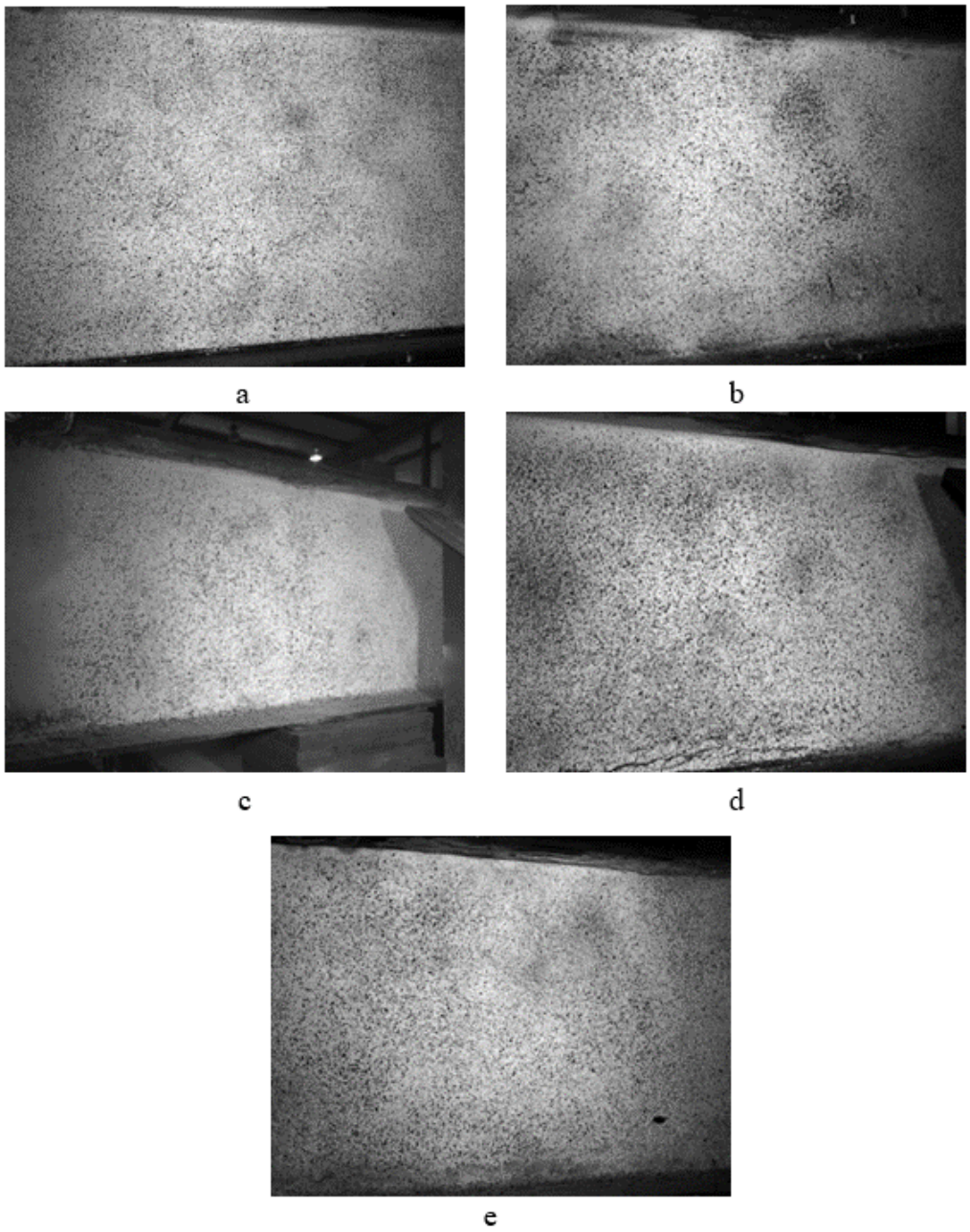

Figure 18. Photographs of W16x24 Beam End Specimens With Stochastic Patterns Showing Corrosion Damage: (a) 13-W16-L(A); (b) 9-W16-L; (c) 10-W16-ML; (d) 11-W16-MH; (e) 12-W16-H.

The distance from the inner face of the support to the load point was changed from a set 4 in to one beam height for the W16x45 beams. This change was made because the distance between the center of the applied load and the support's face was targeted to be equal to the beam height. The research team made the decision to modify the loading location after reviewing results from the first two sets of specimens to allow for a diagonal buckling limit state extending from the bearing point to the point of loading. Moving the load farther from the support enabled the web to fail in diagonal web buckling because of damage away from the bearing area in addition to web crippling. Thus, all W16x45 beams were positioned so that the distance between the load and the face of the support was 16 in.

Neither the medium-high-damage nor the high-damage beams showed any form of through-web holes. Thus, these sections were instead selected from beams showing severe localized web thinning, typically in the lower 3 in of the web directly above the bottom flange. The high-damage Specimen 12-W16-H showed similar corrosion patterns to the other three W16x45 beams; however, the lower web corrosion continued throughout its length.

Although the initial test matrix called for four of each beam size with varying levels of damage, an issue was found during the testing of Specimen 12-W16-H. This issue was that every beam end shared a common web-end thinning, which occurred naturally because of the bridge's age. The thinning meant that even the specimens deemed low- and medium-low-damage had this end thinning within at least the last 1 ft of the web. The team decided that a new alternate low-damage specimen should be tested to provide the full range of damage. One of the untested beams was cut 1 ft from its end to create an undamaged beam end without any form of thinning. This beam was given the designation 13-W16-L(A) and is referred to as the low-damage alternate specimen.

Specimen Set 4: W21x62 Beams

The W21x62 beam specimens were chosen from several candidate bridges selected because of the variation in corrosion damage visible on the web ends. However, four W21x62 beams were selected as the deepest specimens with minimal to through-web damage. The original four beams were approximately 45 ft long and were delivered to the structures laboratory at Virginia Tech in January 2020. Figure 19 shows images of the four beam ends after application of the stochastic pattern prior to testing.

Since the profile scans were conducted outside the laboratory, the full height could be captured by adjusting the camera focus at a far distance. However, because of the increased beam depth of these specimens and the loading frame constraints, the full web could not be captured by the DIC system during these 21-in beam tests. Figure 20 is an example of the DIC camera view for the medium-high-damage specimen and the initial testing scan. The flanges and web extremities are not visible.

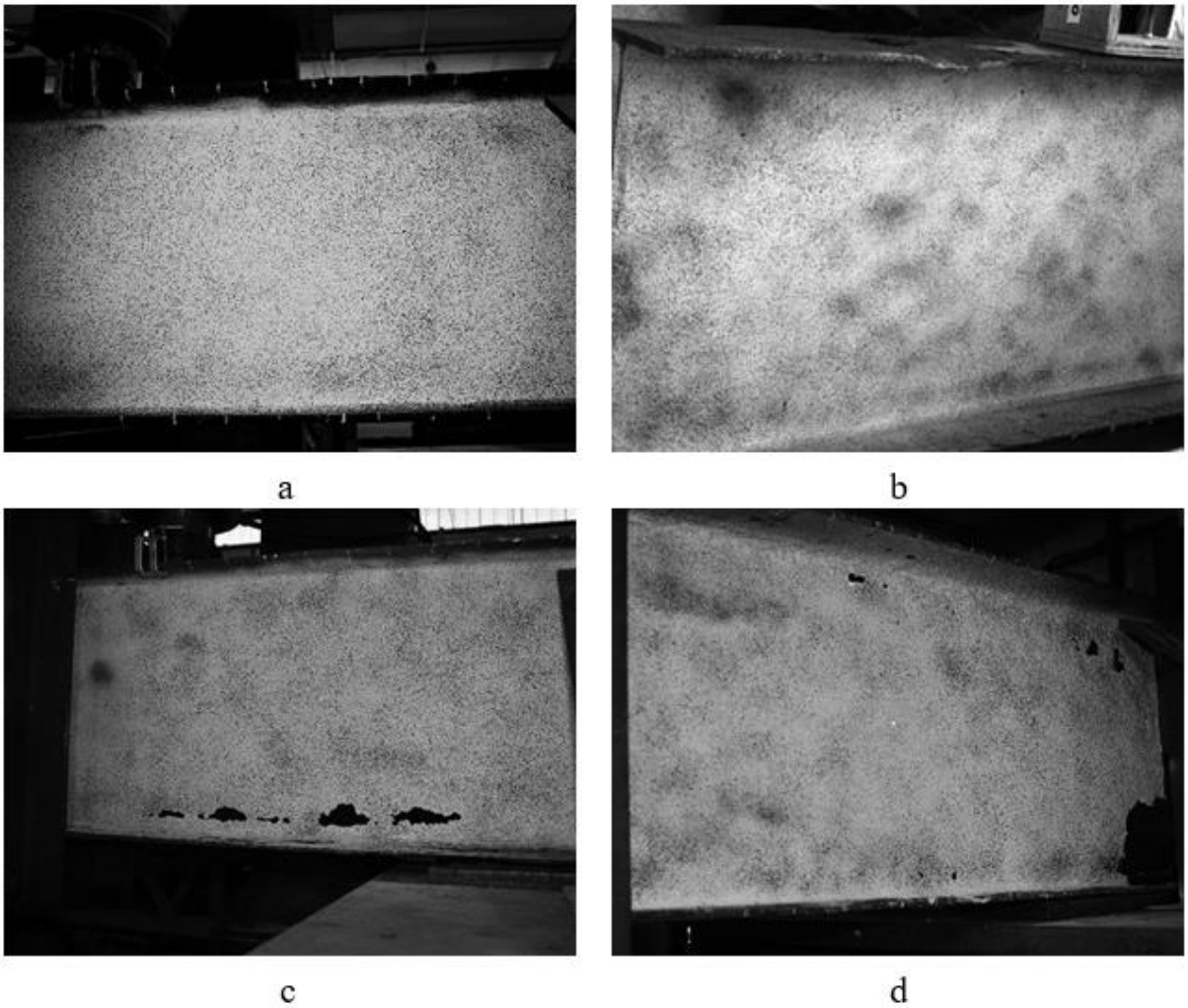

Figure 19. Photographs of W21x62 Beam End Specimens With Stochastic Patterns Showing Corrosion Damage: (a) 14-W21-L; (b) 15-W21-ML; (c) 16-W21-MH; (d) 17-W21-H.

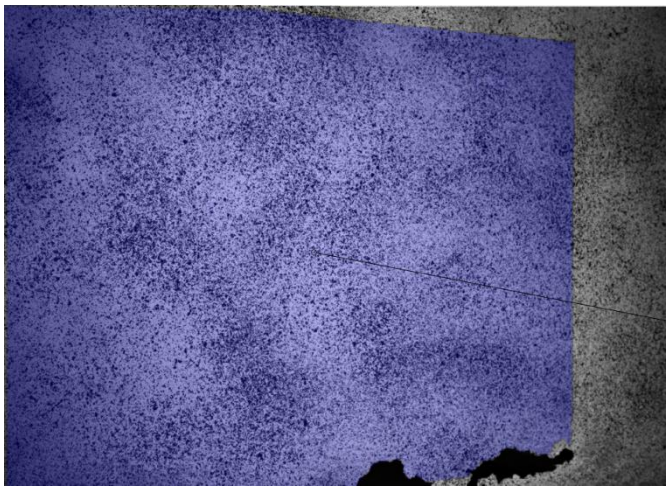

Figure 20. Specimen 16-W21-MH Camera View and DIC Displacement Field. DIC = digital image correlation.

Web Thickness Measurement

Five methods of calculating the remaining average web thickness were compared: minimum average, 45-degree average, area average, 3-in web height average, and 4-in web height average. The minimum average was determined by taking web thickness measurements at 0.5-in or 1.0-in vertical increments over the entire web height at a particular cross section and calculating the average web thickness. This process was repeated at 0.5- or 1.0-in horizontal increments, and the minimum web thickness of all of the cross sections was determined. The 45-degree average was determined by averaging the values in a straight line between the bottom of the web at the support's inner face and one beam height away at the top of the web. The area average was taken as the average of all the thickness matrix values between the interior face of the support and the applied load. Finally, the 3-in and 4-in web height averages were taken over the length of the support plus one beam height from the edge of the support. The five areas over which these measurements were compared are illustrated in Figure 21.

To take these measurements, each DIC profile scan was sampled at 0.5-in or 1-in intervals as described previously to obtain the web thickness measurements across the face of each specimen's web. Each of the colored boxes and lines in Figure 21 corresponds to the thickness measurement at each point on the web. These points were then exported as a thickness matrix and averaged over the areas described in Figure 21.

The profile scans were converted into colored heat maps. During loading, the DIC images were used to calculate the amount of displacement the material had undergone with respect to the original shape of the web, as well as the position of each point to the other points in the strain field surrounding it.

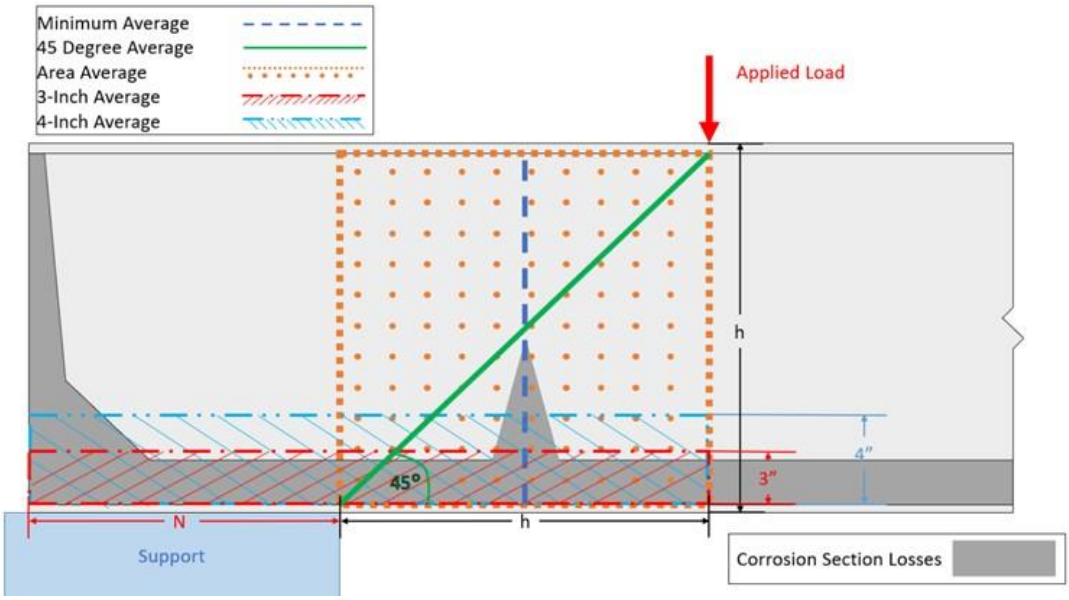

Figure 21. Methods for Calculating Average Web Thickness

As with a tensile test, this strain is calculated as the change in length of the material divided by the original length of a reference gauge length. Major strain, then, refers to the strain in the direction of maximum strain, or the direction on the web plane that the greatest change in material length has occurred for each point on the strain field.

Task 3: Comparison of Simplified Analysis Methods

The results of several shear capacity calculation methods were compared to the experimental results of Task 2 to determine their correlation to actual beam behavior. These methods included the following:

- *AASHTO LRFD Bridge Design Specifications*, 8th Edition (AASHTO, 2017)
- AISC 360-16: Specification for Structural Steel Buildings (AISC, 2016)
- Durability Evaluation Based on Buckling Characteristics of Corroded Steel Deck Girders (Sugimoto et al., 2006)
- Development of Steel Beam End Deterioration Guidelines (van de Lindt and Ahlborn, 2005)
- Remaining Capacity Assessment of Corrosion-Damaged Beams Using Minimum Curves (Rahgozar, 2009)
- LRFD for Composite Beams With Unreinforced Web Openings (Darwin and Donahey, 1988)
- Massachusetts Department of Transportation (MassDOT) *LRFD Bridge Manual* (MassDOT, 2020)
- Development of Load Rating Procedures for Deteriorated Steel Beam Ends (Tzortzinis et al., 2019a).

The goal was to find the most accurate method using a measured web thickness and facilitate implementation for VDOT load rating engineers.

Task 4: Incorporate Simplified Analysis Into BrR

Results from the experimental tests were compared to capacities calculated using BrR. When used to determine the shear capacity of a steel beam, BrR follows the provisions of the *AASHTO LRFD Bridge Design Specifications* (AASHTO, 2017). These provisions, described later, determine the minimum shear capacity of a beam web based on the shear-yielding and shear-buckling limit states.

The only requisite BrR input for modeling corrosion damage is the "Deterioration Profile" located in the "Member Alternatives" folder subtree in BrR. The deterioration profile allows a user to input a percentage of web thickness loss and the location of this thickness loss in terms of its start distance from a support and its relative length. Multiple web thickness losses and locations can be input to represent a steel beam with various amounts of corrosion on the web. The deterioration profile also allows for thickness losses to be input for both flanges and cover plates, if applicable. Since the shear capacity of a steel beam is dependent only on the web dimensions as defined in the *AASHTO LRFD Bridge Design Specifications* (AASHTO, 2017), only the web thickness loss inputs are discussed here. Figure 22 shows an example screenshot of the deterioration profile input for modeling web thickness loss in BrR.

The thickness matrices output from the DIC system were used to fill in the inputs for the deterioration profiles for each beam. Each beam was analyzed in BrR only over the area of interest, which was along the entire width of the support to the point of load application. Percent thickness losses were calculated based on the nominal web thickness of the intact beam shape and were input to the nearest 1%. The smallest length increment allowed by BrR for thickness loss in the deterioration profile is 0.5 ft. Therefore, the percent thickness loss was averaged for each 0.5-ft increment from the thickness matrices before it was entered into BrR. The first length increment began at the face of the support opposite the point of applied load. Increments then continued toward the point of applied load until the increment reached or passed the applied load location. Since the deterioration profile in BrR does not include an input for the height of the corrosion damage, thickness loss was assumed to be an average over the entire height of the web for each increment. The capacity for each deteriorated beam was then determined using BrR and was compared to the experimental test results. A trial-and-error process, discussed later, was then used to determine if different portions of the web could be used for modeling the deteriorated beams in BrR to achieve capacities that closely matched the experimental values.

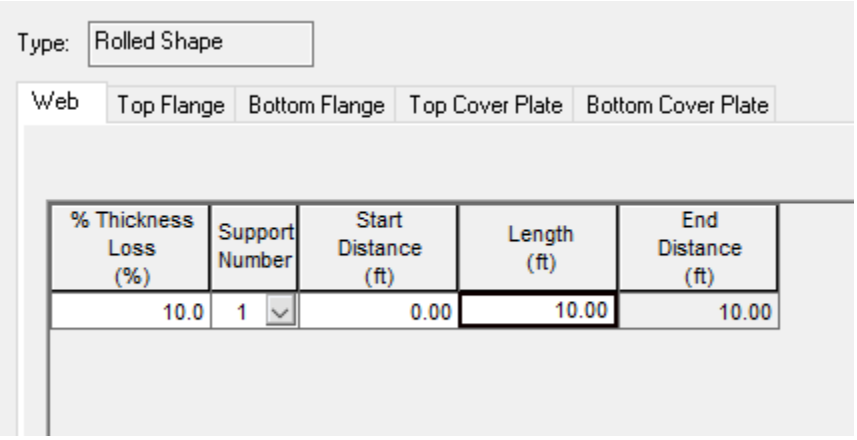

Figure 22. Example Screenshot of Deterioration Profile Input for Modeling Web Thickness Loss in BrR

RESULTS AND DISCUSSION

Task 1: Literature Review

Several methods to determine the shear capacity of steel beams assume that beams maintain a constant cross section for some length of the beam, which introduces difficulty when

assessing corroded beams. A corroded cross section may be uneven and unsymmetrical, making accurate measurement and calculation of the sectional properties challenging to achieve. In addition, this damage may or may not be continuous over the beam's length, which is not accounted for with an assumed cross section. Inspection reports often simplify the damage to an assumed web thickness reduction over an area, which can potentially result in a loss of fidelity of the actual dimensions. Although more precise measurements can be taken given the time, it is not practical to do so for every structure with corrosion because of the sheer number of aging bridges in VDOT's inventory. The following studies proposed several methods for addressing beams with corrosion that may also be applied to the beams used in this study.

Early Work Concerning Beam End Deterioration (Kayser and Nowak, 1989)

Initial research regarding the behavior of corroded steel beams was conducted by Kayser and Nowak, whose report *Capacity Loss due to Corrosion in Steel-Girder Bridges* set a basis for all studies concerning steel beam corrosion behavior (Kayser and Nowak, 1989a). In this study, corrosion source, rate, and pattern were analyzed to determine their effect on the structural capacity of simple span steel girders. The parameter for expressing loss of material because of corrosion was referred to as "loss per surface," calculated by taking the area of an affected surface and dividing it by the average depth of the material loss within that area. This measure's advantage is that the affected area's entirety can be quantified rather than a specific cross section along the beam's length being addressed.

Kayser and Nowak determined that an initial linear relation exists between the surface loss in the web near the girder end and the shear and bearing capacity of the girder. After some indefinite quantity of thickness loss, this relation became nonlinear, and the capacity rapidly decreased for shear and bearing. Curves representing this relationship between the loss per surface measurement and the percent remaining shear and bearing capacity were then created as part of the study. The initial linear relationship for bearing capacity can be preserved if stiffeners designed to AISC or AASHTO specifications are used. However, the non-linear relationship for shear capacity occurs regardless. Conclusions from this study were that flexure ceases to be the governing failure mode for bridges with severe corrosion. The shear and bearing relation found in this study applies specifically to four beam sizes: W36x230, W36x182, W30x116, and W24x76. As such, these curves may not be directly used to estimate the remaining shear capacity in VDOT's inventory of bridges, which consists of many different beam shapes.

This second study conducted by Kayser and Nowak was similar to their first and identified the importance of girder slenderness and web compression on bridge reliability when the effects of corrosion are discussed (Kayser and Nowak, 1989b). The study stated that the plate slenderness of compression elements most heavily influences the safety of steel plate girder bridges. Thus, the steel web plates, primarily in compression, were most susceptible to thickness losses because of corrosion and the corresponding increase in slenderness. This observation demonstrated that the governing failure mode can change because of corrosion damage, which was addressed in the capacity loss study. In addition, the absence of bearing stiffeners on short-span bridges with high corrosion levels was observed to reduce bridge reliability significantly over a 50-year life cycle.

Michigan State Department of Transportation (MDOT) Study and Capacity Ratio Curves (van de Lindt and Ahlborn, 2005)

MDOT had previous issues with corrosion of steel girder bridges attributed to exposure to road salts. Their method of assessing the remaining strength of bridges exhibiting significant section losses had been through finite element (FE) analysis of individual structures or application of the simplified method, which they had found too conservative (van de Lindt and Ahlborn, 2005). A set of 16 out-of-service bridges was selected for a study to determine their remaining capacity because of corrosion damage. To facilitate this, 3-ft-long sections of damaged girders were taken from bridges and loaded to induce buckling or crushing. FE programs were used to estimate the governing failure mode, and each specimen was loaded in a test frame to confirm the models' accuracy. Results showed a good correlation between the FE models and the capacities from testing.

A set of design charts was created to relate the measured damage height and depth to the remaining capacity expressed by a deterioration factor, Ψ_d, using these data. This method allowed for a remaining bearing capacity correlating to the prior test results to be determined quickly given the damage measurements. This deterioration factor method was then compared to the simplified MDOT reduced section calculations using formulas from LRFD. The correlation was not entirely clear. In some cases, the deterioration factor gave more conservative estimates of capacity than the simplified method. This behavior could be partially attributable to the oversimplification of section loss parameters in the simplified method. Assuming the FE study represented actual beam behavior, estimated capacity typically increased using this modified MDOT method. This method would give load raters additional leeway in determining the adequacy of existing structures before requiring posting for reduced capacity.

Durability Evaluation and Presentation of a Simplified Method (Sugimoto et al., 2006)

After the work of Kayser and Nowak in 1989, there was an absence of studies regarding corroded beam capacities during the 1990s. However, because of an aging infrastructure of highways and expressways in the United States and Japan, the early 2000s saw increased interest concerning bridge maintenance efforts. This period was when Sugimoto et al. conducted a study regarding the durability of steel deck girders and the scientific literature regarding the field of corroded beam capacities began to see publications (Sugimoto et al., 2006).

In the Sugimoto et al. study, the topic of discussion was the aging steel railway infrastructure of Japan. Predating the extensive expressway network constructed after World War II, railways had been an essential function in Japanese society since their introduction in the 1800s. Thus, the deterioration of aging steel deck girders required a capacity evaluation method that prioritized the repair and replacement of Japanese railway bridges. It was noted in this study that ultimate strength evaluation methods at the time relied on assumed values of steel properties, the existing beam size, and the degree of corrosion, which were regarded as "uncertainties." As a result, the study included experimental testing on out-of-service steel plate girders from a railway bridge built in 1904.

Following the flexural tests on the out-of-service girders, a second series of shear strength tests was conducted on a plate girder with artificially accelerated corrosion patterns created using a saltwater spray. Testing was applied with a single point shear load near a roller bearing, resulting in an out-of-plane web buckling. This behavior was again approximated in an FE analysis program to prove the validity of FE analysis in predicting the behavior. As a result of these tests, it was determined that the location of section losses did not predominantly determine the capacity of the beam. Instead, the remaining strength was governed by an average web thickness measured along a diagonal line from the support. Further, a simplified strength evaluation method was determined for the bearing and shear strength of plate girder structures. Regarding shear, a relation was found between the average plate thickness reduction ratio in Equation 1 and the shear buckling strength in Equation 2.

$$R_{tavg} = \frac{t_0 - t_{avg}}{t_0} \quad \text{[Eq. 1]}$$

where

R_{tavg} = average plate thickness reduction ratio
t_0 = design plate thickness
t_{avg} = average residual plate thickness.

$$R_{P_{rc}} = \frac{P_{cr}}{P_{cr(0)}} \quad \text{[Eq. 2]}$$

where

R_{Prc} = shear buckling strength ratio
P_{cr} = shear buckling strength in a corroded state
$P_{cr(0)}$ = shear buckling design strength.

The average plate thickness was measured along a 45-degree slant perpendicular to the web plate's shear force to determine the governing corrosion measurement used in the equation. Assuming the critical applied shear load was located at a distance equal to one web height away from the end of the support, this 45-degree line designated the web area affected by the direct flow of forces between the applied load and the support. Using the average web thickness along this path, in theory, accounted for the damage sustained along the web's critical section.

Remaining Capacity Using Minimum Curves (Rahgozar, 2009)

Following Sugimoto et al., Iranian researcher Rahgozar (2009) conducted an analytical study that looked at the remaining capacity of corroded beam models to establish minimum curves that could be used to predict the remaining strength of several universal beam sections. The study proposed that U.S. visual inspection methods are not rigorous enough to evaluate a bridge's corrosion conditions adequately.

Calculations by Rahgozar (2009) concerning shear capacity refer to British Standard 5950, Part 1, from 1985, which provides the following equations for calculating the critical shear strength (q_{cr}):

$$q_{cr} = 0.6p_{yw} \text{ for } \lambda_w \leq 0.8 \quad \text{[Eq. 3a]}$$

$$q_{cr} = 0.6p_{yw}[1 - 0.8(\lambda_w - 0.8)] \text{ for } 0.8 < \lambda_w < 1.25 \quad \text{[Eq. 3b]}$$

$$q_{cr} = q_e \text{ for } \lambda_w \geq 1.25. \quad \text{[Eq. 3c]}$$

where

q_{cr} = critical shear strength of a plate girder web panel
p_{yw} = web design yield strength
q_e = elastic critical shear stress
λ_w = equivalent web slenderness factor.

$$\lambda_w = \sqrt{\frac{0.6p_{yw}}{q_e}} \quad \text{[Eq. 4]}$$

The minimum curves established in this study allowed for the remaining capacity to be estimated using a measured percent loss of the web thickness. The percent remaining shear capacity determined from the curves could then be applied directly to the undamaged beam strength. Additional curves were provided throughout the study to be used for beams with varying degrees of corrosion referred to as damage categories including the following:

Category 1: where the web depth to thickness ratio $\frac{d}{t} \leq 63\sqrt{275/p_y}$
Category 2: where the web depth to thickness ratio $\frac{d}{t} > 63\sqrt{275/p_y}$.

Regarding the applicability to the current study, these curves are applicable only to a maximum web thickness loss of 25%. The existing curves could be extrapolated to estimate the capacity at higher section losses; however, the accuracy of these curves is not guaranteed past the known data points.

Tzortzinis et al. (2019) and MassDOT Methods (MassDOT, 2020)

A more recent study concerning steel beam corrosion was conducted at the University of Massachusetts, Amherst. MassDOT inspection data were analyzed to understand the most common damage patterns and locations for bridges with beam-end corrosion (Tzortzinis et al., 2019a). In total, 93 structures and 732 total corroded beams were used as subjects for the study. Deterioration patterns were split into two groups: general corrosion and holes. Within these groups, six general corrosion patterns and four through-web hole patterns were identified as representative of beam end section losses in the raw data gathered from the MassDOT inventory. Pattern data from bridge inspection documents were compiled into spreadsheets, and a computer script was generated to extract the data from all of the spreadsheets into a single data set. This

data set was then used to make several critical statistical observations about the state of beam end corrosion behavior, with 18 characteristic corrosion patterns identified through the statistical post-processing script. These observations include potential links between these characteristic corrosion patterns, alluding to a typical evolution between subsets of these observed patterns. In addition, analytical modeling was proposed for these 18 corrosion patterns to determine their effects on the remaining capacity of deteriorated girders.

Further work in association with MassDOT yielded a 2019 report regarding an effort to load rate deteriorated steel beam ends (Tzortzinis et al., 2019b) with experimental work and FE modeling. The experimental tests began with six corroded beam specimens selected from a set of beams from the replaced Colrain and Charlemont bridges in Massachusetts. These beams were chosen because of their limited distortion and the presence of corrosion. The loading test configuration was a beam-end shear test with an applied load located 5 ft from the beam end support. Each beam was fitted with strain gauges, potentiometers, linear variable differential transducers, load cells, and pressure transducers. The load test results are tabulated in Table 3, along with the predicted capacities using the existing MassDOT equations for shear capacity.

Table 3. Experimental Results of Load Testing (Tzortzinis et al., 2019b)

Specimen No.	Bridge	Beam Type	Max. Applied Load (kips)	Bearing Failure Load (kips)	Prediction (kips)
1	Colrain	33WF125	134.1	99.1	38.3
2	Colrain	33WF132	91.3	67.6	102.2
3	Colrain	33WF125	112.5	84.3	0
4	Charlemont	21WF73	53.3	42.8	91.5
5	Charlemont	21WF73	45.1	30.9	17.6
6	Charlemont	21WF59	58.8	40.9	6.1

Following the load testing, a set of FE models were created to model different corrosion behaviors outside those exhibited in the actual specimens. The previous 2019 pattern study was referenced, and a computer script was created to automate the creation of corrosion scenarios run by the FE analysis program. Several corrosion patterns were applied to the beam shapes with varying degrees of thickness loss, and several curves were generated for various beam shapes. These curves were then used to modify existing MassDOT shear capacity equations to fit the capacity curves better using various constants.

The corroded web factored resistance is taken as the minimum of the calculated nominal yield and crippling capacity shown in Equation 5 and Equation 6, respectively:

$$R_{n,yield} = F_y t_{ave}(2.5k + N) \quad \text{[Eq. 5]}$$

where

t_{ave} = average remaining thickness within the bottom 4 in of the web height (in)
k = distance from outer face of flange to web toe fillet (in)
N = bearing length (in).

$$R_{n,crip} = \left(\mathrm{c}\sqrt{EF_y t_f}\, t_{ave}^{1.2} + \mathrm{d}\left(\frac{(N-H)}{d}\right)\frac{\sqrt{EF_y t_f}}{t_f^{1.5}}(t_{ave})^3\right)\left(\frac{t_{ave}}{t_{web}}\right)^{\mathrm{h}} \quad \text{[Eq. 6]}$$

where

t_f = flange thickness (in)
H = length of hole along length used for capacity (in)
t_{web} = nominal web thickness of the intact section
d = beam depth
c, d, and h = corroded web equation coefficients as defined in Table 4.

Table 4. Modified MassDOT Equation Coefficients (Tzortzinis et al., 2019b)

Coefficient	Imperfection Amplitude		
	1 t_{web}	**0.5 t_{web}**	**0.1 t_{web}**
c	0.33	0.32	0.38
d	0	0.17	0
h	0.4	0.2	0.15

The t_{ave} term is the calculated average web thickness considering web holes presented in Equation 7 as follows:

$$t_{ave} = \frac{(N+md-H)t_w}{(N+md)} \quad \text{[Eq. 7]}$$

where

m = average web thickness factor defined in Table 5
t_w = remaining web thickness (defined over the bottom 4 in of the web in the study).

Table 5. Proposed Values of Factor *m* for Average Web Thickness Calculation (Tzortzinis et al., 2019b)

N/d Ratio	Imperfection Amplitude		
	1 t_{web}	**0.5 t_{web}**	**0.1 t_{web}**
>0.2	0.2	0.2	0.1
≤0.2	0.1	0.1	0

Calculations to determine web-crippling capacities were modified forms of previous MassDOT formulas found in the MassDOT *LRFD Bridge Manual*. The initial coefficients in these formulas were based on linear regression used to determine the impact of several variables describing beam geometry and corrosion severity. The proposed MassDOT equation for corroded web resistance is provided in Equation 8:

$$\text{Corroded web factored resistance} = \mathrm{Min}\left[\phi R_{n,yield}, \phi R_{n,crip}\right] \quad \text{[Eq. 8]}$$

where

$\phi_{yield} = 1.0$
$\phi_{crip} = 0.8$.

These equations can undoubtedly be applied to the specimens in the current study. This study is the most relevant of those in the current literature by addressing rolled shapes without stiffeners and presenting a method for capacity calculation for beams with end corrosion. The only significant difference is the size of the beams tested. The current study targets much smaller rolled sections, common in older and rural structures.

In January 2020, MassDOT released a revision to their bridge load rating guidelines, which had not been incorporated into the Tzortzinis study (MassDOT, 2020). The revision defined the area over which the corroded web thickness must be measured as the bottom 4 in of the web multiplied by the bearing length plus 2.5 times the web flange fillet (k) on either side of the bearing (Figure 23). In addition, it makes clear that although a buckling capacity procedure was previously determined, that procedure was not included in the revision because of overly conservative results.

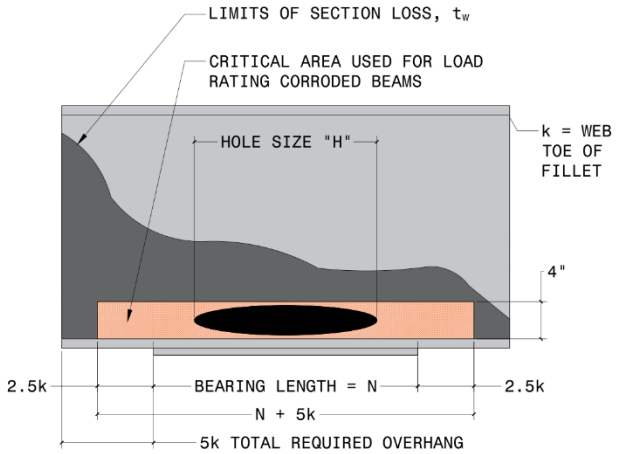

Figure 23. End of Beam Elevation Describing the Deteriorated Beam End

The calculation for the adjusted average web thickness in Equation 7 was also modified as presented in Equation 9:

$$t_{ave} = \frac{(N+5k-H)t_w}{(N+5k)} \quad \text{[Eq. 9]}$$

This modified Equation 9 does not include the *m* factor presented in Table 5 and instead defaults back to the previous MassDOT equation. Instead, if an overhang past the bearing of less than 5k is provided, then the *"5k"* term in the equation should be substituted with *"2.5k."* Similarly, the factors presented in Table 4 were also excluded from the MassDOT revision procedure. Equation 10 shows the MassDOT version of the crippling capacity calculation; the nominal yield capacity is the same as Equation 8. At interior pier reactions and for beam end reactions applied at a distance from the end of the member that is greater than or equal to d/2:

$$R_{n,crip} = 0.8t_{ave}^2 \left[1 + 3\left(\frac{(N-H)}{d}\right)\left(\frac{t_{ave}}{t_f}\right)^{1.5}\right]\frac{\sqrt{EF_y t_f}}{t_{ave}} \quad \text{[Eq. 10a]}$$

Otherwise:

$$R_{n,crip} = 0.4t_{ave}^2 \left[1 + 3\left(\frac{(N-H)}{d}\right)\left(\frac{t_{ave}}{t_f}\right)^{1.5}\right]\frac{\sqrt{EF_y t_f}}{t_{ave}}, \text{when N/d} \leq 0.2 \quad \text{[Eq. 10b]}$$

$$R_{n,crip} = 0.4t_{ave}^2 \left[1 + \left(\frac{4(N-H)}{d} - 0.2\right)\left(\frac{t_{ave}}{t_f}\right)^{1.5}\right]\frac{\sqrt{EF_y t_f}}{t_{ave}}, \text{when N/d} > 0.2 \quad \text{[Eq. 10c]}$$

These equations were unchanged from the previous versions of the MassDOT *LRFD Bridge Manual*. Modifications reflecting recommendations from the Tzortzinis et al. study have not yet been incorporated.

Web Openings in Steel Beams (Darwin and Donahey, 1988)

Outside of studies specifically targeting corroded beam capacity, studies have been conducted regarding the effects of web openings in steel beams. Darwin and Donahey (1988) completed such analyses at the University of Kansas to determine the capacity of composite beams with holes through the steel webs, such as those used to route utilities through buildings. In their 1988 study, Darwin and Donahey proposed a method for determining the shear capacity of beams with web openings by summing the individual shear capacities of beam sections above and below the opening (Darwin and Donahey, 1988). However, the composite concrete component was not expected to be used for the current study. Thus, Darwin and Donahey's calculation for the maximum shear capacity of the non-composite bottom tee may be used (Equation 11).

$$V_{b\,max} = V_{pb}\left(\frac{\lambda\sqrt{3}}{\sqrt{3}+\frac{a_0}{s_b}}\right) \quad \text{[Eq. 11]}$$

where

$V_{b\,max}$ = maximum shear capacity of the bottom tee
λ = constant used in linear approximation of von Mises yield criterion
a_0 = length of the opening
s_b = height of the bottom tee
V_{pb} = plastic shear capacity of the bottom tee, calculated as follows:

$$V_{pb} = \frac{F_y}{\sqrt{3}} t_w s_b \quad \text{[Eq. 12]}$$

where

F_y = yield strength of steel

t_w = web thickness.

Equation 12 can also be applied to the top tee in the case of a non-composite beam, where the top tee's height would replace the value of s_b. The total maximum shear capacity would then simplify to Equation 13:

$$V_{max} = F_y t_w \lambda \left(\frac{s_b}{\sqrt{3}+\frac{a_0}{s_b}} + \frac{s_t}{\sqrt{3}+\frac{a_0}{s_t}} \right) \quad \text{[Eq. 13]}$$

where

s_t = height of the top tee.

AASHTO LRFD Shear Capacity Calculations (AASHTO, 2017)

The shear capacity of corroded steel bridge beams may be determined using AASHTO and AISC calculations using modified section properties. The VDOT Structure and Bridge Division Instructional and Informational Memorandum Number IIM-S&B-86.4 (VDOT, 2020) calls for using AASHTO LRFR code to evaluate the remaining capacity in existing structures. The AASHTO calculations for shear capacity of unstiffened webs are provided in *AASHTO LRFD Bridge Design Specifications* and are as follows (AASHTO, 2017):

$$V_n = CV_p \quad \text{[Eq. 14]}$$

where

V_n = nominal shear capacity
C = ratio of shear buckling resistance to shear yield strength (Eq. 15b-d)
V_p = plastic shear capacity, calculated as follows:

$$V_p = 0.58 F_y D t_w \quad \text{[Eq. 15a]}$$

$$\text{if } \frac{D}{t_w} \leq 1.12\sqrt{\frac{Ek}{F_y}} \text{ then } C = 1.0 \quad \text{[Eq. 15b]}$$

$$\text{if } 1.12\sqrt{\frac{Ek}{F_y}} < \frac{D}{t_w} \leq 1.40\sqrt{\frac{Ek}{F_y}} \text{ then } C = \frac{1.12}{(\frac{D}{t_w})}\sqrt{\frac{Ek}{F_y}} \quad \text{[Eq. 15c]}$$

$$\text{if } \frac{D}{t_w} > 1.40\sqrt{\frac{Ek}{F_y}} \text{ then } C = \frac{1.57}{(\frac{D}{t_w})^2} * \frac{Ek}{F_y} \quad \text{[Eq. 15d]}$$

where

D = web depth
t_w = web thickness
k = shear buckling coefficient (= 5 if unstiffened, actual 5.35).

The AASHTO equations for shear capacity apply to the AASHTO critical section for shear, defined as an applied load located one beam height away from the support.

AISC Shear Capacity Calculations (AISC, 2016)

The equations used in AISC 360-16 to calculate shear capacity are shown in Equations 16a, b, and c (AISC, 2016):

$$V_n = 0.6F_yA_wC_v \quad \text{[Eq. 16a]}$$

where

A_w = web area ($= dt_w$)
d = web depth (for rolled shapes, the distance between flanges less the fillet)
t_w = web thickness
k_v = shear buckling coefficient (= 5.34 for webs without transverse stiffeners)
h = the clear distance between flanges
C_v = web shear strength coefficient, calculated as follows:

$$1.0 \text{ when } \frac{h}{t_w} \leq 1.10\sqrt{\frac{k_vE}{F_y}} \quad \text{[Eq. 16b]}$$

$$1.10\frac{\sqrt{\frac{k_vE}{F_y}}}{\frac{h}{t_w}} \text{ when } 1.10\sqrt{\frac{k_vE}{F_y}} < \frac{h}{t_w} \quad \text{[Eq. 16c]}$$

It should be noted that the web thickness used in these formulas is for webs of uniform thickness, so to apply it to a corroded section, an assumed thickness must be used.

Task 2: Large-Scale Flexural Tests

Steel Coupons

Steel coupons cut from the webs of each beam set were tested in tension in accordance with ASTM E8 (ASTM International, 2021). A 220-kip uniaxial load frame with a 22-kip load cell was used to load each specimen in tension. Each coupon was pulled until failure to produce a stress-strain curve used to determine the elastic modulus and steel grade of each beam set. The load frame was equipped with a load cell to record the applied tensile loads, and a non-contact laser extensometer was used to measure the coupon displacement during testing. Table 6 tabulates the calculated material properties received from these tests.

Table 6. Steel Properties From Beam Coupon Samples

Beam	Elastic Modulus (ksi)	Yield Strength (ksi)	Ultimate Strength (ksi)	Elongation at Yield
S8x18.4	29,027	38.7	62.2	0.00363
W10x26	29,879	42.4	62.9	0.00342
W16x45	29,665	50.0	74.1	0.00189
W21x62	29,693	57.3	66.8	0.00296

DIC Scanned Beam Profiles

Figures 24 through 27 represent the beam web thicknesses measured using the DIC system. These web measurements are given as heat maps, which show changes in thickness as variations in color gradient ranging from blue and green representing little or no section loss to red, which denotes significant section losses. A scale is provided on the right side of each figure that defines the colors corresponding to varying web thicknesses. In addition, some heat maps include holes that could signify either through-web deterioration or, in some cases, errors made by the DIC during stochastic pattern recognition. The commentary accompanying each figure differentiates between web holes and capture defects if this applies. The web section captured using the DIC scans does not encompass the full beam length. Scans depict only the web thickness of the last 1 to 6 ft of the beam (depending on the beam depth and DIC field of view) of 16 to 17 total ft of beam length. The captured sections were selected to demonstrate which portions of the web were engaged during loading, typically between the applied load and the beam end. Each section ends with a table of average web thicknesses, which were created using the thickness measurements taken from these DIC beam scans. The results of the five averaged web thickness values are tabulated at the end of each specimen subsection.

Specimen Set 1: S8x18.4 Beams

The first set of specimen scans are presented in Figure 24, where the applied load is shown at the top of each subfigure marked as a red arrow and the bearings are at the bottom as black arrows. It should be noted that although bearings appear to vary in length between specimens, all bearing lengths were 12 in, but the black arrows continue only to the extent of the image taken, cutting some of the bearing lengths short. This is also true for all of the remaining heat maps.

Because of Specimen 1-S8-L being the low-damage beam, there is nothing of note about the surface profile outside of the fact that few noticeable section losses were present. In Figure 24a, small amounts of section loss can be seen toward the top of the web in green. However, the depth of these deformities is approximately 0.06 in or slightly less than 1/16 in. For the purpose of this study, Specimen 1-S8-L can be compared to a new beam as these losses equate to a highly localized 2% thickness loss. This type of damage is insignificant by the measure of any of the studies mentioned in the literature review. The multiple holes present on the figure's left and right are due to the DIC camera failing to recognize points on the painted stochastic pattern.

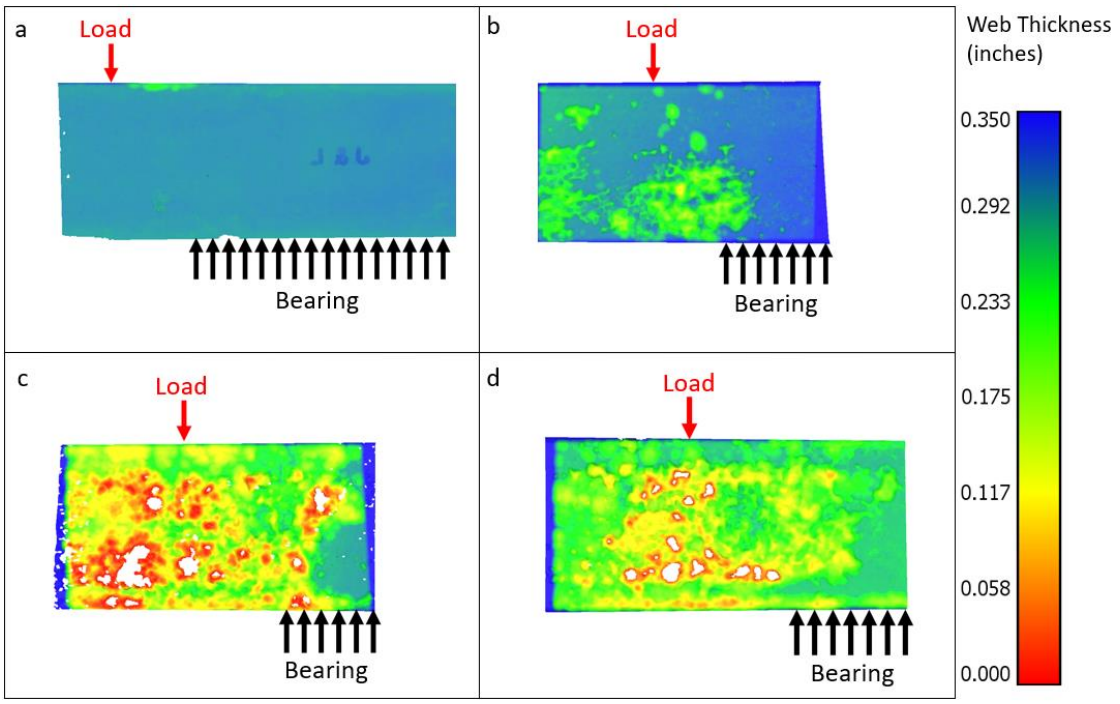

Figure 24. Heat Maps Showing Web Thickness of S8x18.4 Beam End Specimens: (a) 1-S8-L; (b) 2-S8-ML; (c) 3-S8-MH; (d) 4-S8-H.

The corrosion on Specimen 2-S8-ML was scattered across the beam surface but was mostly targeted within the lower 4 in of the web. Figure 24b shows the heat map of the distance between the east and west profile, representing the thickness of the steel at that location. The green portion of the beam was approximately 10.4 in in length, and the corrosion from the left side of the green area extended for about 8.9 in. The DIC scan taken for the east profile was larger than for the west profile because the camera angle used for the west image was suboptimal. The S8x18.4 beams were all scanned with the DIC system while in the load frame, which restricted the positions where the camera could be placed. Later profile scans were taken outside the load frame for this reason.

Specimen 3-S8-MH showed two large holes in the lower web with multiple smaller holes scattered across the surface. In addition, numerous deep corrosion pits were formed across the height and length of the beam. Most of the smaller holes in the blue and green regions in Figure 24c were again because of stochastic pattern recognition errors; however, web pinholes were present in the specimen within the red regions.

Figure 24d shows the presence of multiple holes grouped in a 6-in-wide band of the web, with most openings grouped near the bottom. In addition, the orange areas demonstrated a 0.16-in thickness loss, which surrounds the holes in this band. Further web thinning appears directly above the bottom flange. Following the issues with the profile scan of Specimen 3-S8-MH, the scan of Specimen 4-S8-H was conducted outside the load frame. The beam was elevated on concrete cinderblocks inside the laboratory so that the DIC camera could be moved freely without the need to take images from steep angles.

Table 7 shows all of the average areas for the S8x18.4 beams as defined in Figure 21. Because of the highly irregular corrosion patterns present on the first test set, the measured beam averages were close for all five measurements. Because of the prevalence of holes throughout the beam height, the minimum cross-section average was typically the most conservative measure of section loss. However, the W10x26, W16x45, and W21x62 beam sets did not show similar results because their section losses were typically focused on the bottom 3 in of the web.

Table 7. Web Thicknesses of S8x18.4 Specimens Based on Different Methods

Specimen	Minimum Cross Section (in)	45-Degree Average (in)	Area Average (in)	3-in Average (in)	4-in Average (in)
1-S8-L	0.271	0.271	0.271	0.270	0.271
2-S8-ML	0.225	0.241	0.237	0.236	0.240
3-S8-MH	0.126	0.120	0.159	0.140	0.147
4-S8-H	0.125	0.162	0.172	0.170	0.220

Specimen Set 2: W10x26 Beams

The uniform corrosion in Specimen 5-W10-L amounted to approximately 0.03 in of thickness loss, which was the least of any of the W10x45 shapes tested. The deepest section losses appear as green on the heat map in Figure 25a; however, they still represent only about 0.05 in of loss.

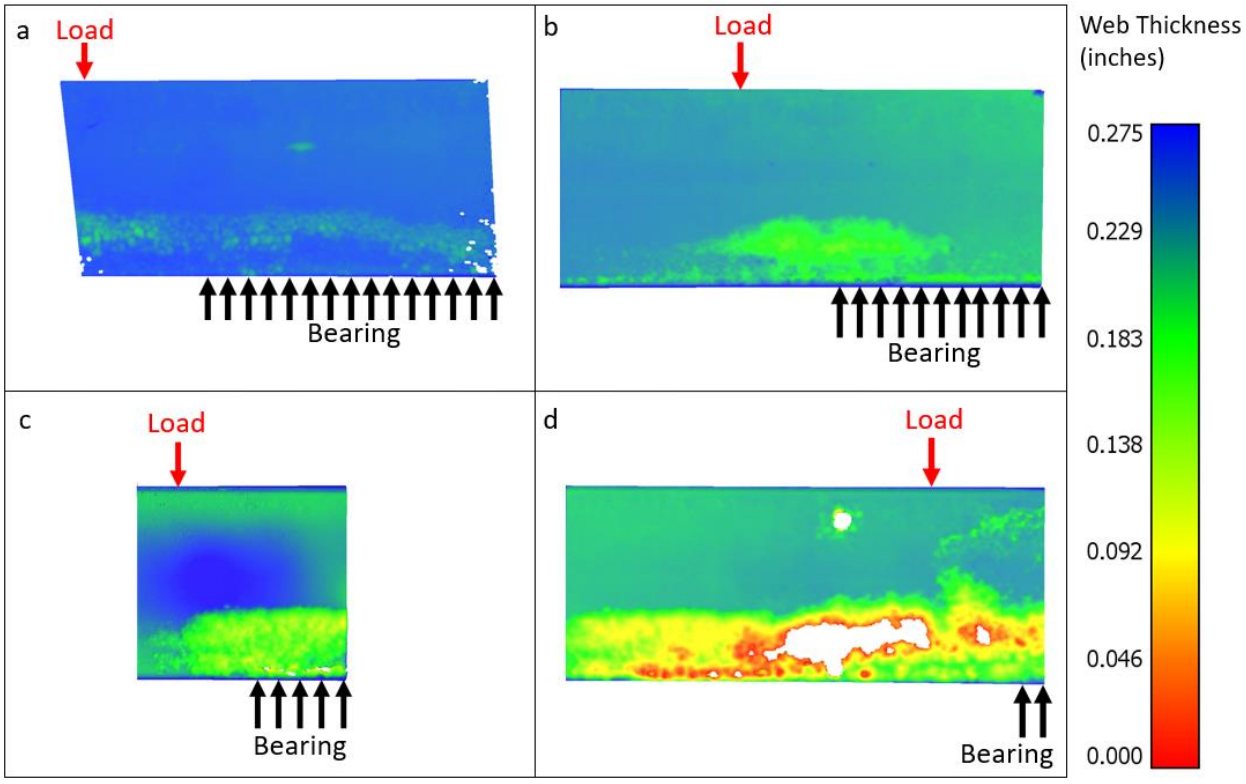

Figure 25. Heat Maps Showing Web Thickness of W10x26 Beam End Specimens: (a) 5-W10-L; (b) 6-W10-ML; (c) 7-W10-MH; (d) 8-W10-H.

The profile scan for Specimen 6-W10-ML in Figure 25b showed that the pitting ranged from 0.06 to 0.11 in of section loss, represented in green. The area of section loss measured 9.5 in from edge to edge and 3 in in height from the beam's bottom. In addition, the strip of section loss directly above the bottom flange measured 0.5 in in height and was continuous along the beam's length.

The corrosion-affected web area in Specimen 7-W10-MH is shown in the bottom right corner of Figure 25c near the beam end. This damage comprised six through-web holes at 0.5 in above the bottom flange and a relatively uniform section loss in the lower 3.5 in of the web extending the full length of the stochastic pattern.

The most significant damage in Specimen 8-W10-H was the large web opening extending 3.4 in in width and 2.6 in in height, the largest single hole in any test. However, the applied load was placed near the north end of this large hole. If the load had been placed farther south, the capacity would have been negligible because of the absence of any material capable of resisting shear forces. Two additional web holes may be seen at the top of the web and to the right of the large web hole in Figure 25d. Since this circular hole did not lie between the applied load and the support, it was not expected to contribute to the beam capacity reduction. Therefore, crack initiation was expected to begin at either the hole in the bottom right of Figure 25d or the pinhole directly to its right. The pinhole was too small for the DIC software to identify as a web opening. Instead, the DIC software modeled it as a severe section loss, visualized in Figure 25d as a red spot near the scan's right edge.

The average web thickness values presented in Table 8 show that the 3-in average was the most conservative measure of the web thickness except in the case of Specimen 8-W10-H because of the presence of large web holes located away from the bearing area, which was excluded from the 3-in and 4-in averages. In addition, the 3-in average did not include the entire height of the yellow section loss band in Figure 25d, which gave a much higher average than the other specimens.

Table 8. Web Thicknesses of W10x26 Specimens Based on Different Methods

Specimen	Minimum Cross Section (in)	45-Degree Average (in)	Area Average (in)	3-in Average (in)	4-in Average (in)
5-W10-L	0.256	0.253	0.257	0.253	0.255
6-W10-ML	0.247	0.249	0.251	0.243	0.248
7-W10-MH	0.191	0.169	0.197	0.118	0.139
8-W10-H	0.193	0.199	0.205	0.213	0.154

Specimen Set 3: W16x45 Beams

Figure 26 shows the web thickness heat maps of the W16x45 beams. These beams are discussed in order of testing from 9 to 13; however, the order of Figure 26 begins with the lowest-damage beam, Specimen 13-W16-L(A). Specimen 9-W16-L was used as the best damage condition despite showing extensive section losses at the beam end. However, the damage seen to the beam's right was not expected to contribute significantly to failure. The 0.1-in damage shown as green and yellow in Figure 26b extends toward the inner face of the support. Although the shear test outcome is discussed further later, this test did not end with a diagonal

web buckling between the applied load and the support. This irregular behavior prompted the fifth W16x45 beam to be tested, the low alternate Specimen 13-W16-L(A).

Specimen 10-W16-ML was selected as the medium-low-damage beam because of web section losses near the bottom flange across its length, which is characteristic of corrosion patterns caused by water pooling. Damage to the W16x45 beams was relatively consistent with this lower web loss pattern, and the order of severity was selected based on the presence of localized damage. Upon visual inspection, Specimen 10-W16-ML showed relatively low amounts of section losses on both sides of the web, ranging from 0.04 to 0.2 in of total web thickness loss, as shown in Figure 26c. It should be noted that the web scans for Specimen 10-W16-ML do not continue to the applied load location because of the range of the DIC camera. The red arrow representing the load is placed approximately where the point load was applied during testing to the left of the scan.

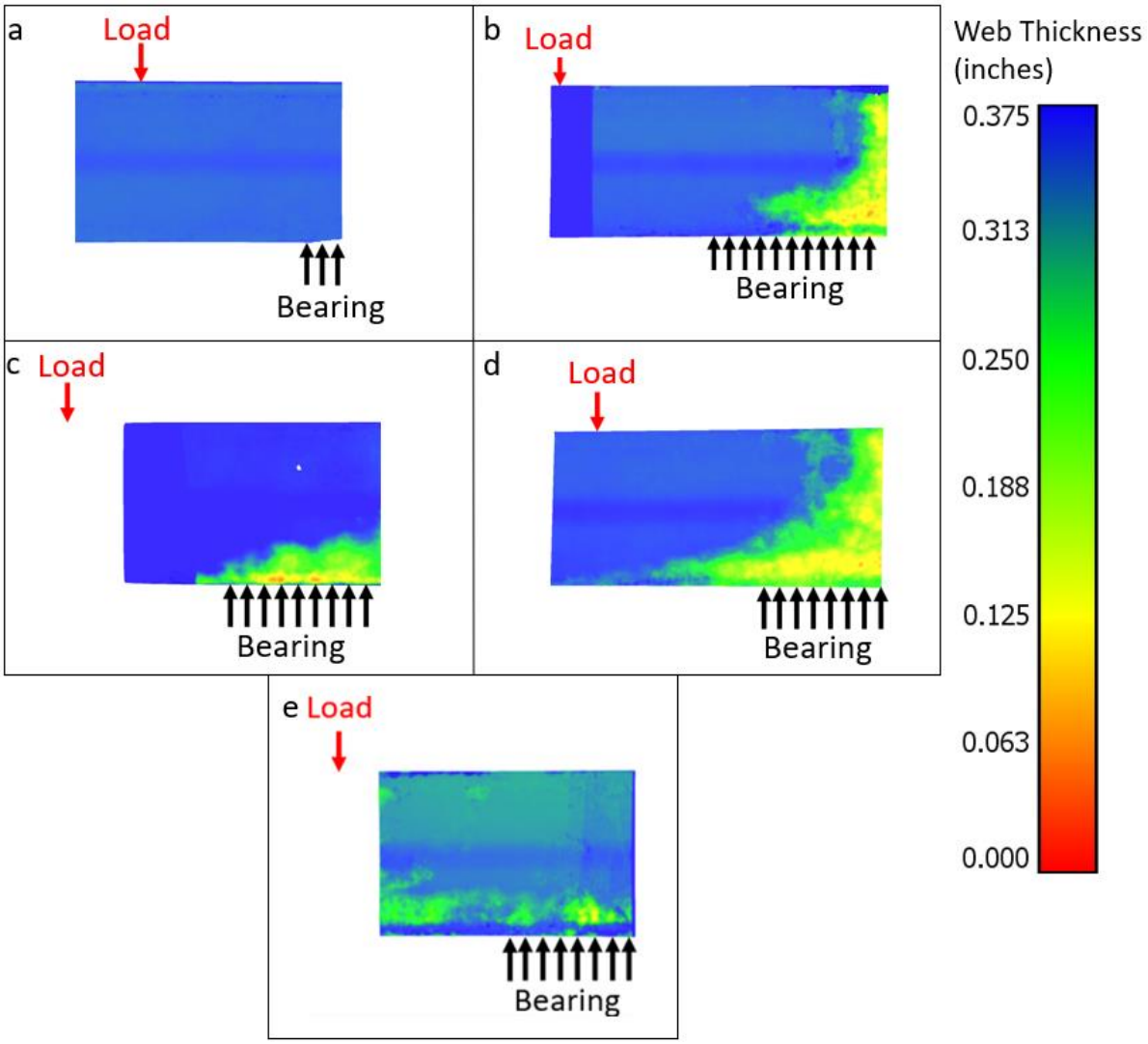

Figure 26. Heat Maps Showing Web Thickness of W16x45 Beam End Specimens: (a) 13-W16-L(A); (b) 9-W16-L; (c) 10-W16-ML; (d) M1-W16-MH; (e) 12-W16-H.

The heat map scan of Specimen 11-W16-MH shows similar damage to Specimen 9-W16-L, but the section losses continue farther into the length of the beam. The total thickness loss amounted to 0.15 to 0.25 in, which appears in the color range of green to yellow in Figure 26d.

The heat map for Specimen 12-W16-H shown in Figure 26e shows multiple locations of deep thickness losses in the lower 4.5 in of the web. The comparatively low damage of this beam set's high-damage specimen compared to the other beam sets is due to the presence of longitudinal stiffener repairs made to the higher-damage beam ends. As such, no beams with through-web holes were available for testing.

Variation in the heat map is at a maximum of 0.02 in of thickness reduction in Figure 26a. Compared to the rest of the beams, the surface profile for Specimen 13-W16-L(A) was the most uniform because it was taken from the interior of the span from the retired bridge. As a result, it was expected that the capacity of Specimen 13-W16-L(A) would be closest to those calculated using AISC and AASHTO shear formulas for undamaged members.

Using the 3-in web method for the W16x45 beams again showed the most conservative estimate of the beam capacity because of the presence of the characteristic web corrosion pattern because of a leaking deck joint. In the case of Specimens 9-W16-L, 10-W16-ML, and 11-W16-MH, the corrosion damage did not extend far past the support and the 3-in average was the only method in which the area of interest (shown in Figure 21) was fully encompassed by portions of the web with section loss and did not include any web portions without corrosion (see Table 9).

Table 9. Web Thicknesses of W16x45 Specimens Based on Different Methods

Specimen	Minimum Cross Section (in)	45-Degree Average (in)	Area Average (in)	3-in Average (in)	4-in Average (in)
9-W16-L	0.261	0.262	0.262	0.187	0.187
10-W16-ML	0.324	0.296	0.330	0.183	0.212
11-W16-MH	0.308	0.315	0.334	0.159	0.177
12-W16-H	0.330	0.335	0.337	0.301	0.306
13-W16-L(A)	0.337	0.337	0.338	0.337	0.337

Specimen Set 4: W21x62 Beams

Figure 27 shows the web thickness heat maps of the W21x62 beams. Despite being the low-damage specimen, Specimen 14-W21-L still showed a fair amount of section losses throughout its length. This was due to the history of the W21x62 bridge beams, as they were sourced from a storage yard and were sitting outdoors for several years before delivery to the Virginia Tech structures laboratory. All of the W21x62 beams had some section loss, but Specimen 14-W21-L had the least amount of damage. The heat map in Figure 27a shows the extent of this section loss, ranging from 0.1 to 0.25 in of total thickness reduction.

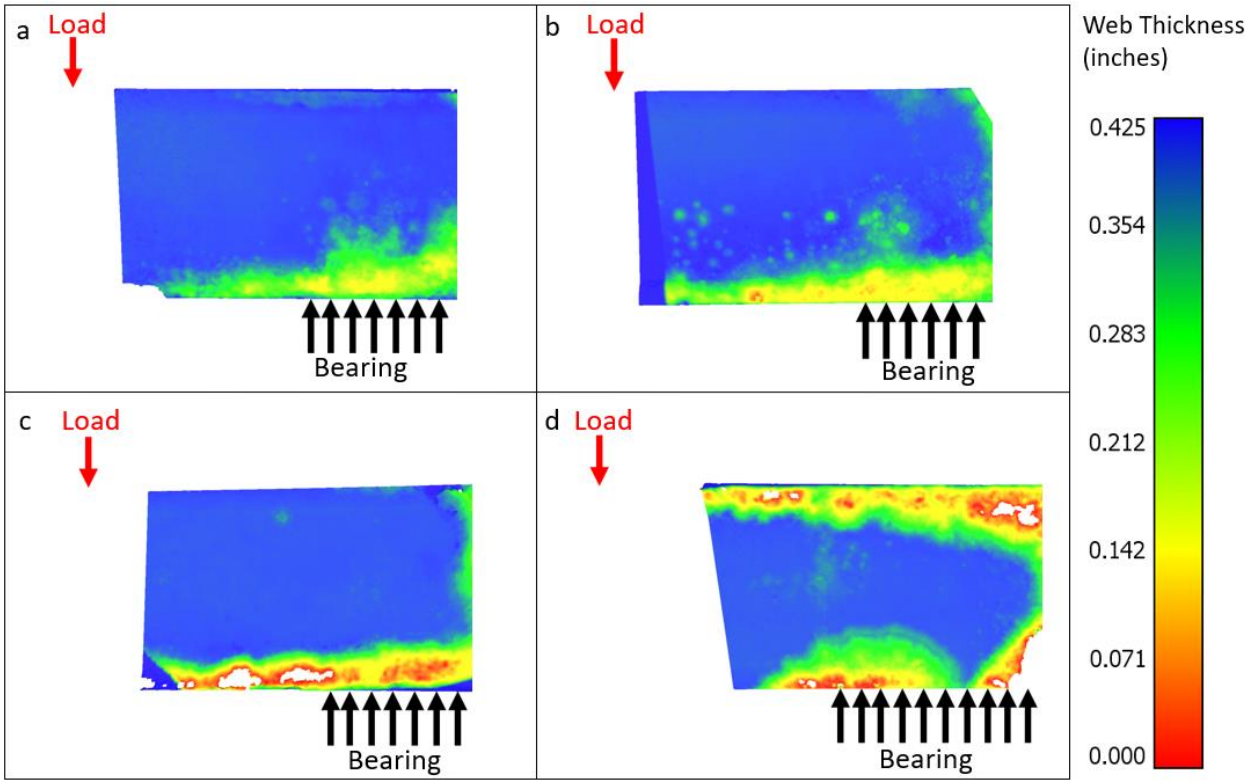

Figure 27. Heat Maps Showing Web Thickness of W21x62 Beam End Specimens: (a) 14-W21-L; (b) 15-W21-ML; (c) 16-W21-MH; (d) 17-W21-H.

The damage on Specimen 15-W21-ML showed a slightly more uniform lower web section loss than on Specimen 14-W21-L. In Figure 27b, the 0.25-in thickness losses in yellow continue across the scan's length at an average height of 2 in from the bottom flange. In addition, 0.1- to 0.15-in section losses were scattered throughout the lower half of the web, shown as green blotches. The missing corner at the top right of the scan was due to the DIC camera's orientation during the profile scanning process.

Specimen 16-W21-MH was selected as the medium-high-damage beam because of multiple through-web holes located between the applied load and the support. The thickness loss band shown near the bottom of Figure 27c measured 3 in in height. The damage ranged between 0.25 in of thickness loss shown in yellow to near-total section loss shown in red.

The section losses on Specimen 17-W21-H were heavily concentrated near the top and bottom of the web shown in Figure 27d. It should be noted that the beam's original in-service orientation was inverted for this load test (i.e., top of the beam in service served as the bottom of the beam during testing). This orientation was used because the web-end angle bracing could not support the highly deteriorated top flange. As a result, the concentrated web section losses in the 3-in corrosion band were positioned at the top of the web. Additional localized section losses can be seen at the bottom of the web.

The W21x62 beam set again showed that the 3-in average gave the most conservative estimate of the remaining web thickness (Table 10). Of all the beam tests, the W21x62 beams most resembled the corrosion patterns expected from bridges with compromised deck joint

leaking. The results of using these averages to estimate beam capacity are further discussed later.

Table 10. Web Thicknesses of W21x62 Specimens Based on Different Methods

Specimen	Minimum Cross Section (in)	45-Degree Average (in)	Area Average (in)	3-in Average (in)	4-in Average (in)
14-W21-L	0.387	0.389	0.401	0.245	0.259
15-W21-ML	0.364	0.363	0.376	0.174	0.214
16-W21-MH	0.344	0.348	0.354	0.131	0.186
17-W21-H	0.294	0.341	0.325	0.203	0.230

Load Versus Displacement Data

The web height to thickness ratios for the nominal specimen shapes are provided in Table 11, along with the calculated web slenderness values from Table B4.1a, Case 5, from AISC 360-16. The height to thickness ratios of these beams were above the slenderness ratio for the W16x45 and W21x62 beams, meaning they were slender members; the S8x18.4 and W10x26 beams were not slender. The S8x18.4 members did not exhibit web crippling or yielding, so this distinction did not apply. Finally, web compression cracking occurs because of web holes that cause high concentrations of stresses during loading. Shear stresses generated during loading use these openings as initiation points for web cracking, often propagating toward other nearby web openings, the web to flange fillet, and the beam end. The loads required to initiate web cracking are often sudden and unpredictable and are not typically addressed in the shear failure literature.

Table 11. Web Height to Thickness Ratios for the Four Tested Specimen Shapes

Specimen Shape	Web Height (in)	Web Thickness (in)	h/t_w Ratio	Slenderness Ratio
S8x18.4	6.00	0.271	22.14	40.81
W10x26	8.25	0.260	31.73	39.55
W16x45	13.63	0.345	39.51	32.51
W21x62	18.38	0.400	45.95	33.92

S8x18.4 Beams: Tests 1-4

The load curves for the first set of S8x18.4 beams were as expected; however, it should be noted that the data gathered for Specimen 1-S8-L were more linear than for the others (Figure 28). The first test was performed with the string potentiometer placed away from the applied load because of restrictions on available space. Because comparing data gathered in this alternate position to those of the other S8x18.4 beam tests would be inappropriate, the displacements for Specimen 1-S8-L were instead determined using DIC measurements. For this specific case, displacement measurements were averaged from five sampled points placed along the bottom flange fillet. These locations were selected to reduce the influence of vertical displacement because of web deformation.

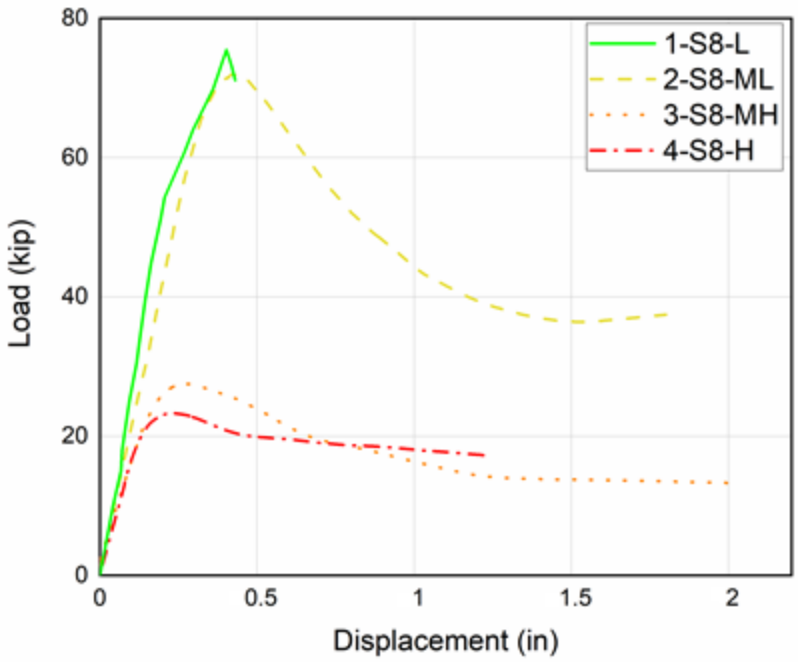

Figure 28. Load vs. Displacement Data for S8x18.4 Beams

The load versus displacement data for the S8x18.4 beams all showed similar linear elastic behavior before yield. This similarity was surprising for Specimens 3-S8-MH and 4-S8-H, as they had very irregular beam profiles because of severe corrosion across the full height and length of their webs. Table 12 summarizes the test performance of the S8x18.4 beams in terms of maximum load, failure mode, and the calculated AASHTO and AISC beam shear capacities using the minimum average web thickness taken between the beam end and the applied load. The minimum average web thickness method was also used for the other sets of beams. The strain behaviors of the beams are further discussed later. However, the point at which Specimens 1-S8-L and 2-S8-ML began to show concentrated bands of plastic strain behavior ranged from 50 to 55 kips, which is close to the calculated capacities according to AASHTO and AISC. In addition, Specimens 3-S8-MH and 4-S8-H began showing localized buckling failure between 15 and 20 kips.

Table 12. Maximum Load Relative to AASHTO and AISC Shear Capacities for S8x18.4 Beams

Specimen	Maximum Load (kips)	Failure Mode	AASHTO Capacity (kips)	Ratio of Maximum Load to AASHTO Capacity	AISC Capacity (kips)	Ratio of Maximum Load to AISC Capacity
1-S8-L	75.5	Web buckle	46.9	0.62	48.6	0.64
2-S8-ML	72.0	Web buckle	39.2	0.54	40.5	0.56
3-S8-MH	27.5	Web cracking	21.7	0.79	22.4	0.82
4-S8-H	23.3	Web cracking	21.7	0.93	22.4	0.96

W10x26 Beams: Tests 5-8

The data gathered in the second set of beam tests are displayed in Figure 29 and tabulated in Table 13 where they are compared with the calculated AASHTO and AISC beam shear capacities using the minimum average web thickness taken between the beam end and the applied load. As with Specimen 1-S8-L, the displacement data for Specimen 5-W10-L were collected from the DIC software for the load tests using the vertical displacement value of points near the bottom flange. This procedure was necessary because the data exported from the data logger became corrupt upon export.

The separation between the low- and medium-low-damage specimens and the two higher-damage beams was much greater than for the first beam set. Although the two high-damage W10x26 beams had holes like the S8x18.4 beams, the main distinguishing factor was the reduced web surface to resist cracking. After a crack propagated across the full length of the engaged shear area, the webs failed. Discussion of the strain fields later in the report discusses this behavior regarding Specimens 7-W10-MH and 8-W10-H.

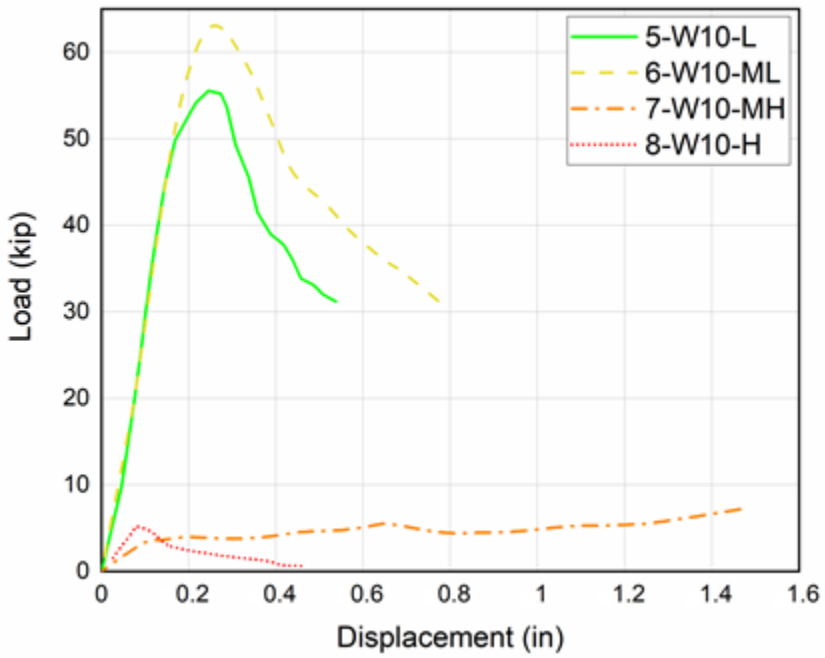

Figure 29. Load vs. Displacement Data for W10x26 Beams

Table 13. Maximum Load Relative to AASHTO and AISC Shear Capacities for W10x26 Beams

Specimen	Maximum Load (kips)	Failure Mode	AASHTO Capacity (kips)	Ratio of Maximum Load to AASHTO Capacity	AISC Capacity (kips)	Ratio of Maximum Load to AISC Capacity
5-W10-L	55.6	Web crippling	61.1	1.10	63.2	1.14
6-W10-ML	63.1	Web crippling	59.1	0.94	61.1	0.97
7-W10-MH	7.2	Web crippling	45.6	6.34	47.2	6.56
8-W10-H	5.2	Web crippling	46.2	8.92	47.8	9.23

W16x45 Beams: Tests 9-13

Test data for all W16x45 beams showed a similar load versus displacement relation before the beams reached maximum load and eventual beam failure. As expected, Specimen 13-W16-L(A) showed much more capacity than any other specimen since it did not have any web end corrosion because of being cut from the middle of a beam.

One discrepancy shown in Figure 30 was that the high-damage Specimen 12-W16-H had a higher capacity than even the original low-damage W16x45 beam, Specimen 9-W16-L. This occurrence prompted testing for Specimen 13-W16-L(A) after the realization that all previous specimens had beam-end web thinning. The larger capacity of Specimen 12-W16-H occurred because all the W16x45 beams failed at the bearing, so damage located directly above the support governed the beam's capacity. Specimens 9-W16-L, 10-W16-ML, and 11-W16-MH all showed typical beam end web corrosion with concentrated damage above the support; Specimen 12-W16-H instead displayed severe localized section losses continuing along the length of the beam. The absence of full-height web end damage in Specimen 12-W16-H was because, as with Specimen 13-W16-L(A), it was cut from the midsection of a beam. Because of the absence of any full-height web corrosion, Specimen 12-W16-H showed better performance than the other W16x45 beams since it did not have extensive damage outside the bearing area to initiate a local failure away from the support.

Table 14 compares the maximum experimental load and failure mode with the calculated AASHTO and AISC beam shear capacities using the minimum average web thickness taken between the beam end and the applied load.

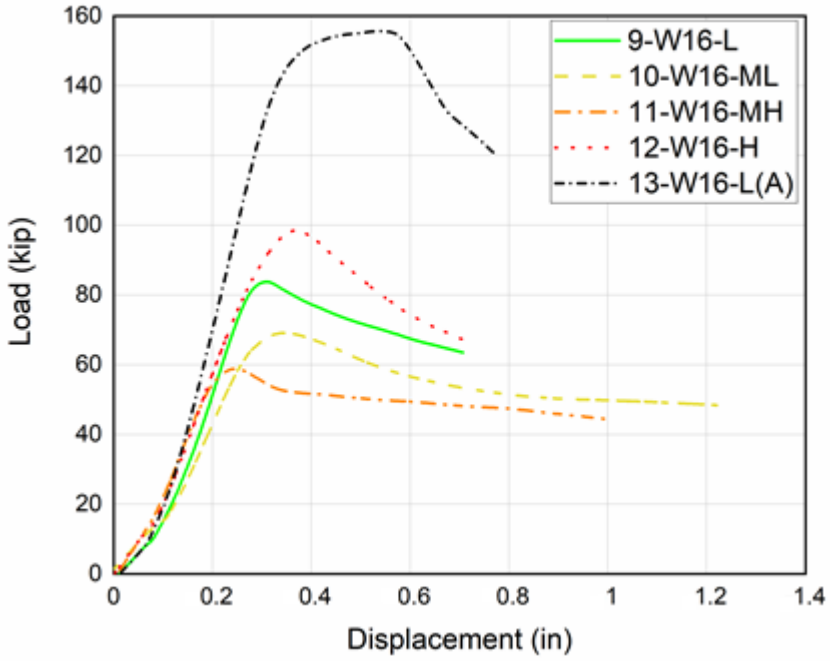

Figure 30. Load vs. Displacement Data for W16x45 Beams

Table 14. Maximum Load Relative to AASHTO and AISC Shear Capacities for W16x45 Beams

Specimen	Maximum Load (kips)	Failure Mode	AASHTO Capacity (kips)	Ratio of Maximum Load to AASHTO Capacity	AISC Capacity (kips)	Ratio of Maximum Load to AISC Capacity
9-W16-L	83.8	Web Crippling	57.2	0.68	60.1	0.72
10-W16-ML	69.2	Web Crippling	116.4	1.68	120.4	1.74
11-W16-MH	58.8	Web Crippling	39.2	0.67	46.6	0.79
12-W16-H	98.5	Web Crippling	129.7	1.32	134.2	1.36
13-W16-L(A)	155.7	Web Buckling	133.0	0.85	137.6	0.88

W21x62 Beams: Tests 14-17

The load versus displacement curves for the W21x62 beams once again followed a similar pre-failure linear relationship between load and displacement, seen in Figure 31. The maximum load, compared to the AASHTO and AISC beam shear capacities using the minimum average web thickness taken between the beam end and the applied load, is shown in Table 15.

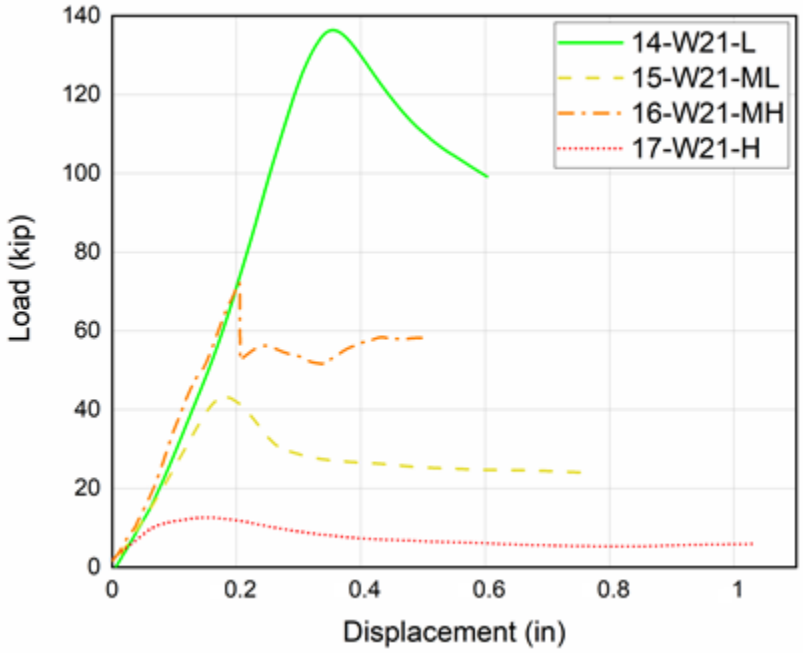

Figure 31. Load vs. Displacement Data for W21x62 Beams

Table 15. Maximum Load Relative to AASHTO and AISC Shear Capacities for W21x62 Beams

Specimen	Maximum Load (kips)	Failure Mode	AASHTO Capacity (kips)	Ratio of Maximum Load to AASHTO Capacity	AISC Capacity (kips)	Ratio of Maximum Load to AISC Capacity
14-W21-L	136.4	Web Crippling	182.9	1.34	189.2	1.39
15-W21-ML	43.1	Web Crippling	177.3	4.11	183.4	4.25
16-W21-MH	11.1[a]	Web Crippling	181.7	16.34	188.0	16.90
17-W21-H	12.6	Web Crippling	54.1	4.28	70.5	5.58

[a] Before crack formed.

One central discussion point is that the medium-high-damage Specimen 16-W21-MH showed a higher maximum load than the medium-low-damage Specimen 15-W21-ML. This discrepancy was due to the beam's failure mode, where holes in the lower web caused a quick crack formation before reaching 10 kips of applied load. Thus, most of the curve is post-failure behavior after the upper web began to rest on the bottom flange. As a result, the maximum load recorded by the DIC before failure for Specimen 16-W21-MH was 11.12 kips. In addition, Specimen 16-W21-MH had a significant amount of out-of-plane deflection, causing it to lean against the intermediate bracing. As a consequence, the applied load continued to rise past the point of failure because of the bracing resistance until the beam eventually began to slip, resulting in a maximum load of 72.17 kips, and the load drop represented by the vertical portion of the Specimen 6-W21-MH curve. This was the only exception to the inclusion of the absolute maximum load for the experimental values because it was the only test that was noticeably affected by a failure in the test configuration.

True Major Strain Fields

The following true major strain fields were created using DIC pictures captured during the large-scale shear load testing. In the initial configuration where every point was in its original position, the strain field appears blue, representing zero strain and zero material displacement. When concentrations of localized material displacements occur, the DIC software displays this as colors ranging from teal to red depending on the amount of maximum strain at each point in the strain field.

Each image presented shows the true major strains at a point during the loading process. Each particular point in time was chosen explicitly to illustrate the strain behavior when the initial web failure mode became identifiable. These modes included crack initiation and propagation, web buckling, and local web crippling below the load or above the support. Not all specimen strain fields were included because of behavior similar to other specimen tests or difficulty in identifying useful information for the report. Additional strain fields for all of the specimens excluded are provided in the Appendix.

Strain Fields for S8x18.4 Beams

The initial test of Specimen 1-S8-L clearly showed the development of stress bands, illustrated as red and yellow patterns in Figure 32. As the load increased to its maximum at 75.5 kips, these strains formed a diagonal web buckle perpendicular to the load path between the applied load and support's interior face. Simultaneously, the beam also displayed a typical shear failure mode where the top and bottom flanges buckled and the entire beam past the support began to displace downward.

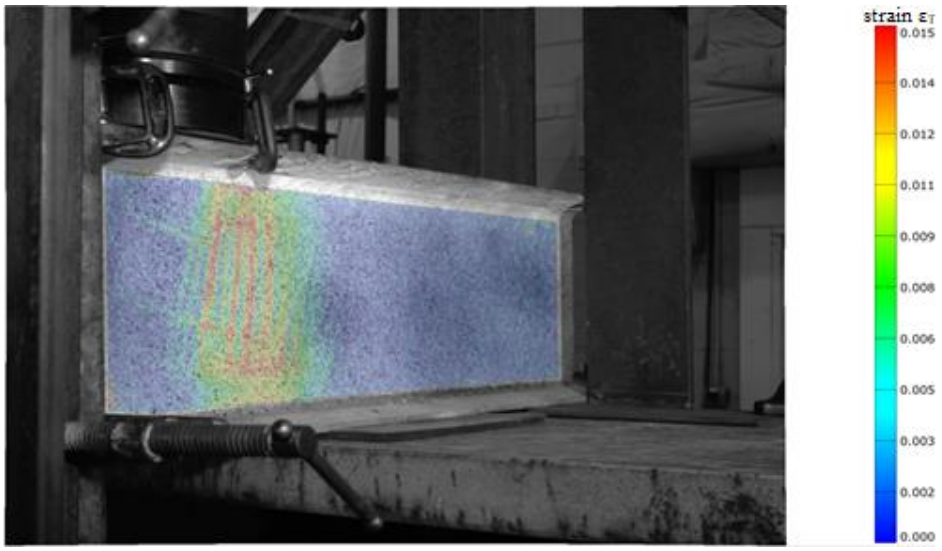

Figure 32. True Major Strain Field of Specimen 1-S8-L at 55 kips of Loading

Specimen 2-S8-ML displayed a diagonal web buckling failure similar to Specimen 1-S8-L, as shown in a more advanced state of deformation in Figure 33. A post-buckling image was chosen as the shear field's signs of initiation were less apparent because of the highly irregular web surface. Like Specimen 1-S8-L, the second beam displayed a combined web buckling and full height beam shearing behavior. This initial failure is represented on the load-displacement diagram (Figure 28, Specimen 2-S8-ML) as the transition past the maximum loading. In addition, the DIC software identified a high area of strain at the site of a localized web deformation at the top right corner of the strain field, which formed after the diagonal web buckling progressed.

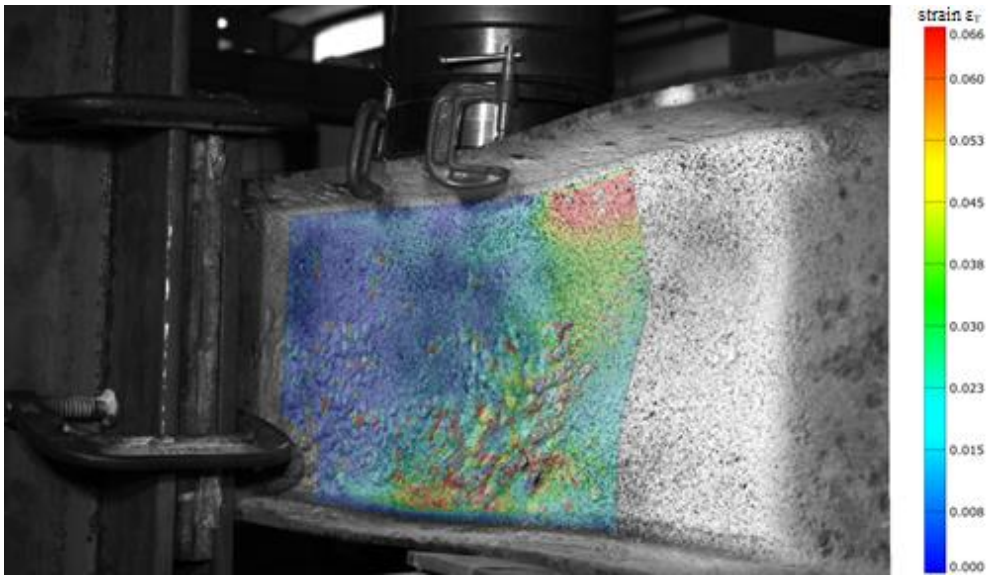

Figure 33. True Major Strain Field of Specimen 2-S8-ML at 0.7 in of Vertical Displacement After Failure

Specimen 3-S8-MH had a much more irregular surface profile than the first two beams, which resulted in a highly complex strain field, shown in Figure 34. However, this image also displays crack propagation among the three vertical holes above the edge of the support represented by the high strains connecting the openings (shown in a red circle in the figure). This crack eventually resulted in a full-height web separation along this high strain line combined with a diagonal buckling in a line connecting the longitudinal band of holes approximately 2 in from the bottom flange.

The final high-damage S8x18.4 beam (Specimen4-S8-H) showed a similar strain development between the through-web holes (see Figure A1 in the Appendix).

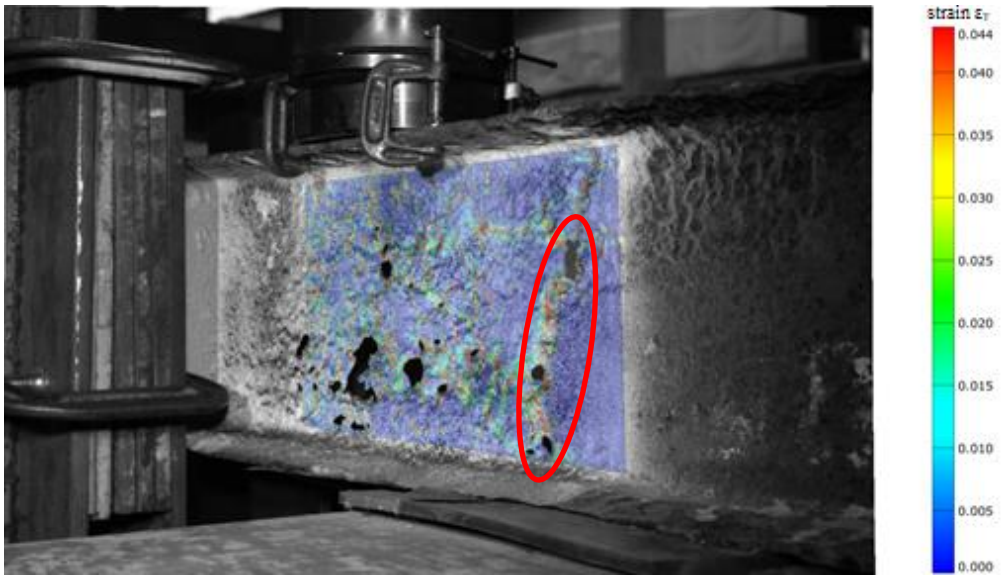

Figure 34. True Major Strain Field of Specimen 3-S8-MH at 20 kips of Loading Before Failure

Strain Fields for W10x26 Beams

Specimen 5-W10-L displayed a strain field comparable to Specimen 1-S8-L (see Figure A2 in the Appendix). However, a horizontal stress concentration below the load formed. This stress concentration developed further and caused a local buckling failure where the web under the top flange folded downward at the maximum load before a diagonal web buckle could form. This behavior was peculiar, as the surface profile indicated no section losses near the top flange. Instead, the web displayed only minor 1/16-in section losses for 2.5 in above the bottom flange on the west face (not shown). It was determined that this action was because the failure first initiated as a local displacement at the section loss above the lower flange on the west side of the web (into the image). Subsequently, a corresponding local failure initiated at the top of the east web displacing to the east (out of the image).

An event similar to what happened in Specimen 5-W10-L happened in Specimen 6-W10-ML. A horizontal high-strain band appeared below the applied load near the top flange in Figure 35, precipitating a local buckling failure of the web in this region. This failure was due to a region of 0.1-in-thick section loss in the lower portion of the west face of the beam, which again caused a pair of local out-of-plane displacements in the web.

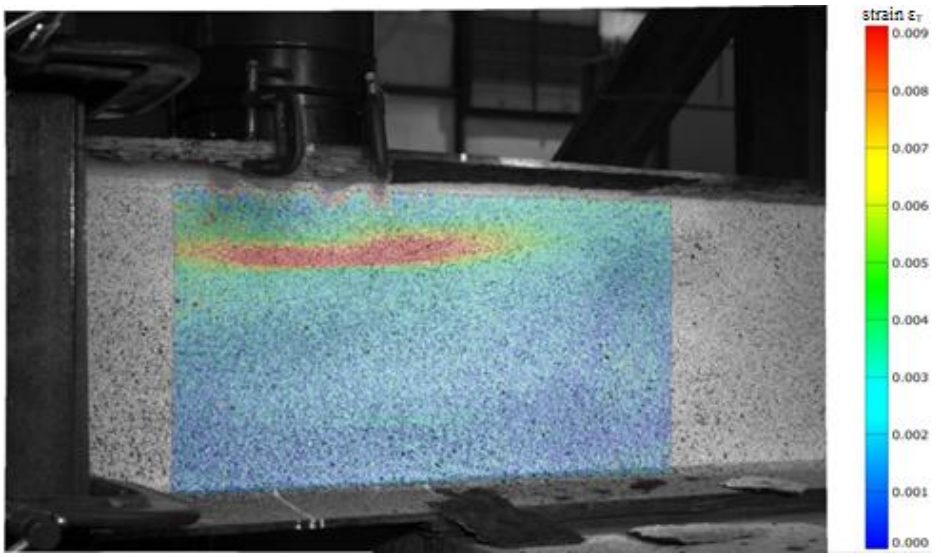

Figure 35. True Major Strain Field of Specimen 6-W10-ML at 49.9 kips of Loading Before Failure

For Specimen 7-W10-MH, the failure was initiated among six holes at the bottom of the web near the support (see Figure A3 in the Appendix) and extended to the end of the beam. As with Specimens 3-S8-MH and 4-S8-H, multiple web openings created a line of high strain between them. This behavior was exacerbated by the beam end being much closer to the support, which reduced the available material to confine the crack. In addition, the reduced support length from using the welded plate resulted in higher stress concentrations above the short bearing area, which ultimately caused a web crippling failure, folding the lower web before the steel could separate.

The behavior of Specimen 8-W10-H was similar to that of Specimen 7-W10-MH, as the hole in the area between the load and support initiated failure, shown in Figure 36 as a thin red line extending from a pinhole in the web, which is marked with a red oval.

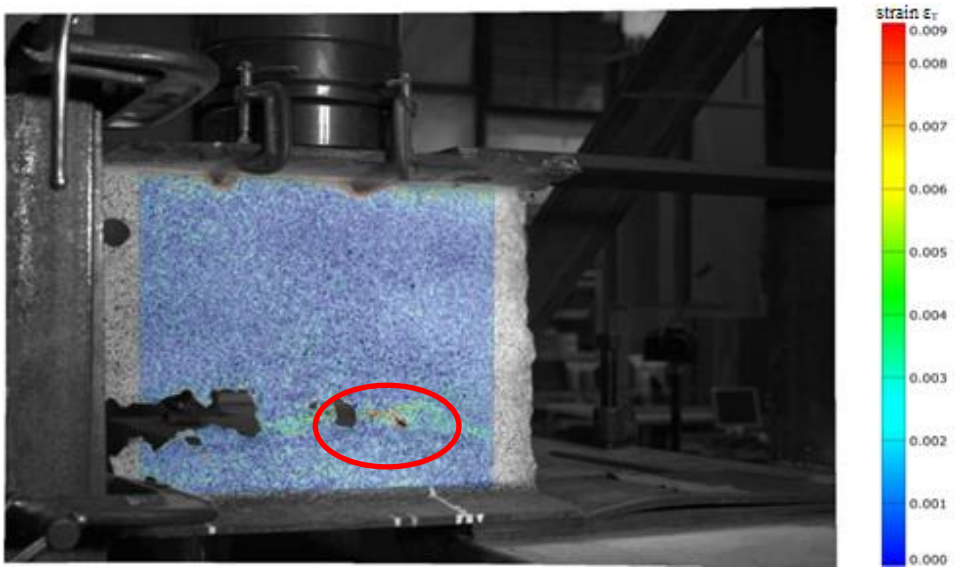

Figure 36. True Major Strain Field of Specimen 8-W10-H at 5 kips of Loading Before Maximum Loading

Instead of traveling toward the beam end, this high-strain line propagated to the 1-in hole directly beneath the load and quickly jumped to the large 3.4-in opening to the left. These stress concentrations quickly resulted in local web folding on either side of the 1-in hole beneath the load. This behavior was categorized as a web crippling failure as with Specimen 7-W10-MH, where web folding because of concentrated loads above the bearing was augmented by the path of stress concentrations caused by the web holes.

Strain Fields for W16x45 Beams

The failure of Specimen 9-W16-L occurred as a local web buckle extending to the beam end, similar to how the crack developed in Specimen 7-W10-MH. In this case, there was no separation of the beam, but the material strain increased along the red line in Figure 37 until failure occurred. The assumption was that the bearing strength would control in this configuration because of the extensive damage present above the support. Although no damage continued past the face of the bearing pad (marked as a faint white line in the bottom right of Figure 37), the corrosion still caused a change in failure mode from the regular diagonal web buckling, as shown in Specimen 13-W16-L(A).

The strain field of Specimen 10-W16-ML, shown in Figure 38, clearly shows the development of a horizontal line of high-strain concentration in the lower web directly above the support. This line of high strain eventually developed into a local crippling failure just past the face of the support where the beam deflected vertically downward.

Specimen 11-W16-MH developed a failure mode nearly identical to Specimen 9-W16-L (see Figure A4 in the Appendix). This failure was due to the extensive section losses near the bottom flange, primarily above the support. Despite the applied load being placed so far from the support, failure resembled a bearing failure rather than some form of local buckling at the support's face.

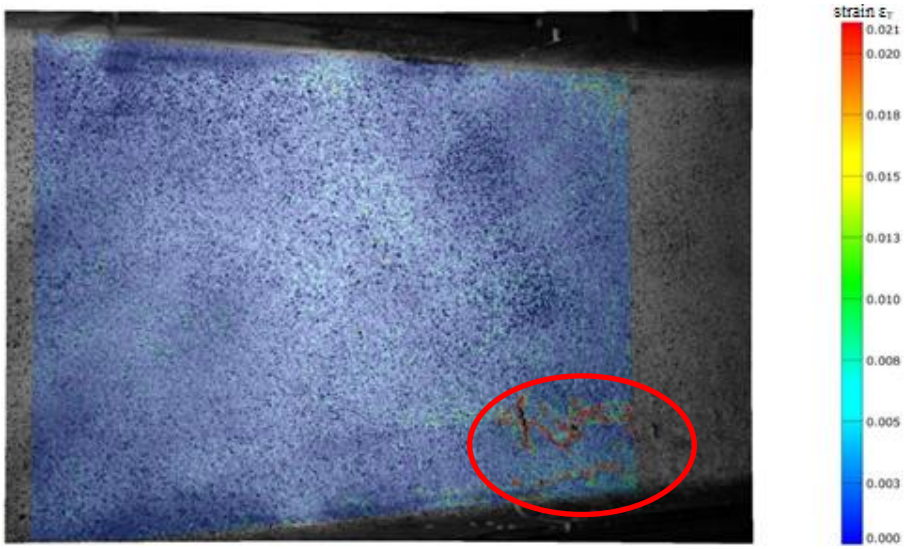

Figure 37. True Major Strain Field of Specimen 9-W16-L at 77 kips of Loading Before Failure

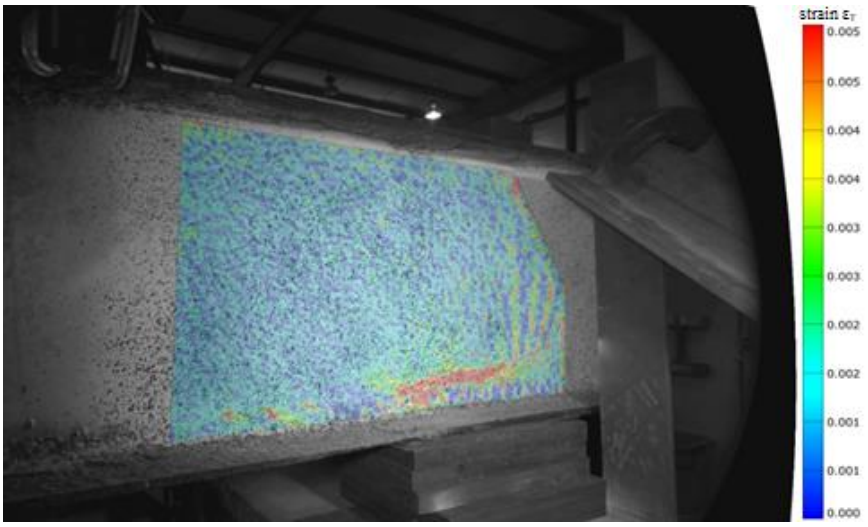

Figure 38. True Major Strain Field of Specimen 10-W16-ML at 67 kips of Loading Before Failure

Specimen 12-W16-H exhibited two main areas of strain concentrations below the applied load and above the support (see Figure A5 in the Appendix). As with Specimen 9-W16-L, local web crippling above the support was the governing failure mode. This observation is interesting because most other beam tests favored failure either at the support or below the applied load. This specimen was the only one that simultaneously displayed signs of both failure modes.

The failure mode in Specimen 13-W16-L(A) was what was expected to occur in Specimen 9-W16-L, thus validating its addition to the testing matrix. Figure 39 shows multiple vertical and horizontal stress bands forming on the web's surface, as well as a large area of high stress below the applied load (located by the red oval in the figure). This stress pattern led to a combined local deflection below the loading point and diagonal web buckle from the lower left to the top right of the figure.

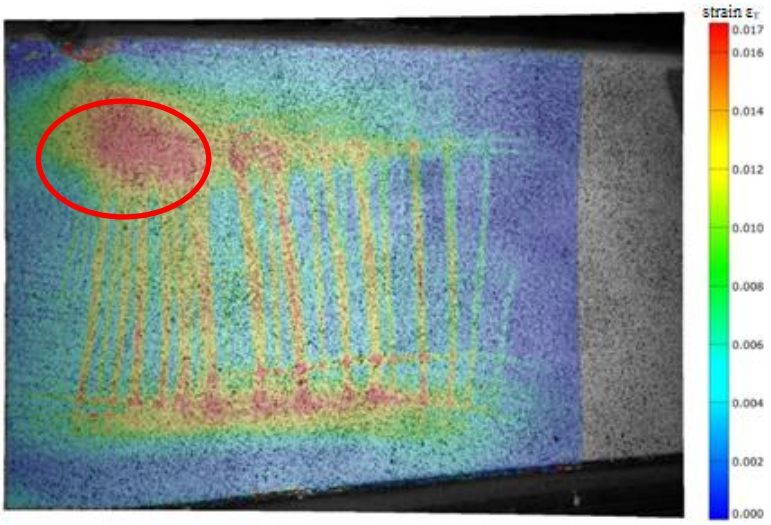

Figure 39. True Major Strain Field of Specimen 13-W16-L(A) at 145 kips of Loading Before Failure

Strain Fields for W21x62 Beams

The failure pattern of Specimen 14-W21-L occurred as a local buckling beneath the top flange at the loading point. Figure 40 shows the stress field condition directly before the maximum load was reached. This failure mode was like that of Specimen 6-W10-ML, which would suggest that the failure was due to section loss near either the top flange or the bottom flange below the load, causing the web to deform near the top and bottom flanges. This observation could not be verified using the DIC because the system's range did not extend all the way to the location of the applied load. For this reason, most of the W21x62 beams' strain field images are included in the Appendix. Visual inspection of the beam showed minor section losses.

The strains in Specimen 15-W21-ML were all below 0.003, which makes them well below any other values shown so far. Despite placement of the applied load so far from the bearing area, the damaged web section above the support controlled the beam's failure mode. As with Specimen 9-W16-L, the assumption was that the bearing strength would govern for this beam; however, the 21 in of web between the applied load and the support did not develop any strain concentrations through testing to failure of Specimen 15-W21-ML since the deformations were focused at the bearing.

The failure of Specimen 16-W21-MH was due to the presence of a line of through-web holes above the bottom flange. As with Specimen 8-W10-H, the failure mode was a line of buckling between the lower web holes, which extended to the beam end. The strain condition captured by the DIC camera showed minimal variation, as with Specimen 15-W21-ML, and the buckled regions between the holes deflected out of the view of the camera.

The failure in Specimen 17-W21-H also occurred outside the camera's view in the section loss below the top flange. The web developed a local out-of-plane buckle below the applied load, which was typical for several beam failures preceding this one, including Specimens 5-W10-L, 6-W10-ML, 13-W16-L(A), and 14-W21-L. It appears that defects in the area directly below the applied load significantly contributed to the beam's failure behavior.

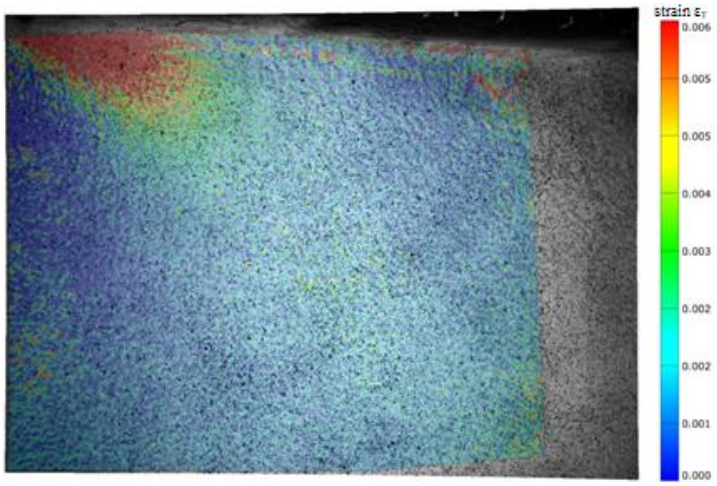

Figure 40. True Major Strain Field of Specimen 14-W21-L at 133 kips of Loading Before Failure

Task 3: Comparison of Simplified Analysis Methods

Comparison of Five Thickness Measurement Results

As mentioned previously, five web thickness measurements were collected from each beam. Figure 41 presents a prediction error plot comparing the maximum experimental shear load vs. the AASHTO shear capacity using the five different methods for web thickness measurement. In the figure, points lying below the 45-degree line (not to be confused with the 45-degree average) indicated that the method overestimated the capacity and those lying above the line indicated that the method conservatively underestimated the experimental capacity. Although conservative, a data point falling considerably above the line is not necessarily beneficial because it means that a beam's capacity was underestimated by a significant amount, leading to unnecessary repairs if this method were applied to a bridge inventory. Therefore, in an ideal case, all of the data points would fall on or slightly above the 45-degree line.

Immediately it can be seen on the right side of Figure 41 that the minimum cross-section, 45-degree, and area average methods provide similar and unconservative results for at least 5 of the 17 tests. The lower area averages (4-in and 3-in) provided results that better correlate with the experimental values as shown by their proximity to the 45-degree line. As expected, it was found that the lower area averages were the most conservative estimates of remaining web thickness. However, to illustrate the effect of not properly defining a measurement method, all methods considered that did not specifically define a web thickness measurement method were calculated using the minimum cross-section thickness value. This was done since it was the simplest of the five methods. Ideally, a single measurement value such as those presented in some inspection reports could be used, but this was outside the scope of this study to attempt to standardize the use of calipers, pit depth gauges, or any other physical collection method that would vary depending on the experience and intuition of a bridge inspector.

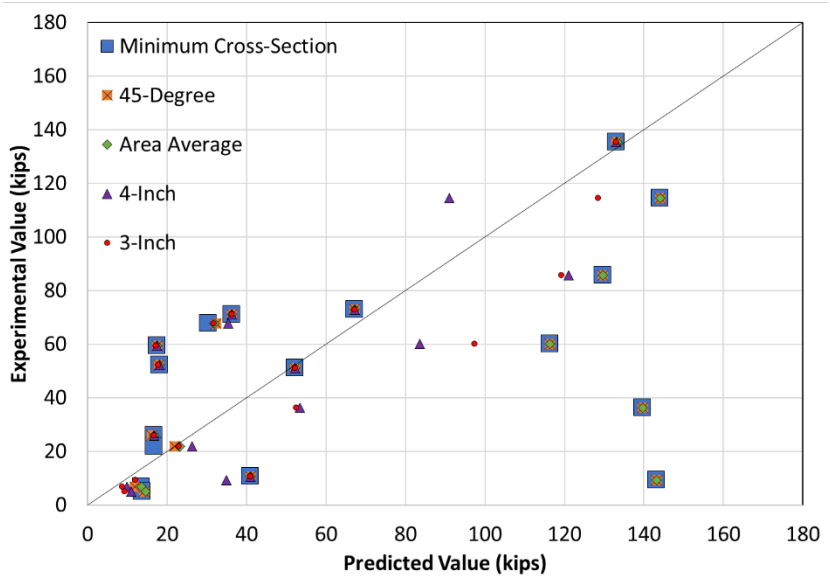

Figure 41. Prediction Error Plot of Maximum Experimental Shear Load vs. AASHTO Shear Capacity Using Five Thickness Measurement Methods

Comparison of Test Data to the Literature

Several shear capacity calculations were compared to the full-scale test results to determine which methods would be appropriate for VDOT to use in bridge load rating. The results of capacity calculation methods presented previously were compared to determine their correlation with the outcome of the full-scale testing. Each calculation was completed using the web thickness measurement data presented in Figures 24 through 27. The process for creating the thickness matrices used in this process was described previously. Although this computer measurement process is highly comprehensive, the implementation of these capacity calculation methods requires a method for gathering thickness data in the field without using a DIC system. Such methods could include the use of an ultrasonic thickness gauge or a set of calipers.

The AASHTO and AISC equations were used as baseline shear calculation methods that used the five effective web thickness measurements. In addition to these two shear capacity calculation methods, six additional capacity calculation methods were selected to determine their correlation with the test results using the same thickness measurements mentioned previously. The Sugimoto et al., van de Lindt and Ahlborn, and Rahgozar methods calculate a strength reduction ratio or percentage expressing a beam's remaining strength, which relies on the accurate calculation of the undamaged shear capacity using AASHTO, AISC, or an equivalent standardized shear calculation method. The Darwin and Donahey, MassDOT, and Tzortzinis et al. methods calculate the capacity directly and incorporate web opening measurements if present. If holes were present in the beam webs, their lengths and heights were measured. Although the holes were irregularly shaped, the length and height measurements were conservatively assumed to be the smallest rectangular section fully encompassing the opening. In some of these cases, multiple holes closely spaced in groups were conservatively treated as a single large hole encompassing all the present openings.

Table 16 presents the maximum applied shear loads for each specimen and the shear capacities calculated using the seven estimation methods. The maximum applied shear load was calculated using the maximum applied load with an assumed simply supported 14-ft span length. The calculated strength reduction ratios for the Sugimoto et al., van de Lindt and Ahlborn, and Rahgozar methods were applied to the AASHTO undamaged beam capacities. The AASHTO, AISC, van de Lindt and Ahlborn, and Rahgozar methods leave the beam thickness value to be determined by the load rater. The minimum average web thickness taken from the DIC scans was used in these cases because of being a commonly used thickness measurement method before this study. The Sugimoto et al. method used the 45-degree average thickness measurement as specified in Sugimoto et al. Although the Darwin and Donahey method does not consider section loss outside web openings and assumes that the web is undamaged, the Tzortzinis et al. study used the 4-in average web thickness. Blank cells in the table signify that the calculation method could not be used for the associated beam. The van de Lindt and Ahlborn method applies to beams with more than 35% of the web height affected by corrosion, which did not allow it to be used on many of the higher-damaged beams in this study. The Darwin and Donahey method was applicable only to calculate the effect of web openings, which ruled out beams displaying only section losses without holes.

Table 16. Maximum Applied Shear Load Versus Calculated Shear Capacities (kips)

Specimen	Max. Applied Shear Load (kips)	AASHTO (kips)	AISC (kips)	Sugimoto et al. (kips)	van de Lindt and Ahlborn (kips)	Rahgozar (kips)	Darwin and Donahey (kips)	Tzortzinis et al. (kips)	MassDOT (kips)
1-S8-L	71.0	36.3	37.6	36.5	36.5	36.6		43.8	152.4
2-S8-ML	67.7	35.2	36.5	32.4		35.2		30.2	117.4
3-S8-MH	25.8	16.8	17.4	16.1		26.0	46.7	18.0	39.0
4-S8-H	21.9	26.3	27.2	21.8		29.7	57.2	17.3	48.6
5-W10-L	52.3	51.3	53.1	51.3	52.8	51.3		42.2	32.5
6-W10-ML	59.3	49.4	51.1	50.5	46.2	49.4		37.3	30.3
7-W10-MH	6.8	22.8	23.9	34.2	38.2	23.9		15.2	7.9
8-W10-H	4.9	43.2	44.7	40.4		43.2	41.5	7.2	2.4
9-W16-L	72.8	58.6	67.8	128.9		91.9		53.5	41.4
10-W16-ML	60.1	60.8	69.5	145.9	157.1	90.1		52.7	53.2
11-W16-MH	51.1	39.6	52.2	155.1	154.6	78.2		57.8	37.2
12-W16-H	85.6	148.0	153.1	164.7	149.5	148.0		67.6	118.7
13-W16-L(A)	135.3	165.7	171.5	165.7	169.9	165.7		75.0	127.4
14-W21-L	114.5	107.6	118.9	237.7	222.3	149.3		89.4	47.4
15-W21-ML	36.2	39.0	60.5	221.4	197.9	106.5		55.0	32.4
16-W21-MH	9.3	16.5	34.1	212.7	144.1	80.0	259.8	4.4	5.3
17-W21-H	10.6	55.3	76.4	208.3	171.0	124.0		29.6	14.5

These data are displayed in Figure 42 as a prediction error graph plot as in Figure 41 where points above the line are conservative and points below the line are unconservative.

Considering only the AASHTO and AISC capacity calculations, more than one-half of their results overestimated the experimental capacity. This shared unconservative behavior was due to how similar their equations are structured. The Sugimoto et al., van de Lindt and Ahlborn, and Rahgozar methods each applied a reduction ratio or percentage to the undamaged AASHTO or AISC capacity but typically greatly overestimated the experimental values. This overestimation was especially egregious in the cases of high amounts of corrosion, since these methods were not designed for such high section losses. The Darwin and Donahey method applied to only a select few beams but for the most part showed little correlation with the experimental values, and not enough to suspect that it was a good method for the evaluation of corroded beam ends. The Tzortzinis et al. and MassDOT points remained in relatively close groups for all 17 tests. In addition, the Tzortzinis et al. method tended to provide more conservative results than the MassDOT method, typically lying above the line.

Figure 43 focuses on the prediction errors for only the AASHTO and Tzortzinis et al. methods. This is because VDOT currently uses BrR (which uses AASHTO) to evaluate corroded beam shear capacity and the results of the Tzortzinis et al. method showed the best correlation with the maximum experimental shear loads and were typically conservative. In both cases, the 3-in web height was used to determine the web thickness. In the case of the AASHTO results, use of the average web thickness taken from the 3-in web height resulted in less scatter than the minimum web thickness, as initially shown in Figure 41. However, six of the values were still below the 45-degree line, meaning that they overestimated the experimental capacity. As for the Tzortzinis et al. results, the values tended to fall above the 45-degree line, signifying a more conservative method, with varying results for high-damage beams.

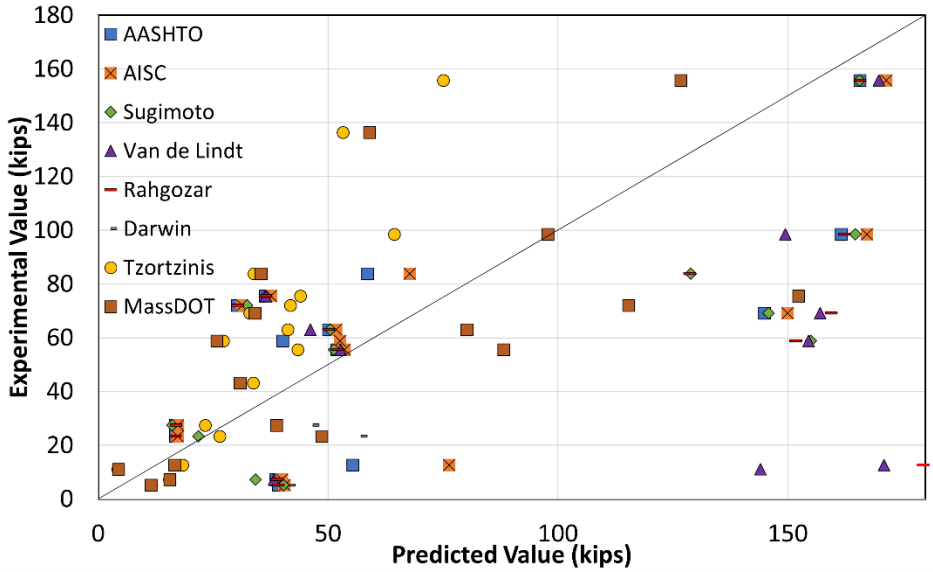

Figure 42. Prediction Error Plot for All Tested Calculation Methods

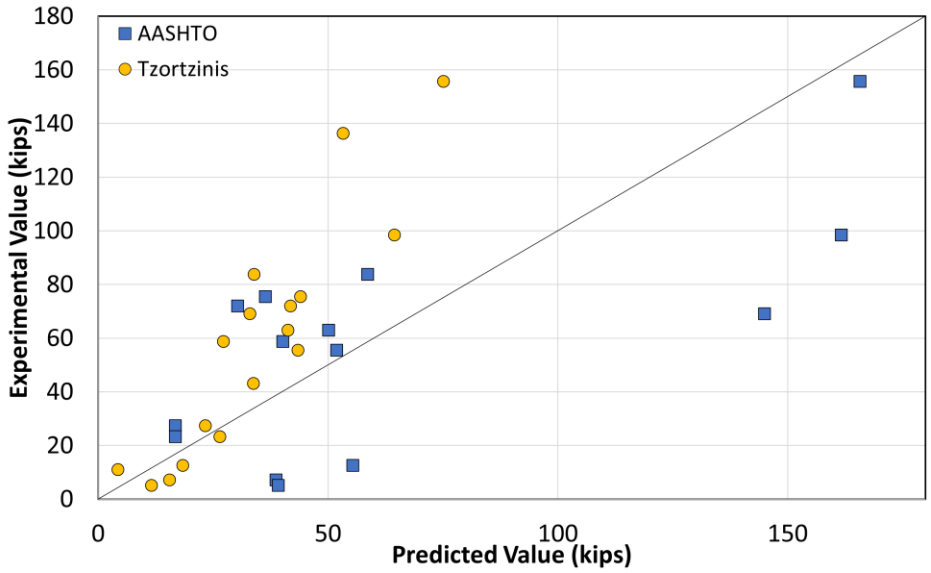

Figure 43. Prediction Error Plot for AASHTO and Tzortzinis et al. Capacity Calculations Using Remaining Average Thickness Over Corroded Web Portion

Several reasons may explain why the Tzortzinis et al. equations performed better than the others. The Tzortzinis et al. method considers the effect of web hole size during the web thickness calculation rather than ignoring the holes or simply including the holes in an average web thickness. The consideration of through-web damage is an important feature of a suitable capacity calculation method because of the stress concentrations at holes. As shown previously, web holes were typically the sites of localized web failures that governed the capacity of beams that would have otherwise continued to resist shear loads.

Only 5 of the 17 test specimens had through-web holes: Specimens 3-S8-MH, 4-S8-H, 8-W10-H, 16-W21-MH, and 17-W21-H. Some of these beams had extensive corrosion holes spread across the length and full height of the web, such as Specimens 3-S8-MH and 4-S8-H. In these cases, an equivalent web opening encompassing a group of holes within the lower 3 in of the beam was selected to represent a single through-web hole. The alternative case was an equivalent hole encompassing all the web holes across the length and height of the web, resulting in a near 100% section loss, which understandably resulted in near total loss of shear capacity. In other cases, some beam webs showed single major web holes in addition to several surrounding pinholes, which were ignored. For Specimen 8-W10-H, for example, the single extensive longitudinal web hole alone was used in the Tzortzinis et al. equation to calculate the reduced web thickness. Although the calculated shear capacities using these assumptions were imperfect, each sufficiently underestimated the true shear strength. Based on these observations, when multiple holes exist in the lower 3 in of the web, an equivalent larger web opening encompassing all of the surrounding holes can be conservatively used when determining the hole dimension inputs for the Tzortzinis et al. equation.

Another significant difference from the other methods is that the Tzortzinis et al. method calculates the reduced beam capacity directly instead of applying a reduced ratio to the undamaged beam strength. Although the yield capacity equation is similar to those of AASHTO and AISC, the web-crippling equation governed for every beam. For web crippling, the

Tzortzinis et al. equation uses a much different approach with statistically derived coefficients and is based on the original MassDOT equations. The comparison between the Tzortzinis et al. and MassDOT calculated capacities is shown in Figure 44. The prediction error plot shows that the modifications made to the crippling equation significantly improved the reliability of the results, as many of the MassDOT calculations considerably overestimated the test results.

One discrepancy with the Tzortzinis et al. method is that the corroded web resistance is calculated as the minimum of the nominal yielding and web local crippling capacities. In the 2019 study, Tzortzinis et al. (2019b) recognized that the method does not include a capacity equation that considers the effect of web buckling. During the current study, however, web cracking, crippling, and buckling behavior occurred during the large-scale testing process. Yet most tests failed because of web crippling. Typically, web buckling occurred on beams with low amounts of damage, or less than 1/16 in of total section loss, or on those with web thinning at mid-height. It would be acceptable to continue using the AASHTO shear calculation methods with slightly adjusted thickness percentages in cases where there is less than 1/16 in of section loss.

The critical area most appropriate for this study was found to be 3 in above the bottom flange extending for the full support length (N) plus one beam height from the interior support (h) (Figure 45). Although the 4-in section defined in the MassDOT *LRFD Bridge Manual* also gave much better results than any of the other web thickness measurements, lower web damage tended to be within the bottom 3 in of all of the beams tested in the present study. In addition, web holes within one beam height of the support also tended to affect appreciably the shear capacity to the point of causing low-load failures in some specimens, such as Specimen 8-W10-H. The length of holes (H) was found to influence the failure loads.

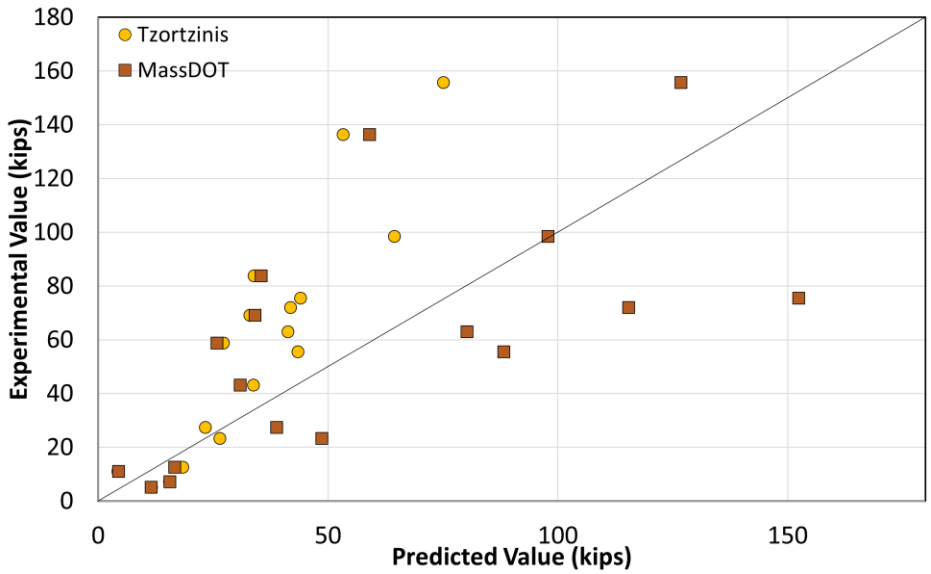

Figure 44. Prediction Error Plot for MassDOT and Tzortzinis et al. Capacity Calculation Methods

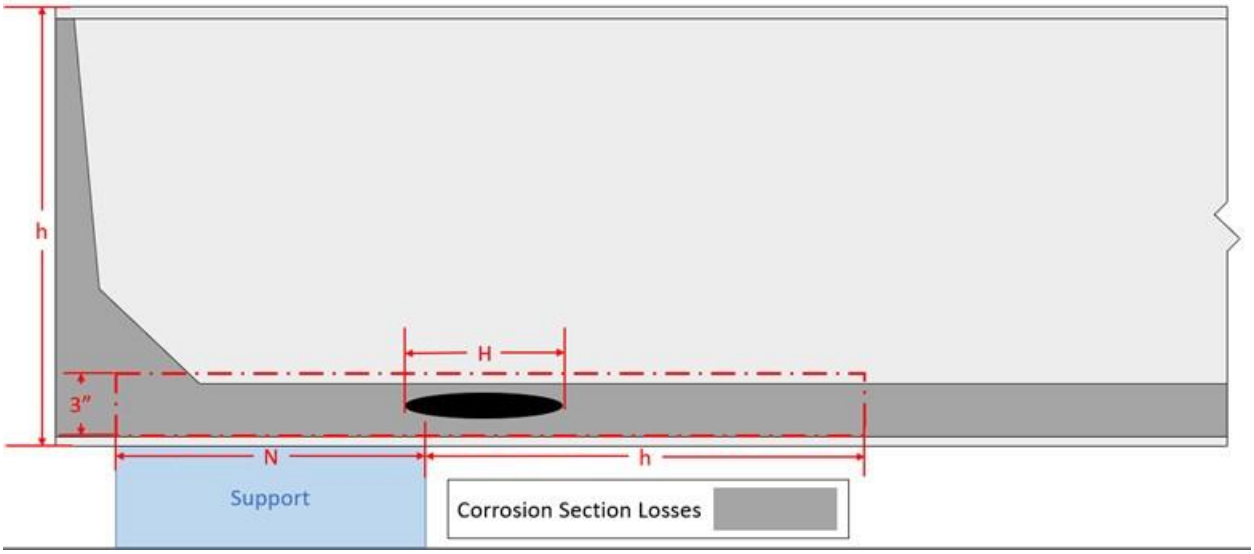

Figure 45. Critical Dimensions Used for Load Rating Corroded Steel Beams

Task 4: Incorporation of Simplified Analysis Into BrR

The beam capacities calculated using the BrR deterioration profile were compared to the experimental capacities to determine the best strategy for assessing corrosion section loss for load rating engineers. The results of this comparison are shown in Figure 46. This figure is similar to Figures 41 through 44. Each beam's experimental capacity is plotted on the y-axis. Another capacity, BrR in this case, is plotted on the x-axis, with a 45-degree line included in the figure to illustrate where the data points should fall if the experimental capacity is equal to the BrR capacity for each beam. In this figure, the data points are differentiated by the level of damage to determine if the level of damage influenced the correlation between the BrR and experimental capacity.

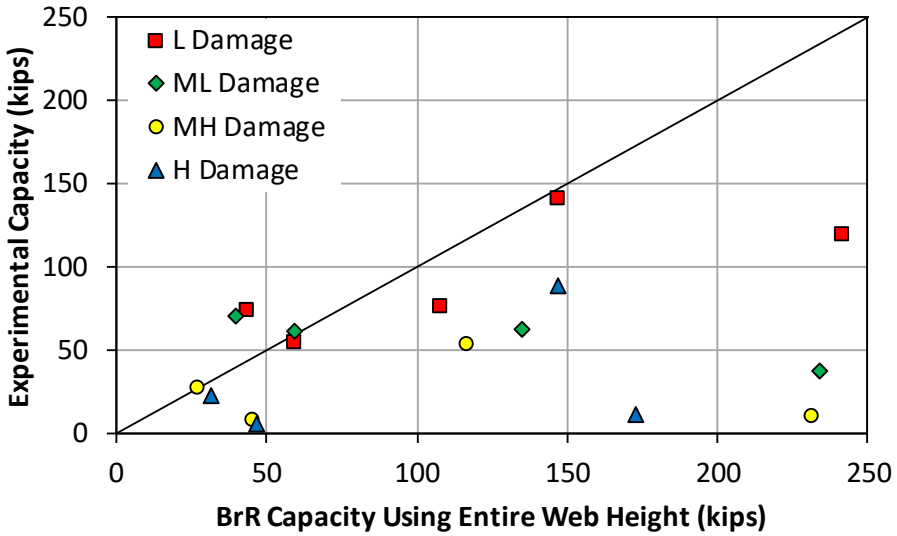

Figure 46. Comparison of Experimental and BrR Capacity. L = low; ML = medium-low; MH = medium-high; H = high.

As shown in the figure, some of the data points fell slightly above the 45-degree line, but many data points fell significantly below it. This indicated that merely modeling the corrosion of the beams assuming that the thickness loss is an average over the entire height of the beam web in the BrR deterioration profile can lead to overestimating the capacity of deteriorated beams. Since the BrR capacities did not provide good agreement with the experimental capacities, different methods of calculating the remaining average web thickness and subsequent web thickness losses were included in the deterioration profile to determine modified beam capacities in BrR.

Similar to the comparison of simplified analysis methods, multiple methods of calculating the remaining average web thickness were evaluated with BrR. The first method used was the minimum average method (shown in Figure 21). Once the minimum average web thickness was determined, it was compared to the nominal web thickness to calculate a percent web thickness loss, and that value was input into the BrR deterioration profile. Results from this comparison are shown in Figure 47.

In examining Figure 47, it was clear that more data points either fell above or were closer to the line when compared to Figure 46. This result indicated that using the minimum average method to calculate the remaining average web thickness to calculate a deteriorated beam's capacity in BrR leads to a better correlation with the experimental capacity. However, many of the data points still fell well below the line, suggesting that other methods of calculating the average web thickness needed to be considered.

The method of calculating the remaining average web thickness investigated was the bottom 4-in of the web method. The remaining average web thickness was calculated using the thickness matrices. For beams with holes in the web attributable to corrosion, the thickness of the web at the location of the holes was equal to zero in the thickness matrices. These 0-in thickness values were not included in the calculations to determine the average web thickness.

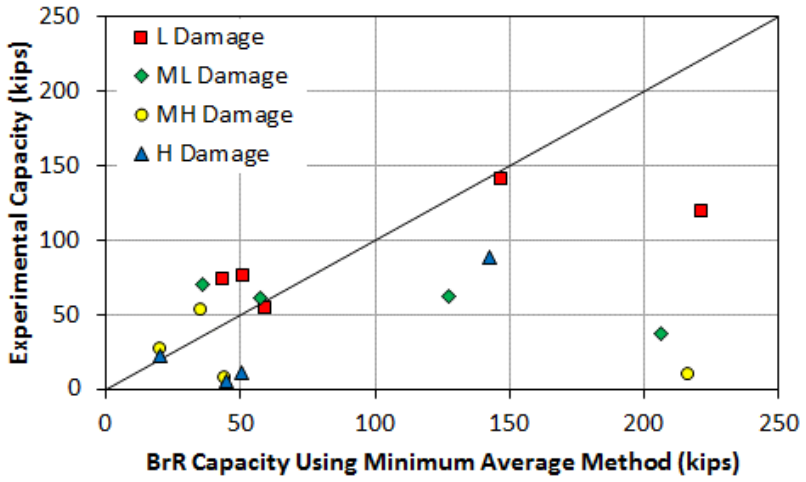

Figure 47. Comparison of Experimental and BrR Capacity Using the Minimum Average Method. L = low; ML = medium-low; MH = medium-high; H = high.

This was done so that if this method were to be implemented, a bridge inspector would need to obtain measurements of the web thickness only in areas where the web still existed (i.e., had a thickness greater than 0). Otherwise, the inspector would need to record 0-in web thickness measurements where holes were located, which seemed slightly more complicated. This method was also consistent with how Tzortzinis et al. calculated average web thickness measurements (Tzortzinis et al., 2019b). The remaining average web thickness was then used to calculate a percentage thickness loss, and that value was entered into the BrR deterioration profile in 0.5-ft horizontal increments. Beam capacities were then calculated using BrR. Results from using the bottom 4-in method are shown in Figure 48.

The results shown in Figure 48 demonstrated a much better correlation using the bottom 4-in method rather than either the entire beam area (shown in Figure 46) or the minimum average method (shown in Figure 47). Most of the data points were much closer to the line in this figure; a handful of the data points fell above the line. However, the majority of the data points fell below the line, so this method is still unconservative. Therefore, the bottom 3-in web method was used to determine the average remaining web thickness for estimating the capacity of each beam in BrR using the same method as the bottom 4 in except with the 1-in reduction in web height. The bottom 3-in method was also consistent with where most of the corrosion damage was located on the beams in this study. Results from using the bottom 3-in method are shown in Figure 49.

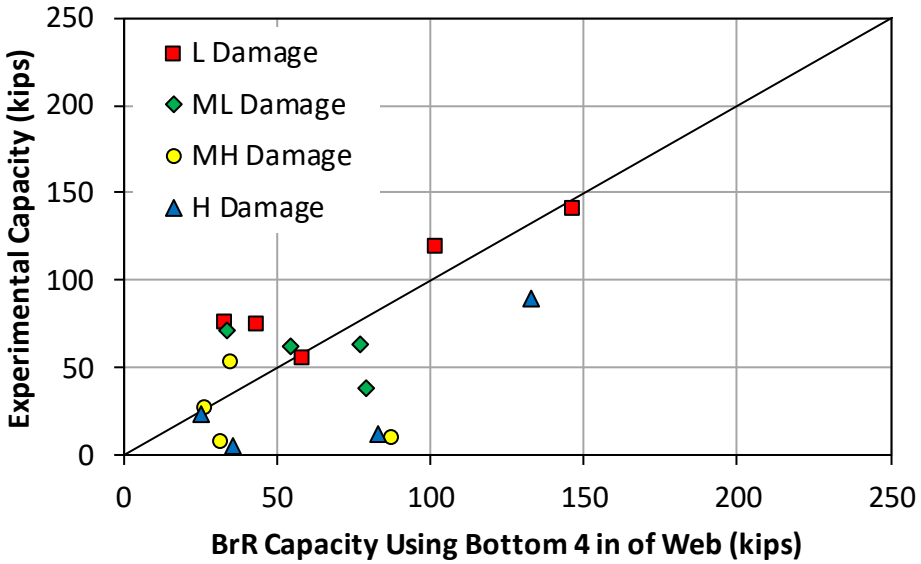

Figure 48. Comparison of Experimental and BrR Capacity Using Bottom 4 in of Web. L = low; ML = medium-low; MH = medium-low; H = high.

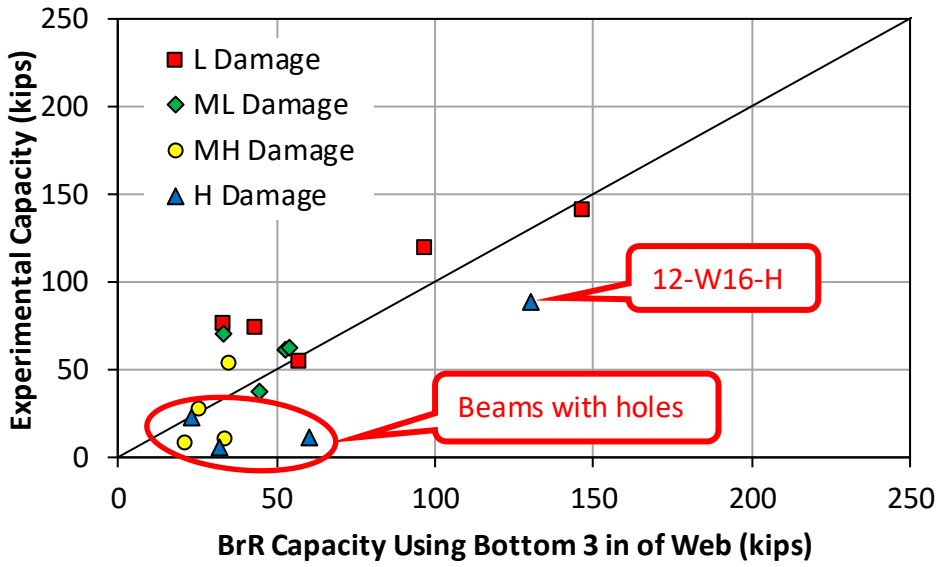

Figure 49. Comparison of Experimental and BrR Capacity Using Bottom 3 in of Web. L = low; ML = medium-low; MH = medium-high; H = high.

The data points in the bottom 3-in web method in Figure 49 provided an even better correlation than the bottom 4-in web method. More data points were above the line, and even those that were not were much closer to it when compared with Figure 48, especially those data points representing beams with BrR capacities under approximately 60 kips. The figure also displays better performance for beams in each of the four damage levels, though the medium-high and high-damage beams showed the worst correlation. Smaller web heights were considered, such as the bottom 2 in of the web, but they did not seem reasonable since many of the beams had damage extending past the bottom 2 in of the web.

The beams that had the worst correlation were beams that had holes in the web and Specimen 12-W16-H, both of which are indicated in the figure. Though Specimen W12-W16-H did not have holes, it was considered a high-damage beam because of significant amounts of corrosion throughout the beam web, not just concentrated at the bottom of the web. Since some of the beams with holes did not have good correlation, these beams were further analyzed by consideration of an additional modification to the remaining average web thickness.

As discussed previously, the MassDOT load rating procedure has a modification for reducing the effective web thickness to account for holes on steel beam ends without bearing stiffeners (MassDOT, 2020). The MassDOT modification for holes is shown in Equation 9 and depends on the remaining web thickness, bearing length, length of the hole, and the k-region length for the beam. Because this method is currently used by MassDOT, it was applied to the beams with holes in this study to evaluate its effectiveness.

Because the beams in this study did not include an overhang past the bearing, the "*5k*" terms in Equation 9 were replaced with "*2.5k*" as discussed previously. The remaining average web thickness calculated using the 3-in web method was used as the remaining web thickness term in the equation based on its effectiveness, demonstrated previously. The effective web thickness for the six beams containing holes was then calculated using Equation 9.

Table 17 shows the parameters used in the equation, including the calculated effective web thickness accounting for holes for each beam in the last column of the table. As discussed previously, Specimens 4-S8-H, 7-W10-MH, and 8-W10-H contained multiple holes in close proximity. These holes were conservatively considered as a single large hole encompassing all the nearby holes. The hole length term, *H*, in Equation 9 was then set equal to the length of this large hole encompassing nearby holes.

The effective web thickness accounting for holes (last column in Table 17) was compared to the nominal web thickness of each beam to determine the percent thickness loss. This percent thickness loss was then input into the BrR deterioration profile for each beam, and a shear capacity was calculated. Results from this analysis are shown in Figure 50, which is similar to Figures 46 through 49.

Table 17. Parameters for MassDOT Effective Web Thickness Reduction for Specimens With Holes

Specimen With Hole(s)	Effective Web Thickness in Bottom 3 in of Web, t_w in Equation 9 (in)	Bearing Length, N in Equation 9 (in)	Beam Fillet Size, k in Equation 9 (in)	Hole Length, H in Equation 9 (in)	Effective Web Thickness Accounting for Holes, t_{ave} in Equation 9 (in)
3-S8-MH	0.159	12	1.00	1.549	0.142
4-S8-H	0.145	12	1.00	1.973	0.125
7-W10-MH	0.114	12	0.74	3.362	0.087
8-W10-H	0.140	12	0.74	7.222	0.067
16-W21-MH	0.171	12	1.12	10.028	0.055
17-W21-H	0.206	12	1.12	6.375	0.117

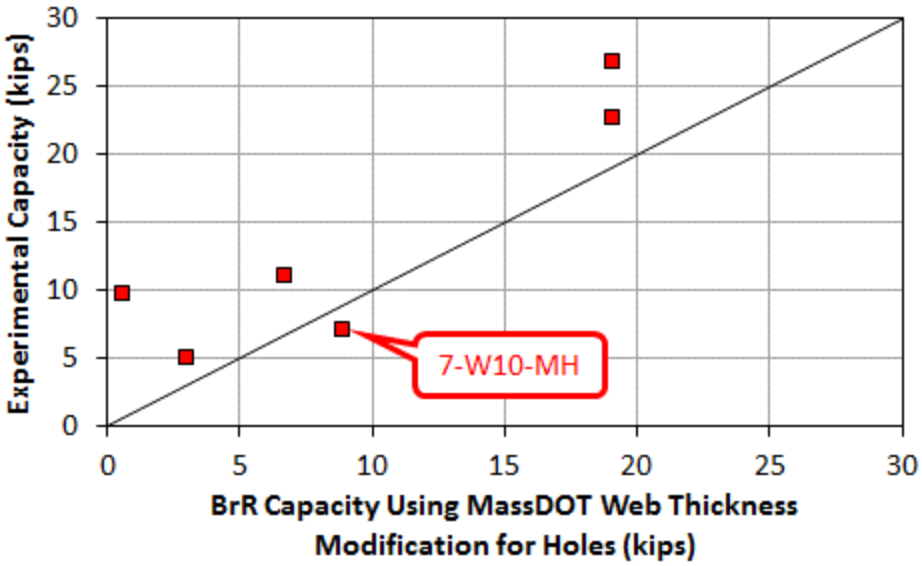

Figure 50. Comparison of Experimental and BrR Capacity Using MassDOT Effective Web Thickness Modification for Beams With Holes

As shown in the figure, five of the six beams with holes fell above the 45-degree line, indicating that the MassDOT hole modification produced a conservative capacity in BrR. Although Specimen 7-W10-MH fell below the line, its experimental capacity was only approximately 2 kips less than its capacity calculated in BrR. This shows that the MassDOT hole modification equation for determining an effective web thickness for beams with holes in conjunction with the use of the deterioration profile in BrR is an effective method for calculating the shear capacity of corroded steel beams with holes.

Figure 51 presents a summary of the effectiveness of the two methods presented in this study for using BrR to calculate the capacity of a corroded steel beam end. As previously mentioned, for beams with corrosion but no holes, the bottom 3-in web method was used to determine the remaining average web thickness. For beams with holes, the bottom 3-in method was also used, but the remaining average web thickness was modified using the MassDOT hole modification method shown in Equation 9. If the beam contained multiple holes in the same vicinity, the holes were conservatively treated as a single, large hole for which to determine a single hole length. With or without holes, the effective web thickness was then compared to each beam's nominal web thickness to determine the percent thickness loss. This value was then input into the BrR deterioration profile for each beam, and it was analyzed to compute a shear capacity.

As shown in the figure, nearly all of the data points fell above or only slightly below the 45-degree line, indicating these two methods were reasonably accurate and mostly conservative. The lone exception to this was Specimen 12-W16-H, which fell considerably below the 45-degree line. Since the specimen had general corrosion concentrated at the bottom of the beam without any holes, the research team expected good correlation between the experimental load and the shear capacity calculating using the bottom 3-in method. It is unknown why this beam did not provide as good agreement as the other beams in this study.

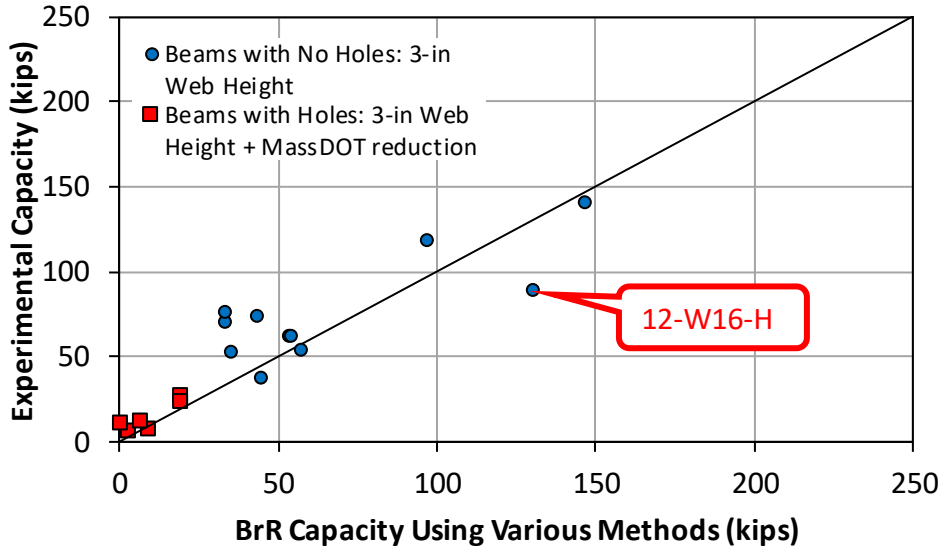

Figure 51. Comparison of Experimental and BrR Capacity Using Various Methods for Effective Web Thickness

Figure 52 shows a flowchart summarizing how to determine the shear capacity of a corroded steel beam end in BrR.

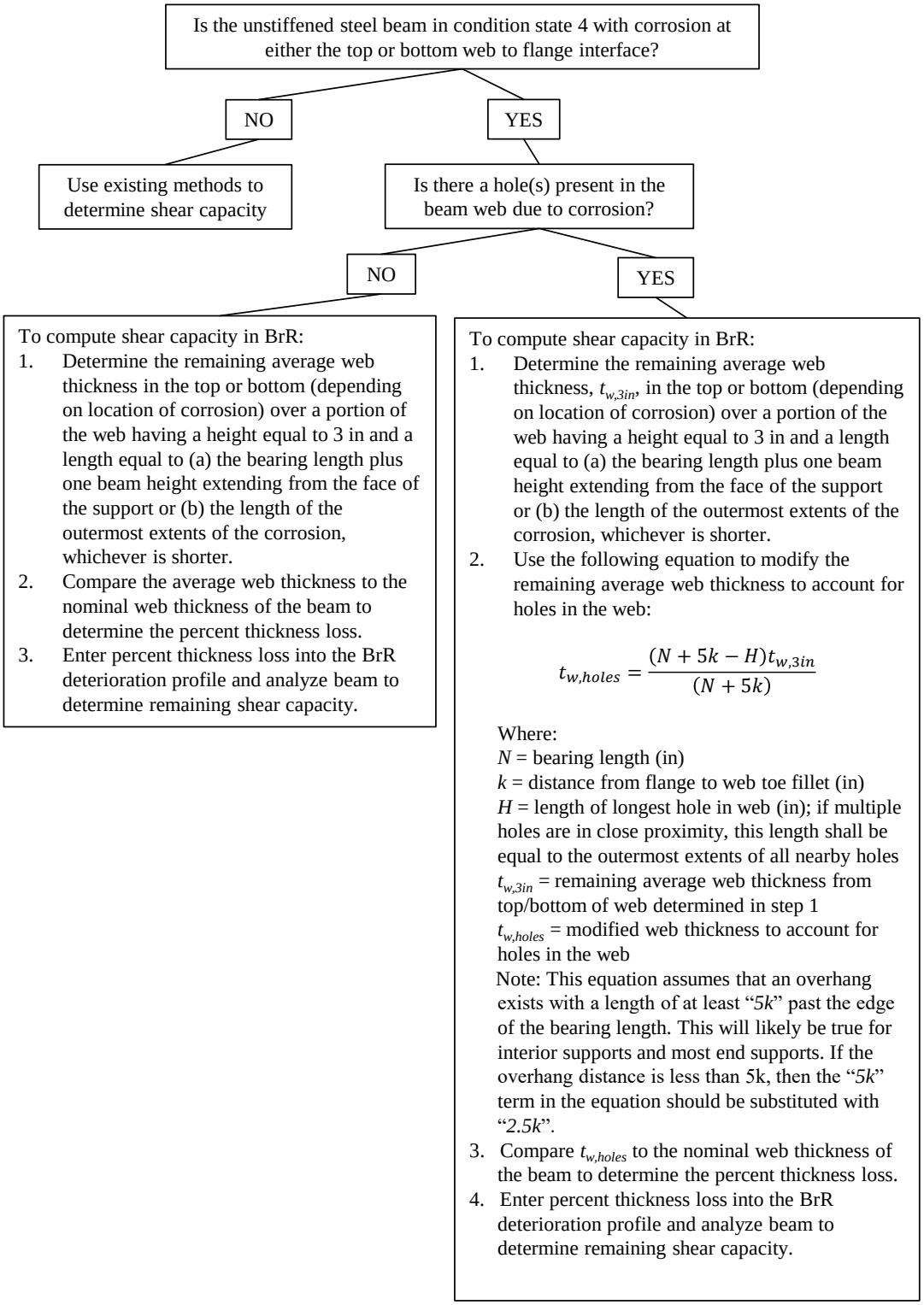

Figure 52. Flowchart for Determining Shear Capacity of Deteriorated Steel Beam End in BrR

The flowchart accounts for corrosion concentrated at the bottom of a steel beam end, near the web to flange interface, and differentiates between beams with and without holes in the web. The flowchart also provides guidance for determining the shear capacity in BrR for steel beam ends with corrosion concentrated at the top of the beam, which is common for steel beam bridges with timber decks.

CONCLUSIONS

- *The remaining shear capacity of a corroded steel beam end is highly dependent on the location, magnitude, and type of damage.* The failure modes of the specimens tested were influenced by the presence of section loss located near the top flange below the load and directly above the bottom flange over the bearing because of the high concentrations of stress in these areas. In addition, the length and number of holes contributed to the failure mode in cases where strains were allowed to develop in the web between the holes themselves or between the holes and the beam end.

- *Calculating the remaining average web thickness using the bottom 3-in and 4-in web heights provided the most conservative and accurate capacity estimates of the five methods compared.*

- *The Tzortzinis et al. method is a relatively accurate, yet conservative, method for determining the remaining shear capacity of a corroded steel beam end.* The method can be improved by calculating the remaining average web thickness using the bottom 3 in of the web, rather than the bottom 4 in of the web as recommended by Tzortzinis et al. (2019b).

- *BrR can reasonably be used to calculate the remaining shear capacity of a corroded steel beam end.* When doing so for a corroded steel beam without holes, the accuracy of BrR can be improved by calculating the percent thickness loss input in the BrR deterioration profile using a portion of the web with a height equal to the bottom or top 3 in of the web, depending on the location of severe corrosion, and a length equal to the lesser of the bearing length plus the beam height or the extent of the corrosion damage near the bearing. When doing so for a corroded steel beam end with holes, the BrR accuracy can be improved by using the same portion of the web and by modifying the remaining average web thickness using the guidelines provided in the 2020 MassDOT *LRFD Bridge Manual*, Part I, Section 7.2.9.2, before inputting the percent thickness loss into the BrR deterioration profile.

RECOMMENDATIONS

1. *VDOT's Structure and Bridge Division should provide guidance in a job aid for enhanced web thickness measurements and measurements of holes to be used for load rating of unstiffened corroded steel beam ends in Condition State 4 on bridges without diaphragms or a concrete deck.*

2. *VDOT's Structure and Bridge Division should provide guidance in VDOT's upcoming new load rating user manual to define the portion of the web and web thickness modification to account for web holes to be used for load rating unstiffened corroded steel beam ends in Condition State 4 on bridges without diaphragms or concrete decks.*

IMPLEMENTATION AND BENEFITS

Implementation

Implementation of Recommendation 1 will include incorporating guidance into a new or existing job aid to provide inspectors with the means and methods for assessing the condition of unstiffened corroded steel beam ends. The job aid may include descriptions and illustrations to demonstrate exactly where web thickness and hole measurements should be taken. Enhanced measurements need not be taken on all beam ends of a bridge but instead may be taken on the worst-case exterior and interior beams. Web thickness measurements may be taken with an ultrasonic thickness gauge, pit gauge, calipers, or other suitably accurate means. Web thickness measurements may be taken on an approximate 1-in grid (subject to field conditions) encompassing the bottom or top (depending on corrosion location) 3 in of the web along the length of the support plus one beam height away from the face of the support. These thickness measurements may be included in the inspection report or in supplemental field documentation to be preserved in the bridge file for year-over-year comparison. The relative location and length of all holes in a beam web because of corrosion may be measured and recorded. The relative location measurements may include a hole's vertical position on a girder web and its horizontal position relative to the beam bearing. The length measurement may include the length of all holes within a distance of one beam height from the end of the beam's bearing. A diagram of these measurements is shown in Figure 45. These changes may eventually be incorporated into the VDOT Structure and Bridge Division Instructional and Informational Memorandum Number IIM-S&B-86.4 (VDOT, 2020) after experience is gained using the job aid. Implementation of Recommendation 1 should have a goal of field use within 2 years of the publication of this report.

Implementation of Recommendation 2 will include additions to VDOT's upcoming new load rating user manual. Additions may include descriptions and illustrations of the portion of the web used for determining the web percent thickness loss. Revisions may also include an equation and guidance to modify the remaining web thickness to account for holes in the beam web because of corrosion. The portion of the web and web thickness modification to account for holes is outlined in Figure 52, which can be included in VDOT's upcoming new load rating user manual as guidance for this procedure. Additions may also instruct load raters that BrR should be used for rating whenever possible; however, a standardized Mathcad or Excel sheet incorporating these additions may be developed for other cases. Implementation of Recommendation 2 should have a goal of standardized use by load raters within 2 years of the publication of this report.

Benefits

Implementation of Recommendation 1 will provide VDOT with clear guidance for bridge inspectors when making web thickness and hole position and length measurements of corroded steel beam ends. These additional measurements will allow load raters access to a more detailed account of a beam end's current condition. Further, having additional documented web thickness and hole position and length measurements will allow for improved tracking of corrosion damage over time.

Implementation of Recommendation 2 will provide VDOT with an accurate, yet conservative, method for using BrR to determine the remaining shear capacity of unstiffened corroded steel beam ends with and without holes. Although BrR has limited inputs for modeling corrosion damage, it is the standard method for VDOT load rating because it interfaces with the Department of Motor Vehicles for heavy vehicle routing. Implementation of Recommendation 2 will provide a method to work around the limitations of BrR without sacrificing the interface with the Department of Motor Vehicles.

ACKNOWLEDGMENTS

The authors acknowledge several key groups and people who were instrumental in enabling and supporting this study. Major thanks go to Chris Williams for championing the project and to Soundar Balakumaran, Jeff Hill, Bernie Kassner, and Adam Matteo for serving on the study's technical review panel. The authors also thank all of the VDOT districts that were involved in procurement and delivery of steel beam specimens including the Bristol, Culpeper, Northern Virginia, Salem, and Staunton districts. In addition, the authors thank Roberto Leon and Carin Roberts-Wollmann from Virginia Tech for their feedback on the study and its accompanying thesis work. The authors also thank everyone who supported this study through their guidance and assistance including Ali Alfailakawi, Raul Avellaneda, Garrett Blankenship, Brett Farmer, David Mokarem, Bill Ordel, Sam Sherry, Japsimran Singh, Ryan Stevens, Adrian Tola, and all the undergraduate lab assistants. Without all of these individuals, this study could not have been completed.

REFERENCES

AASHTO. *AASHTO LRFD Bridge Design Specifications,* 8th Edition. Washington, DC, 2017.

AASHTO. *The Manual for Bridge Evaluation,* 3rd Edition. Washington, DC, 2018.

American Institute of Steel Construction. *AISC 360-16: Specification for Structural Steel Buildings.* Chicago, 2016.

ASTM International. *ASTM E8 / E8M-21: Standard Test Methods for Tension Testing of Metallic Materials.* West Conshohocken, PA, 2021.

Darwin, D., and Donahey, R.C. LRFD for Composite Beams With Unreinforced Web Openings. *Journal of Structural Engineering,* Vol. 114, No. 3, 1988, pp. 535-552.

Kayser, J.R., and Nowak, A.S. Capacity Loss Due to Corrosion in Steel-Girder Bridges. *Journal of Structural Engineering,* Vol. 115, No. 6, 1989a, pp. 1525-1537.

Kayser, J.R., and Nowak, A.S. Reliability of Corroded Steel Girder Bridges. *Structural Safety,* Vol. 6, No. 1, 1989b, pp. 53-63.

Massachusetts Department of Transportation. *LRFD Bridge Manual, Part I, Chapter 7, LRFD Bridge Load Rating Guidelines, January Revision*. 2020. LRFD Bridge Manual - Part I, January 2020 Revision. https://www.mass.gov/doc/chapter-7-bridge-load-rating-guidelines/download. Accessed August 5, 2021.

Rahgozar, R. Remaining Capacity Assessment of Corrosion Damaged Beams Using Minimum Curves. *Journal of Constructional Steel Research,* Vol. 65, No. 2, 2009, pp. 299-307.

Sugimoto, I., Kobayashi, Y., and Ichikawa, A. Durability Evaluation Based on Buckling Characteristics of Corroded Steel Deck Girders. *Quarterly Report of RTRI (Railway Technical Research Institute) (Japan),* Vol. 47, No. 3, 2006, pp. 150-155.

Timoshenko, S., and Gere, J. *Theory of Elastic Stability*, 2nd Edition. McGraw-Hill, New York, 1961.

Tzortzinis, G., Gerasimidis, S., Breña, S., and Knickle, B. *Development of Load Rating Procedures for Deteriorated Steel Beam Ends.* Report No. 19-008. Massachusetts Department of Transportation, Boston, 2019a.

Tzortzinis, G., Knickle, B., Gerasimidis, S., Bardow, A., and Breña, S. Identification of Most Common Shapes and Locations for Beam End Corrosion of Steel Girder Bridges. Presented at the Annual Meeting of the Transportation Research Board, Washington, DC, January 13-17, 2019b.

van de Lindt, J.W., and Ahlborn, T.M. *Development of Steel Beam End Deterioration Guidelines.* RC-1454. Michigan Department of Transportation, Lansing, 2005.

Virginia Department of Transportation. *VDOT Supplement to the AASHTO Manual for Bridge Element Inspection.* 2016. https://www.virginiadot.org/business/resources/bridge/VDOT_Suppl_to_the_AASHTO_Manual_for_Bridge_Element_Insp_2016.pdf. Accessed August 5, 2021.

Virginia Department of Transportation. Structure and Bridge Division Instructional and Informational Memorandum Number IIM-S&B-86.4. 2020. https://www.virginiadot.org/business/resources/bridge/Manuals/IIM/SBIIM86.4.pdf. Accessed October 6, 2021.

APPENDIX

ADDITIONAL STRAIN FIELD FIGURES

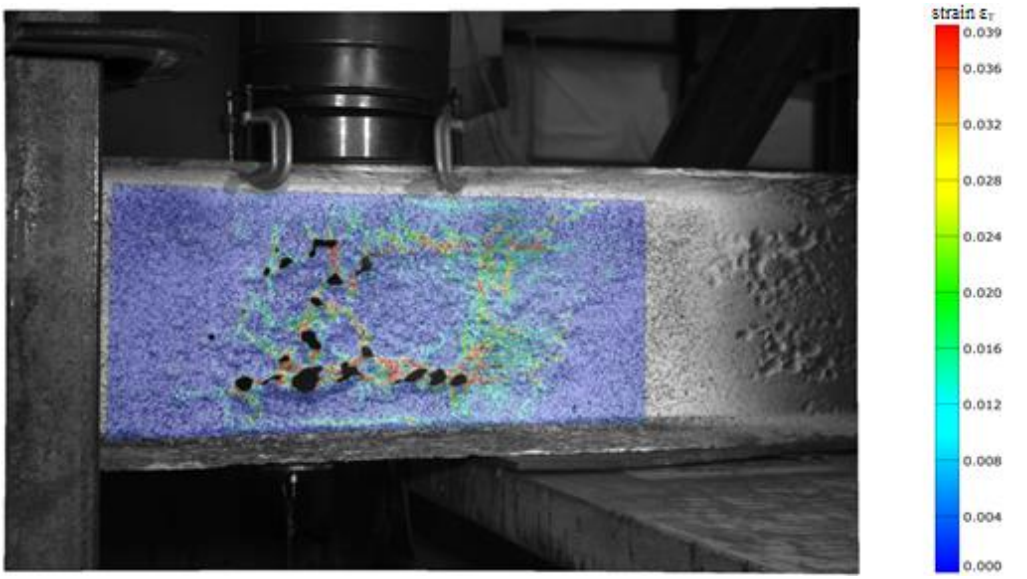

Figure A1. True Major Strain Field of Specimen 4-S8-H at 22.8 Kips of Loading Before Maximum Loading

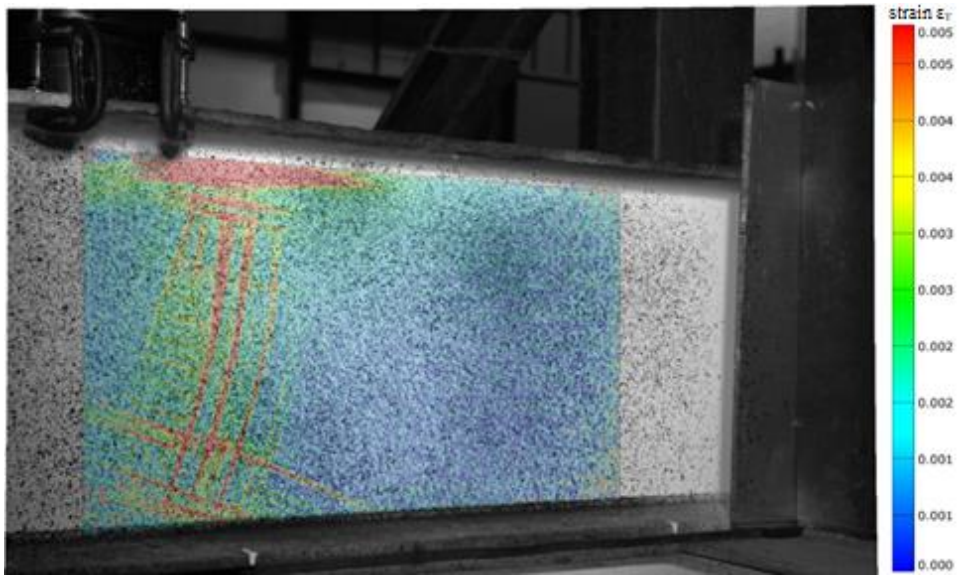

Figure A2. True Major Strain Field of Specimen 5-W10-L at 49.8 Kips of Loading Before Failure

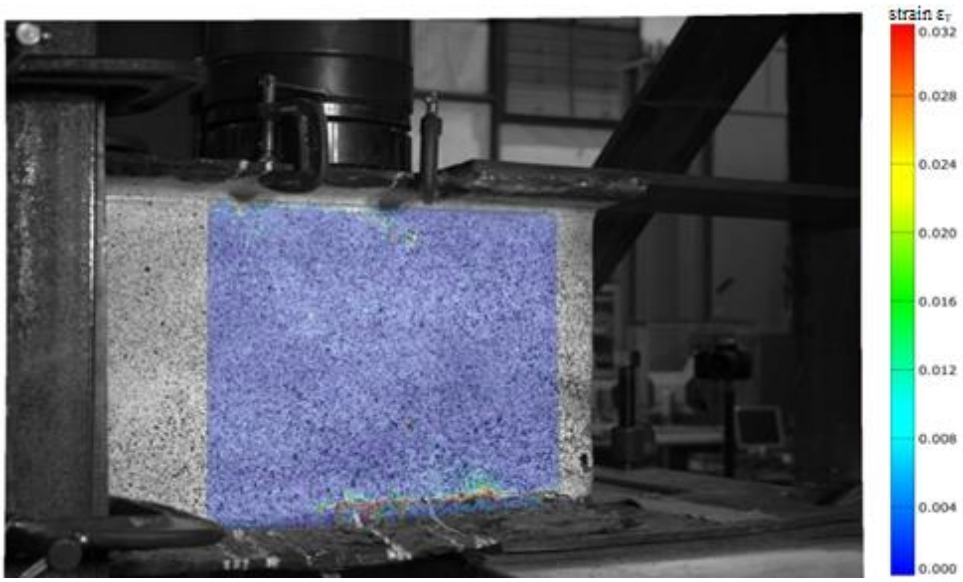

Figure A3. True Major Strain Field of Specimen 7-W10-MH at 0.45 in of Downward Vertical Displacement After Failure

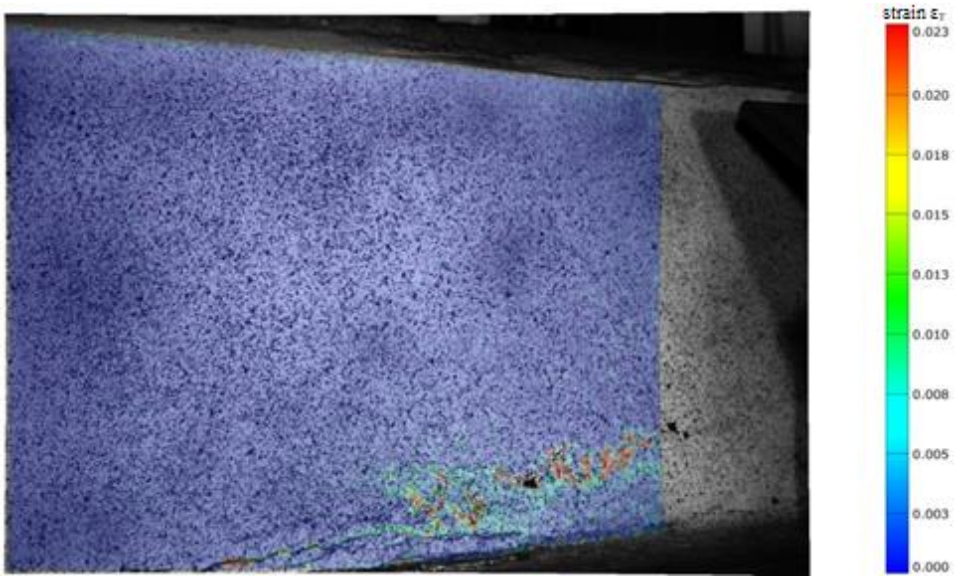

Figure A4. True Major Strain Field of Specimen 11-W16-MH at 55 Kips of Loading Before Failure

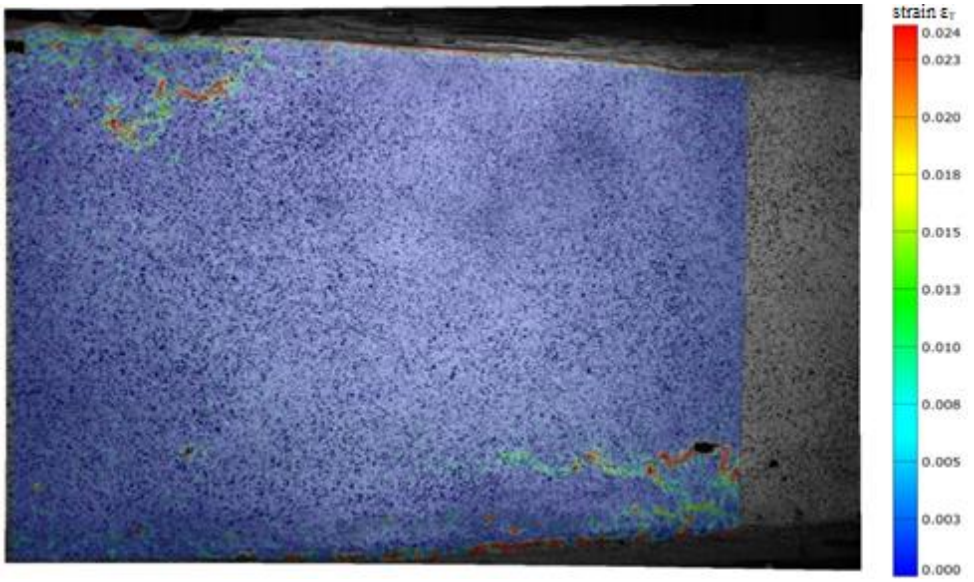

Figure A5. True Major Strain Field of Specimen 12-W16-H at 79 Kips of Loading Before Failure

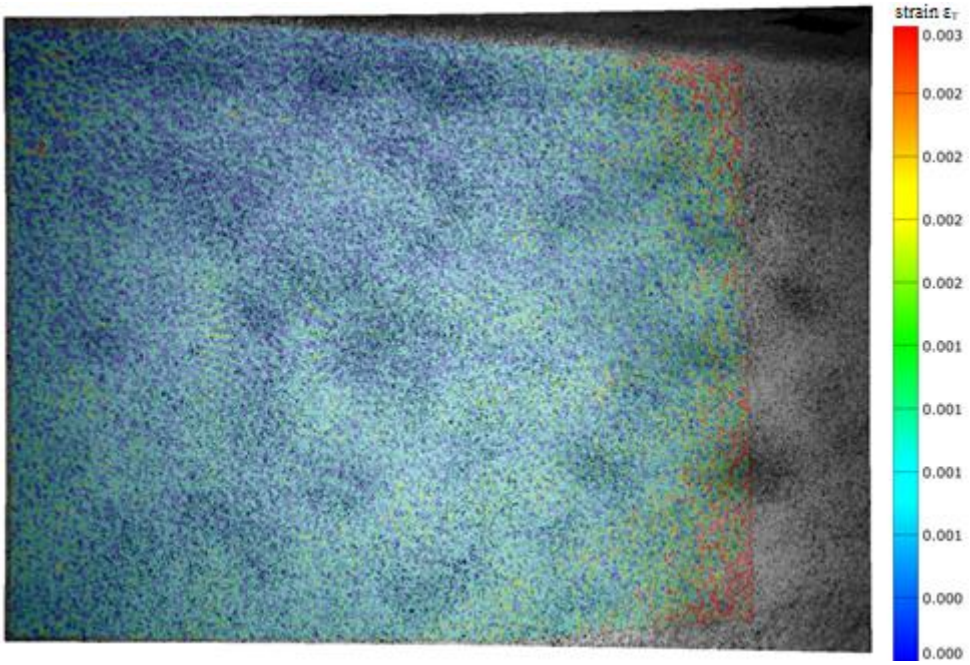

Figure A6. True Major Strain Field of Specimen 15-W21-ML at 45 kips Loading Before Failure

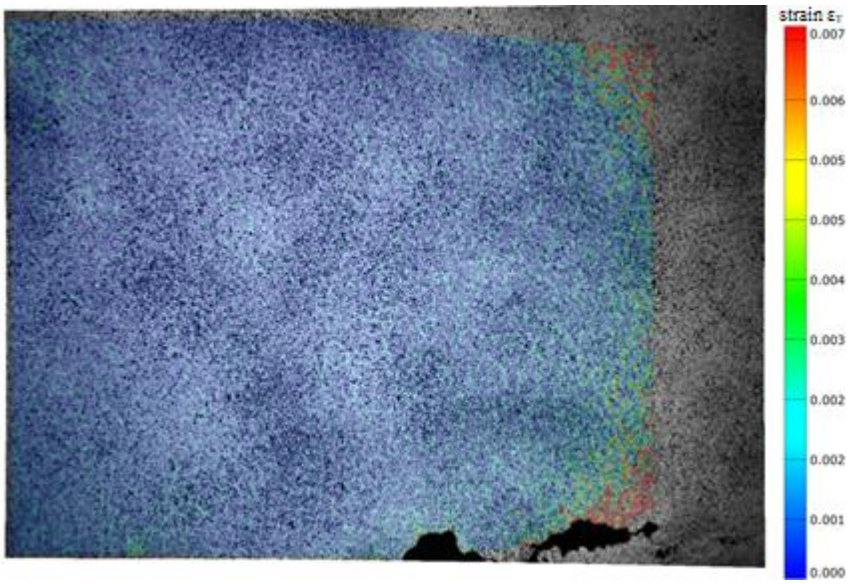

Figure A7. True Major Strain Field of Specimen 16-W21-MH at 0.15 in of Downward Vertical Displacement After Failure

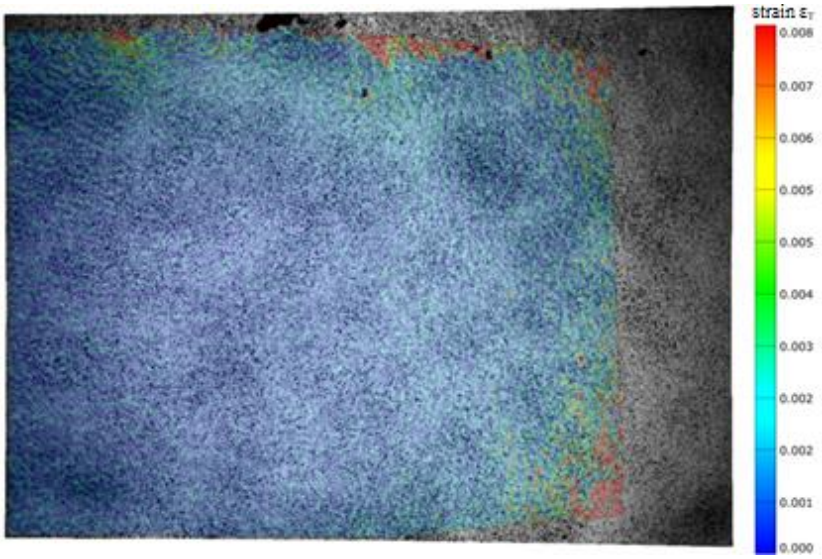

Figure A8. True Major Strain Field of Specimen 17-W21-H at 52 kips Loading Before Failure